

General Disclaimer

One or more of the Following Statements may affect this Document

- This document has been reproduced from the best copy furnished by the organizational source. It is being released in the interest of making available as much information as possible.
- This document may contain data, which exceeds the sheet parameters. It was furnished in this condition by the organizational source and is the best copy available.
- This document may contain tone-on-tone or color graphs, charts and/or pictures, which have been reproduced in black and white.
- This document is paginated as submitted by the original source.
- Portions of this document are not fully legible due to the historical nature of some of the material. However, it is the best reproduction available from the original submission.

ADVANCED METEOROLOGICAL
TEMPERATURE SOUNDER
(AMTS) STUDY

FINAL REPORT
NOV. 10, 1977

CONTRACTOR:
ITT AEROSPACE/OPTICAL DIV.
FT. WAYNE, IN 46803

STUDY PERFORMED FOR:
CALIFORNIA INSTITUTE OF TECHNOLOGY
JET PROPULSION LABORATORY
4800 OAK GROVE DRIVE
PASADENA, CALIFORNIA 91102

JPL CONTRACT NO. 954788



(NASA-CR-157083) ADVANCED METEOROLOGICAL
TEMPERATURE SOUNDER (AMTS) STUDY Final
Report (ITT Aerospace/Optical Div.) 109 P
HC A06/MF A01 CSCL 04E

N78-24752

Unclas
G3/47 20711

ADVANCED METEOROLOGICAL
TEMPERATURE SOUNDER
(AMTS) STUDY

FINAL REPORT
NOV. 10, 1977

CONTRACTOR:
ITT AEROSPACE/OPTICAL DIV.
FT. WAYNE, IN 46803

PREPARED BY
ELECTO-OPTICAL SYSTEMS DEPT.

STUDY PERFORMED FOR:
CALIFORNIA INSTITUTE OF TECHNOLOGY
JET PROPULSION LABORATORY
4800 OAK GROVE DRIVE
PASADENA, CALIFORNIA 91102

JPL CONTRACT NO. 954788

THIS WORK WAS PERFORMED FOR THE JET PROPULSION
LABORATORY, CALIFORNIA INSTITUTE OF TECHNOLOGY
SPONSORED BY THE NATIONAL AERONAUTICS AND SPACE
ADMINISTRATION UNDER CONTRACT NAS 7 - 100.

TABLE OF CONTENTS

	TECHNICAL CONTENT STATEMENT	PAGE
	ABSTRACT	iii
1.	INTRODUCTION	1
2.	INSTRUMENT CONFIGURATION (TIROS)	4
3.	TECHNICAL ANALYSES	
3.1	OPTICAL DESIGN	9
3.2	RADIANT COOLER	47
3.2.1	COVER TEMPERATURES	47
3.2.2	RADIATOR THERMAL ANALYSIS	52
3.2.3	PATCH THERMAL ANALYSIS	55
3.3	DETECTOR SELECTION AND SYSTEM SENSITIVITY	60
3.3.1	AMTS REQUIREMENTS	60
3.3.1.1	SYSTEM PARAMETERS	60
3.3.1.2	SCENE RADIANCES	61
3.3.1.3	SIGNAL-TO-NOISE REQUIREMENTS	61
3.3.2	DETECTOR SELECTION	61
3.3.2.1	INDIUM ANTIMONIDE CHANNELS (13-28)	63
3.3.2.2	MERCURY-CADMIUM- TELLURIDE CHANNELS (1-12)	72
3.3.3	SYSTEM SENSITIVITY	76
3.3.3.1	DEGRADATION FACTORS	76
3.3.3.2	SIGNAL/NOISE IN CHS. 13-28	80
3.3.3.3	SIGNAL/NOISE IN CHS. 1-12	82
3.4	ELECTRONICS DESIGN	87
3.5	INSTRUMENT COOLING	102
4.	NEW TECHNOLOGY	105

TECHNICAL CONTENT STATEMENT

This report contains information prepared by ITT Aerospace/Optical Division under JPL sub-contract. Its content is not necessarily endorsed by the Jet Propulsion Laboratory, California Institute of Technology, or the National Aeronautics and Space Administration.

ABSTRACT

This report describes the results of a system definition study (theoretical) for an Advanced Meteorological Temperature Sounder (AMTS) performed by ITT Aerospace/Optical Division for Jet Propulsion Laboratory. The AMTS will be mounted on an earth-orbiting spacecraft such as TIROS-N and will measure earth radiance in twenty-eight infrared bands at the 4.3 and 15 μ m CO absorption wavelengths. From this data the atmospheric temperature and humidity profiles can be determined over the entire earth's surface with a spatial resolution* of 45 km. x 45 km; amounts and type of cloud cover as well as surface temperatures of the earth are also determined. Vertical temperature resolution significantly better than obtained with previous sounding instruments is predicted as a result of the narrower spectral bands (2 cm⁻¹ at 4.3 μ m and 0.5 cm⁻¹ at 15 μ m).

The major purpose of the study was to determine the feasibility of cooling the twenty-eight detectors to the 80-90 Kelvin region by means of a radiative cooler. Other related considerations were achieving high signal-to-noise ratios, maximizing optical throughput through the grating spectrometer and reducing preamplifier noise. Instrument size was restricted by the f-number of the spectrometer and the smallest width of the field lenses that were deemed manufacturable (1 m.m.). A detailed optical design of an f/5 Ebert-Fastie spectrometer was carried out to verify that image quality is adequate; field lenses near the spectrometer focal plane were designed to image the grating onto the smallest size detectors for each channel. Effects of the basic spectrometer design on system throughput, detector size, size and spacing of field lenses, entrance and exit slit width and height, etc. were analyzed prior to selection of the final spectrometer parameters (grating size and grooves per m.m., blaze angle and wavelength and mirror focal length).

The results of the study indicate that an instrument can be designed and built which will fulfill the scientific objectives. Recommendations include additional optical, thermal and structural analyses as well as fabrication and test of critical system components.

* instantaneous field of view

1.0 INTRODUCTION

This report describes the results of a 3 months system definition study for an Advanced Meteorological Temperature Sounder (AMTS) performed by ITT Aerospace/Optical Division for Jet Propulsion Laboratory. The AMTS instrument is designed for operation on board an earth, polar orbiting spacecraft such as the TIROS-N. The AMTS measures earth radiance in both the 4.3 μ m and 15 μ m CO₂ absorption bands and vertical temperature profile information for the earth's atmosphere can be extracted from this data. The AMTS design incorporated much narrower spectral bands than the HIRS¹ instrument (High Resolution Infrared Radiation Sounder) or the J.P.L. Multidetector Sounder^{2,3,4} and is expected to significantly improve the vertical temperature resolution. The AMTS will also provide additional meteorological information such as the humidity profile, day and night surface temperatures of the ground and oceans, cloud-type identification for storm detection and day-night mapping of cloud cover amount and heights. The data obtained will not only improve remote sensing of tropospheric temperature profiles but will also improve the accuracy of numerical weather forecasting models.

The major purpose of the study was to determine the feasibility of radiatively cooling the twenty-eight infrared detectors to low enough a temperature where good signal-to-noise ratios could be obtained. Thus detector performance and optical throughput of the spectrometer were also major considerations. The spectral channels and bandwidths for AMTS are listed in Table 1. The spectrometer is designed so that the diffraction grating is used in first order in channels 1 through 10, second order in channels 11 and 12, third order in channels 13 through 19 and fourth order in channels 20 through 28. The effects of the basic spectrometer design on system throughput, detector size, size and spacing of field lenses, etc. were analyzed by ITT-A/OD; an analysis of spectrometer optical resolution (image blur spot size), detailed field lens and collimator-imaging mirror design and optical ray-traces were done by Optical Research Associates, Pasadena, California, under subcontract to ITT-A/OD.

1. The High Resolution Infrared Radiation Sounder (HIRS), Koenig & Zaun (ITT-A/OD), Presentation at 1975 Spring Conference of the Optical Society of America.
2. Performance of a Spectrometer for Measuring the Earth's Radiance Near 4.3 μ m, Schaper & Shaw, Applied Optics, Vol. 9 p. 924, April 1970.
3. Infrared Multidetector Spectrometer for Remote Sensing of Temperature Profiles in the Presence of Clouds, Aumann & Chahine, Applied Optics, Vol. 15, p. 2091, September 1976.
4. Spectral Bandpasses for a High Precision Satellite Sounder, L. Kaplan et al, Applied Optics, Vol. 16, p. 322, Feb. 1977

Table I

ADVANCED METEOROLOGICAL TEMPERATURE SOUNDER (AMTS) SPECTRAL BANDS

Channel Number	Center Wavelength		Resolution $\Delta\nu$ (cm^{-1})	Main Function
	ν (cm^{-1})	λ (μm)		
1	607.00	16.474	0.5	Cloud filtering
2	623.23	16.045	0.5	Cloud filtering
3	627.75	15.929	0.5	Cloud filtering
4	635.80	15.728	0.5	Temperature
5	646.65	15.464	0.5	Temperature
6	652.75	15.320	0.5	Temperature
7	666.20	15.010	0.5	Temperature
8	666.90	14.995	0.5	Temperature
9	668.10	14.968	0.5	Temperature
10	669.10	14.945	0.5	Temperature
11	1203.00	8.313	1.0	} Windows and Cloud filtering
12	1231.80	8.118	1.0	
13	1772.00	5.643	1.5	Humidity
14*	1844.50	5.422	1.5	Humidity
15	1889.50	5.292	1.5	Humidity
16*	1809.50	5.526	1.5	Humidity
17	1839.40	5.437	1.5	Humidity
18*	1850.90	5.403	1.5	Humidity
19	1930.10	5.181	1.5	Humidity
20	2383.75	4.1951	≤ 2.0	Temperature
21	2386.10	4.1909	≤ 2.0	Temperature
22	2388.20	4.1873	≤ 2.0	Temperature
23	2390.20	4.1837	≤ 2.0	Temperature
24	2392.35	4.1800	≤ 2.0	Temperature
25*	2394.50	4.1762	≤ 2.0	Temperature
26	2424.00	4.1254	2.5	} Surface Temperature
27	2505.00	3.9920	2.5	
28	2616.50	3.8219	2.5	

*Tentative

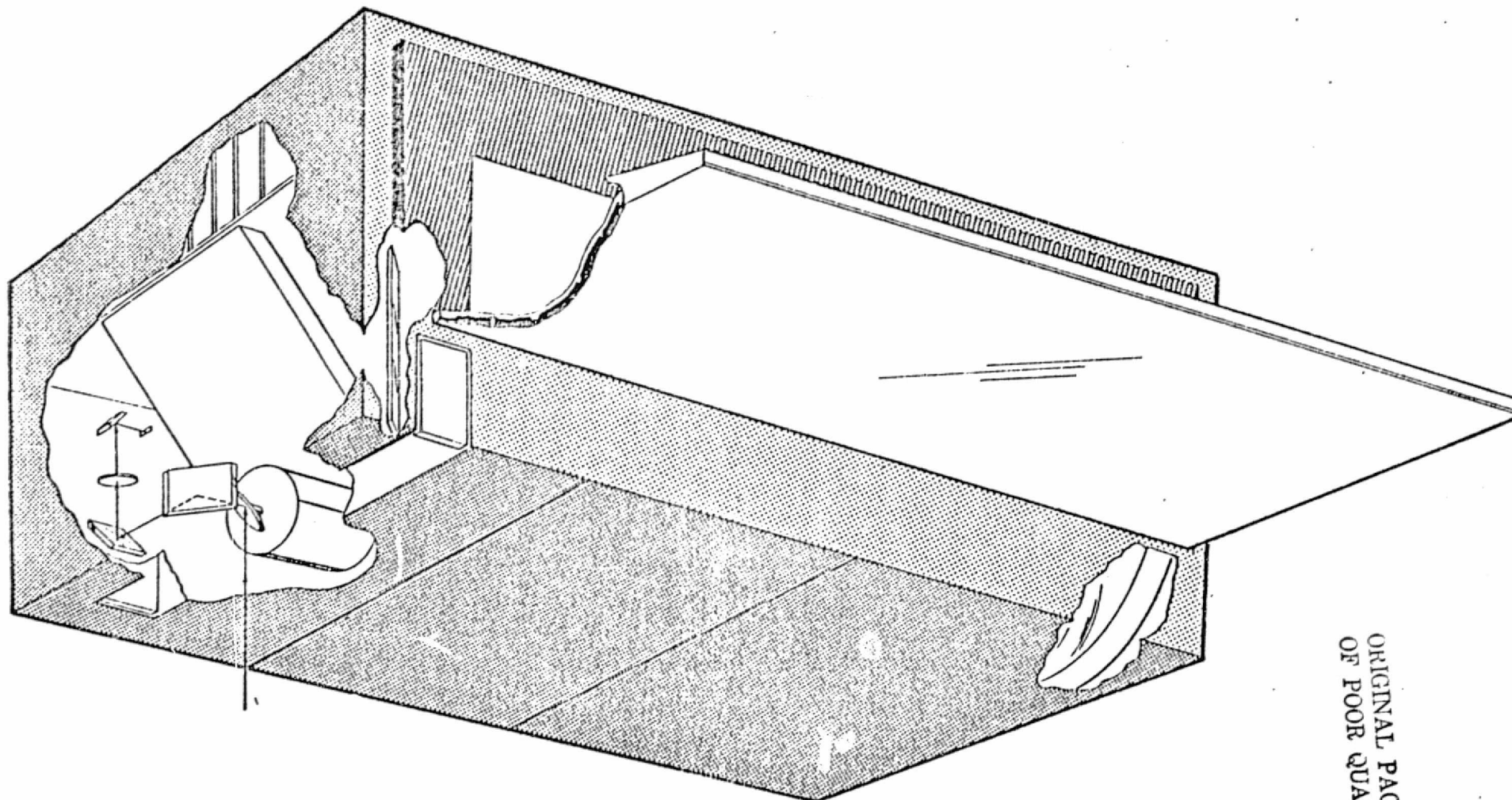
Electronics design and analysis was restricted to the pre-amplifiers for the infrared detectors since this has an effect on noise levels and hence signal-to-noise performance; no breadboarding or tests were done under this study contract.

The results of our study indicate that an instrument can be designed and built which will fulfill the scientific objectives described above. The rest of this report describes the results of the study effort and gives a brief description of the important features of the proposed AMTS.

2.0 INSTRUMENT CONFIGURATION (TIROS)

Figure 2-1 is an artist's illustration of the Advanced Meteorological Temperature Sounder for the Tiros-class spacecraft; Figure 2-2 shows external dimensions of the AMTS instrument. The AMTS is only slightly larger than the AVHRR for TIROS-N which measures 11" x 15" x 31"; estimated weight for AMTS is 75 pounds compared with 54.3 pounds for AVHRR, 73 pounds for HIRS and 90 pounds for VHRR for ATS-6. The instrument is located on the spacecraft so that the radiant cooler is always on the anti-solar side looking toward space as shown in Figure 2-3. The major portion of the volume is taken up by the f/5 Ebert-Fastie grating spectrometer ("over/under" configuration) which has a focal length of 3/4 meter. The radiant cooler, which is designed to cool twenty-eight infrared detectors to an operating temperature of 84 kelvins, is a scaled up version of the AVHRR radiant cooler (AVHRR is an imaging radiometer to be flown on Tiros N.). The cooler consists of a first stage radiator operating at 154 kelvins and an earth shield which shields the second stage radiator (patch) from earth radiance. The earth shield folds over the first and second stage radiators during launch and for two or three weeks thereafter until the gaseous atmosphere surrounding the spacecraft has subsided and the danger of contamination of cold optical surfaces and detectors is no longer present. The twenty eight infrared detectors as well as twenty eight small field lenses are mounted to the second stage cold patch. The input stage and feedback resistor for sixteen preamplifiers are mounted on the first stage radiator for improved performance and to lessen stray capacitance and noise pickup.

The spectrometer incorporates a 6" x 8" diffraction grating having 80 grooves per m.m. and blazed at 41° for $16.4\mu\text{m}$ (610 cm^{-1}) in first order. The collimating and imaging mirror is a single element aspherical mirror with a focal length of 762 m.m. The dispersed spectrum is reflected by a long rectangular flat mirror to direct the 159 m.m. long spectrum into the radiant cooler. The first four orders of the grating are used without any beamsplitters since the spectral bands have been selected in such a way that none of the channels physically interfere with each other. Thus all twenty eight detectors lie in a row (slightly curved) as shown in Figure 2-4 (note that all channels have been converted to first order equivalent wavenumbers). Channels 22 and 23 are the closest spaced channels being only 0.5 cm^{-1} apart (referenced to first order); channels 7 and 8 are 0.7 cm^{-1} apart between centers. The spectral bands will be defined by thin aperture masks in the focal plane of the spectrometer exit beam. Immediately behind the aperture masks are thin field lenses which image the grating onto individual detectors for each channel. In many cases the field lenses must be cut in thin sections (defined by two planes parallel to the lens axis) about 1.2 m.m. thick for channels 22 and 23 (the detector, field lens, mask array is not shown in Figure 2-1).



ORIGINAL PAGE IS
OF POOR QUALITY

FIG. 2-1 ADVANCED METEOROLOGICAL TEMPERATURE SOUNDER

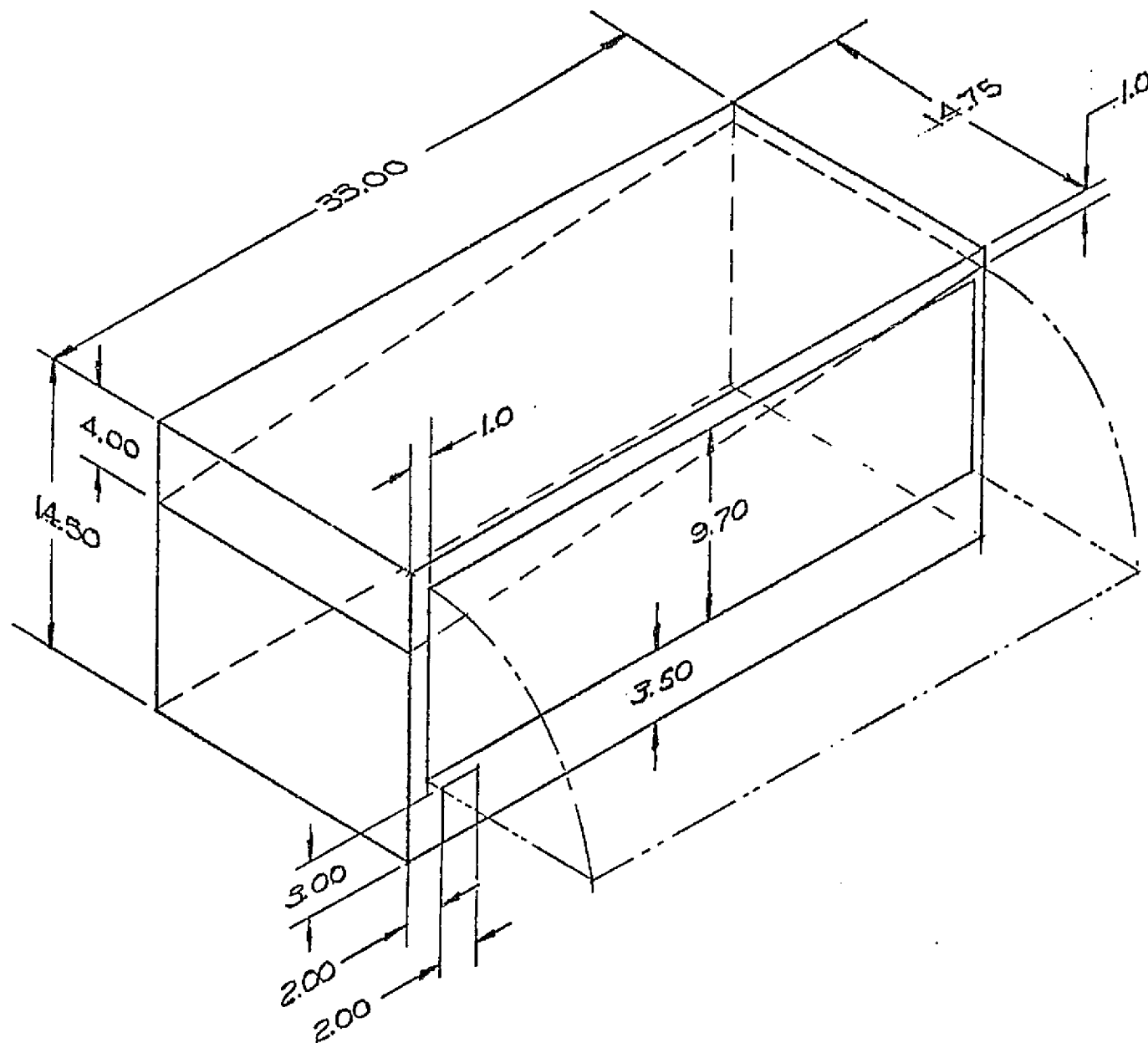


Fig. 2-2 AMTS Envelope (dimensions in inches)

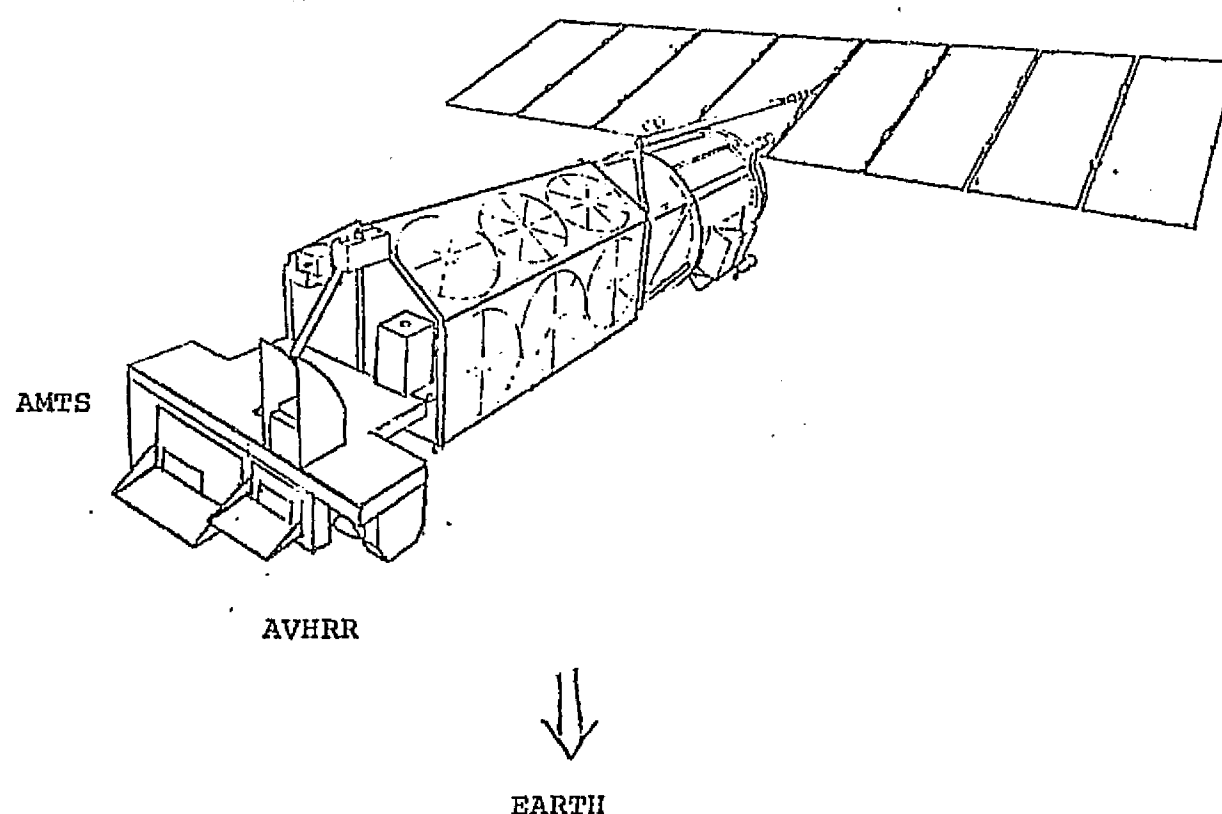


FIG. 2-3 AMTS and AVHRR on TIROS-N SPACECRAFT

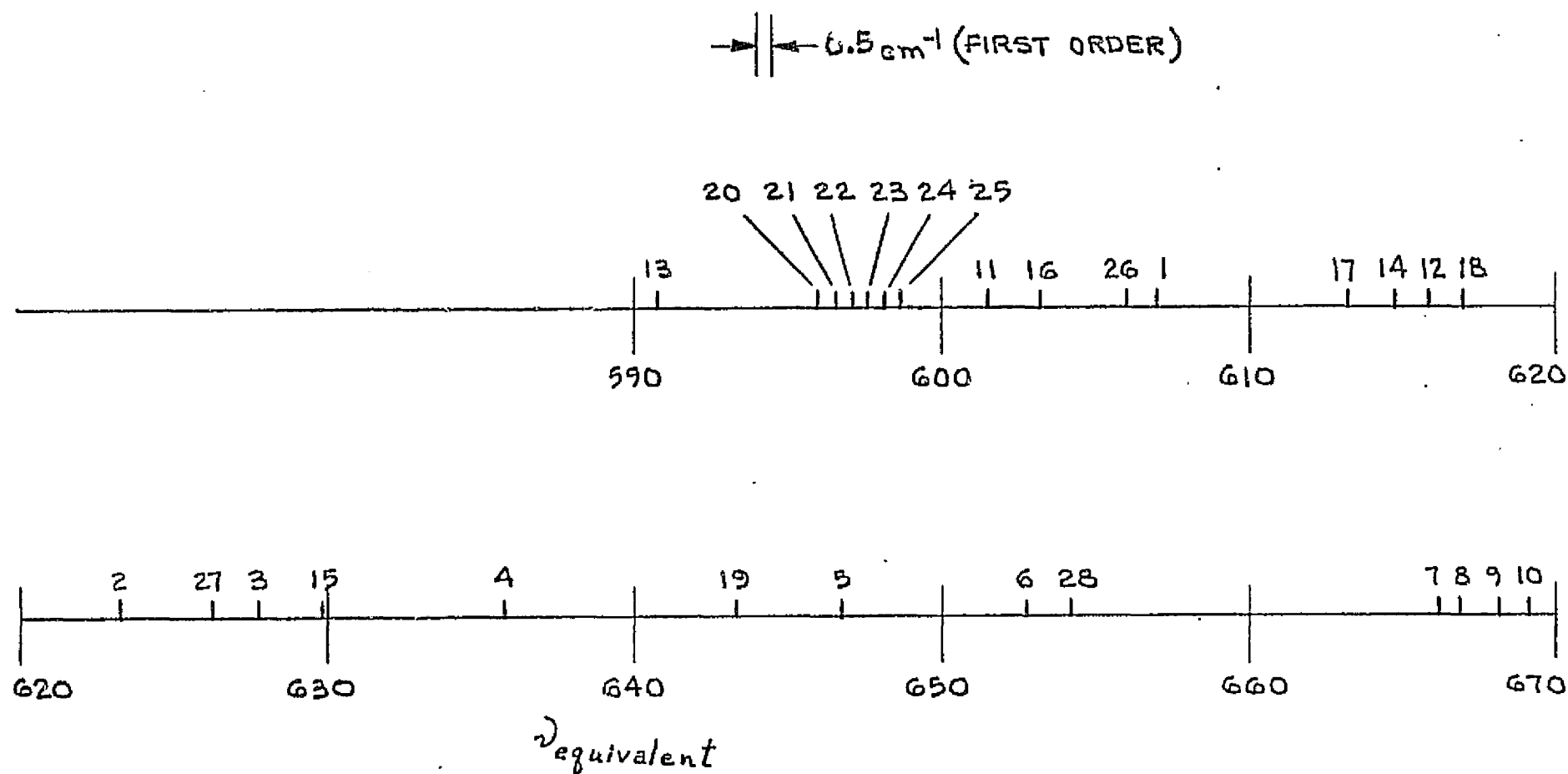


FIG. 2-4 AMTS SPECTRAL BANDS

The spectrometer entrance slit is imaged onto the earth by the telescope lens which has a focal length of 110 m.m and clear aperture diameter of 31.5 m.m. (the grating is the aperture stop for the system). A scan mirror sweeps the optical beam across the earth through an angle of 60°, 30° on each side of nadir. Three flat folding mirrors must be used to orient the length of the slit image perpendicular to the mirror scan direction (the scan mirror sweep is perpendicular to the satellite orbital motion). Two internal calibration targets, one at ~ 250K and the other at ~ 300K, serve as temperature calibration points in addition to the space reference; the calibration sequence has not been established as yet. A tuning fork chopper which modulates the optical beam near the entrance slit is illustrated in Figure 2-5, Conceptual Design Optical Layout. The spectrometer housing and optical elements are cooled to 248K by covering the side facing the earth with a silver-teflon radiator surface and appropriate thermal, structural design. This is essential for reducing the thermal background irradiance on the indium antimonide detectors (used in channels 13 to 28) and it also benefits the radiant cooler performance.

Mercury-Cadmium-Telluride detectors are used in Channels 1 to 12 since they provide the best signal to noise ratio when cooled to the 84 kelvin range. The system design described in this report has been selected to achieve the highest performance possible (i.e., S/N ratios of 100 or more in all channels; a lower ratio is estimated for channel 28 but this is acceptable). The spatial resolution or effective field of view at the subsatellite point is 45 km. x 45 km. with all channels viewing the same area on the ground simultaneously; cloud filtering analysis is performed on the data to obtain clear column profiles on a 90 km. x 90 km. area scale.

3.1 Optical Design

3.1.1 Design Analysis

To start with, we will present the first-order design of a spectrometer for the AMTS. In particular, we will determine the range and nominal values of the following parameters:

- a. Throughput
- b. Entrance slit width
- c. Slit length
- d. Spectrum length
- e. Exit slit (field lens aperture) widths
- f. Detector element width

The design is based on the grating equation

$$\sin i + \sin r = \frac{m \lambda}{a} = \frac{m}{a v}$$

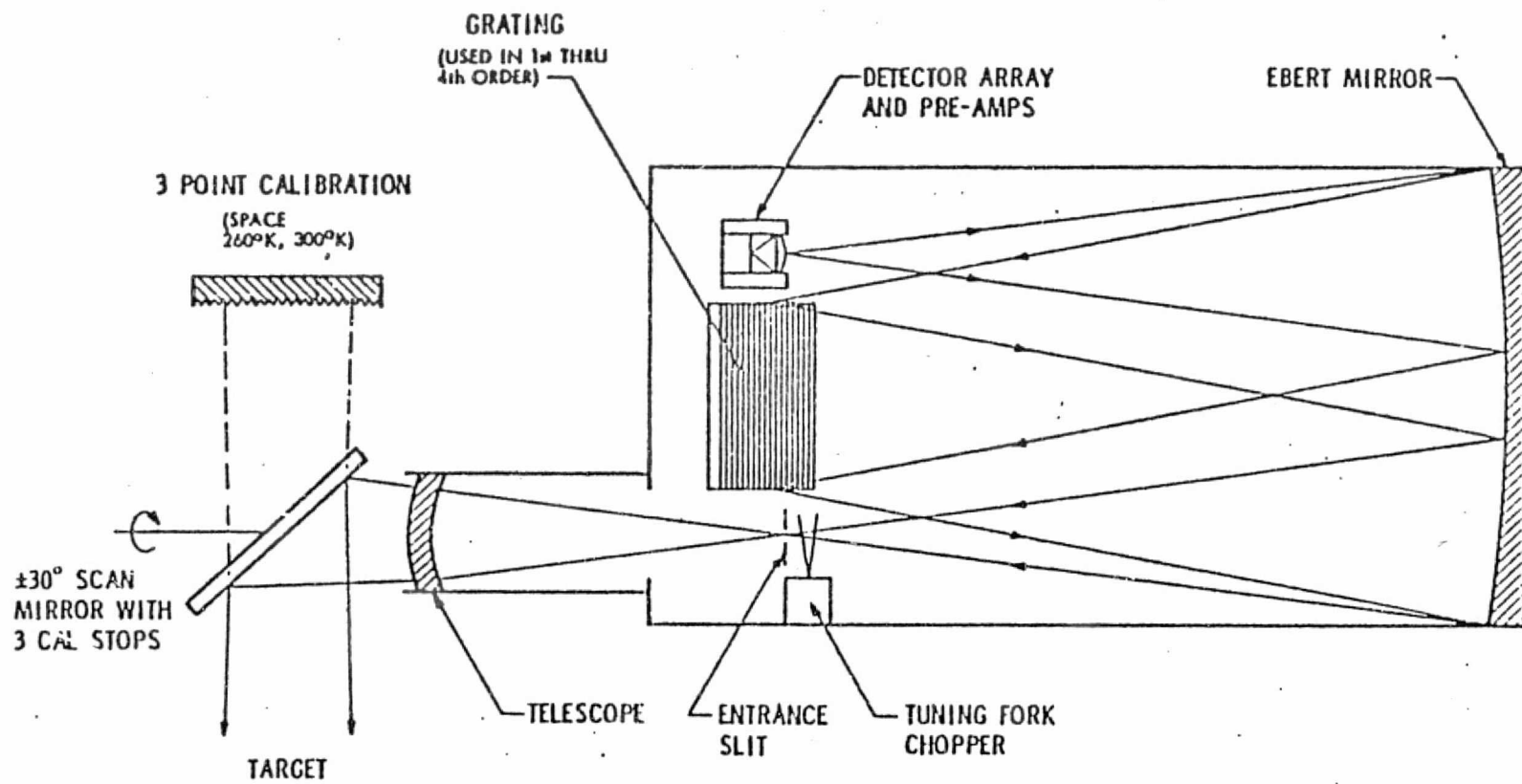


Fig. 2-5 CONCEPTUAL DESIGN - OPTICAL LAYOUT, AMTS

where i = incidence angle with respect to grating normal
 r = diffraction angle with respect to grating normal
 m = order number
 λ = wavelength
 a = width of a grating groove
 ν = wavenumber.

As a result, we have neglected the (second order) effects of both oblique incidence on the grating (J. F. James and R. S. Sternberg, The Design of Optical Spectrometers, Chapman and Hall, 1969, Section 5.9) and geometrical aberrations on the optical system.

All wavenumbers (spectrometer channels) have been reduced to first order, so that the maximum is 669.10 cm^{-1} (Channel 10), the minimum 509.67 cm^{-1} (Channel 13), and the mean 629.885 cm^{-1} . In addition, we have assumed that the spectrum is centered with respect to wavenumber, i.e., that the incidence and diffraction angles are equal at the mean wavenumber. We then have

$$\sin i = \frac{m}{2a \nu_m}$$

where ν_m is 629.885 cm^{-1} . For high grating efficiency, i must be at or close to the blaze angle of the grating (which also becomes the angle at which the grating is set in an Ebert mounting). The diffraction angle for any other wavelength is then the solution to

$$\sin r = \frac{m}{a} \left(\frac{1}{\nu} - \frac{1}{2\nu_m} \right).$$

3.1.1.1 Throughput

The optical throughput or area - (projected) solid angle product of the spectrometer is given by

$$T = A \Omega = \left(\frac{w}{f} \right) \cdot \left(\frac{l}{f} \right) \cdot A_g$$

where w = width of entrance slit
 l = length of entrance slit
 f = focal length of spectrometer
 A_g = projected area of grating.

Now the angle w/f is the element of incidence angle set by the required spectral resolution, according to.

$$\Delta i = \frac{w}{f} = \frac{m}{a} \cdot \frac{\Delta \lambda}{\cos i}$$

where $\Delta \lambda = \Delta v/v^2$ is the wavelength band of the spectrometer.

We see that the entrance slit defines a fixed spectral element in terms of wavenumber. And because we require a fixed wavenumber band (0.5 cm^{-1}) throughout the spectrum, we must set Δi for the maximum wavenumber. This gives us

$$\Delta i = \Delta i_{10} = \frac{m \Delta v}{a v_{10}^2 \cos i}$$

where v_{10} equals 669.10 cm^{-1} (Channel 10). The image of the entrance slit and the exit slit (field lens aperture) then have equal widths at this maximum wavenumber. At all other (smaller) wavenumbers, the wavenumber band must be set by the exit slit, which then has a width greater than that of the image slit. (Note that the spectral width is set by the larger of the exit slit or the entrance slit image).

Next, consider the angle l/f subtended by the slit height. This is determined by the closest spaced spectral Channels, 22 and 23, which have 0.5 cm^{-1} center separation (remember, that's in first order terms). As shown in Figure 3.1-1, we can calculate this ratio from two relationships imposed on the detector width w_d in these channels,

$$\frac{w_d}{f'} = \frac{s_g}{f}$$

$$\text{and } w_d = F' f \Delta r_{22.5}$$

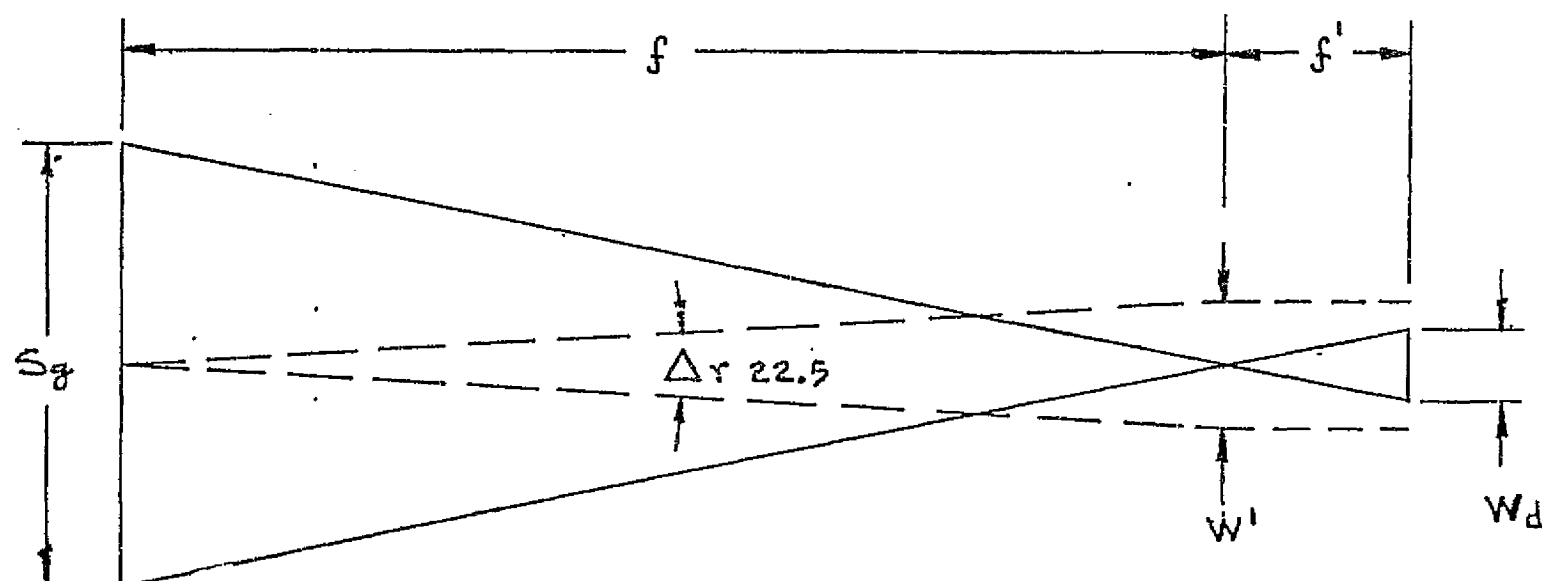
where f' = focal length of field lens

F' = f-number of field lens

$s_g = A_g^{1/2}$ = side of projected grating area

$\Delta r_{22.5}$ = increment of diffraction angle that corresponds to 0.5 cm^{-1} at 597.30 cm^{-1} (mean of Channels 22 and 23, designated 22.5).

FIG. 3.1-1 CONDITIONS IMPOSED ON DETECTOR WIDTH



f = FOCAL LENGTH OF SPECTROMETER

f' = FOCAL LENGTH OF FIELD LENS

S_g = PROJECTED WIDTH OF GRATING

W' = EXIT SLIT WIDTH

W_d = DETECTOR WIDTH

$\Delta r_{22.5}$ = DIFFRACTION ANGLE INCREMENT FOR $\Delta \nu = 0.5 \text{ cm}^{-1}$
AT $\nu = 597.30 \text{ cm}^{-1}$

CONDITIONS:

$$W_d = S_g f' / f$$

$$W_d = f' W' = f' \Delta r_{22.5}$$

The first of these equations is just the geometrical imaging of the grating by the field lens. The second is the requirement that the detector element have a width equal to that of the exit slit times the f-number of the field lens. To prevent overlap with the adjacent channel, F' can be no greater than one. Moreover, an f-number less than one is used to reduce the width of the detector element rather than to increase the length of the slit (see discussion 3.1.1.7). Using the fact that $F' = f'/\ell$, we can solve the above equations to give us

$$\frac{\ell}{f} = \frac{f \Delta r_{22.5}}{s_g}$$

The throughput is now given by

$$T = \Delta i_{10} \Delta r_{22.5} s_g f = w \Delta r_{22.5} s_g$$

Note that for a given grating (given a , i , and s_g), both Δi_{10} and $\Delta r_{22.5}$ are fixed. In this case, the throughput is set by the focal length of the spectrometer. That is, a larger instrument has a larger throughput. Thus, if the focal length were increased by 2X, the slit width would also increase by 2X, but the slit length would increase by 4X. The result is to increase the throughput by 2X. There is, of course, a limit on the angle ℓ/f imposed by either geometrical aberrations or spectral resolution (James and Sternberg, op. cit., pp 67 and 69). However, as shown below, the f/ℓ ratio in our design is less than 0.01 in all cases and is therefore not even close to its limiting value.

For purposes of our study, we have considered gratings in which a^{-1} is 600 cm^{-1} , 750 cm^{-1} , and 800 cm^{-1} , with 800 cm^{-1} taken to be the nominal design value. In addition, we have fixed the focal length f of the spectrometer at a nominal value of 762 m.m. and selected a grating in which s_g is 15.4 cm, for a spectrometer f-number f/s_g of 4.95. The resultant throughputs are listed in Table 3.1-1, together with the incidence angle i and the refraction angle $r_{22.5}$.

Table 3.1-1
Throughput of Spectrometer**

a^{-1}	i	$r_{22.5}$	T
600 cm^{-1}	28.443°	31.887°	$0.88 \times 10^{-3} \text{cm}^2 \text{ster}$
750	36.537	41.323	1.71
800*	39.423	44.775	2.14

* nominal value

** conditions on following page

$$f = 76.2 \text{ cm}; s_g = 15.4 \text{ cm}$$

$$m = 1; \Delta v = 0.5 \text{ cm}^{-1}; v_{22.5} = 597.30 \text{ cm}^{-1}$$

$$v_m = 629.885 \text{ cm}^{-1}$$

3.1.1.2 Entrance Slit Width

The entrance slit width for a fixed focal length is given by

$$w = f \Delta i_{10}$$

The values for the three grating constants are given in Table 3.1-2, together with the incidence angle element Δi_{10}

Table 3.1-2
Incidence Angle Element and Entrance Slit Width

a	Δi_{10}	w
600 cm^{-1}	0.76209×10^{-3}	0.58 m.m.
750	1.0425	0.79
800	1.1566	0.88

$$f = 76.2 \text{ cm}; s_g = 15.4 \text{ cm}$$

$$m = 1; \Delta v = 0.5 \text{ cm}^{-1}$$

$$v_{10} = 669.10 \text{ cm}^{-1}; v_m = 629.885 \text{ cm}^{-1}$$

3.1.1.3 Slit Length

The slit length can be calculated from

$$l = f^2 \Delta r_{22.5} / s_g$$

The values are shown in Table 3.1-3, together with the angle l/f subtended at the grating.

Table 3.1-3
Slit Length

a^{-1}	l	l/f
600 cm^{-1}	3.73 mm	4.90×10^{-3} radian
750	5.28	6.925
800	5.955	7.81

$$m = 1; \Delta v = 9.5 \text{ cm}^{-1}; v_{22.5} = 597.30 \text{ cm}^{-1}; v_m = 629.885 \text{ cm}^{-1}; s_g = 15.4 \text{ cm}; f = 76.2 \text{ cm}$$

The telescope lens in front of the spectrometer must project the slit length onto the ground at nadir at a size of 45 km. Its focal length f_t must then satisfy

$$\theta_l = 45 \text{ km} / 833 \text{ km} = l / f_t,$$

where θ_l is the field of view that corresponds to a resolution element (54.0 μr or 3.09°) and 833 km is the nominal altitude of a Tiros-N spacecraft. For a slit length of 5.955 mm, we have

$$f_t = 110.23 \text{ mm}.$$

In addition, the aperture of the telescope lens must be sufficient to fully illuminate the grating area. In particular, a circular lens aperture must have a diameter D_t that satisfies

$$\frac{D_t}{\sqrt{2} s_g} \geq \frac{f_t}{f} \quad \text{or} \quad D_t \geq 31.505 \text{ mm}.$$

Based on the diagonal of the projected grating area, the f-number of the telescope is 3.50.

3.1.1.4 Spectrum Length

The length of the spectrum is given by

$$L = f [\tan (r_{13} - r_m) + \tan (r_m - r_{10})] .$$

The values are listed in Table 3.1-4, together with the diffraction angles for Channels 10, 13 and the mean wavenumber.

Table 3.1-4
Length of the Spectrum

a^{-1}	r_{13}	r_m	r_{10}	L
600 cm^{-1}	32.651°	28.443°	24.863°	103.74 mm
750	42.407	36.537	31.706	142.74
800	46.001	39.423	34.097	158.91

$$m = 1; \nu_{13} = 590.67 \text{ cm}^{-1}; \nu_m = 629.885 \text{ cm}^{-1}; \nu_{10} = 669.10 \text{ cm}^{-1}$$

3.1.1.5 Exit Slit (Field Lens Aperture) Widths

Each channel has an exit slit (field lens aperture) whose width subtends a spectral band of 0.5 cm^{-1} . The physical size of this width is given by

$$w' = f \Delta r = f \frac{m \Delta \nu}{a \nu^2 \cos r} .$$

The widths for the maximum, mean, and minimum wavenumber are given in Table 3.1-5. The increase in width with decrease in wavenumber is the result of two effects, the increase in angular magnification of the grating ($\Delta r / \Delta i = \cos i / \cos r$) and the increase in slit width needed for a $\Delta \nu$ of 0.5 cm^{-1} (i.e., the increase in $\Delta \lambda$).

Table 3.1-5
Exit Slit (Field Lens Aperture Widths)*

a^{-1}	w'_{10}	w'_m	w'_{13}
600 cm^{-1}	0.563 mm	0.655 mm	0.778 mm
750	0.750	0.896	1.109
800	0.822	0.994	1.258

* Conditions on following page

$$m = 1; \Delta v = 0.5 \text{ cm}^{-1}; f = 762 \text{ mm}$$

$$v_{10} = 669.10 \text{ cm}^{-1}; v_m = 629.885 \text{ cm}^{-1}; v_{13} = 590.67 \text{ cm}^{-1}$$

Although some of the slit widths are less than 1 mm, namely those on the higher frequency side of the mean, all the field lenses in the nominal design can be made 1 mm or more in width. The exit slit width applies to the aperture stop in front of the field lens, so that the minimum lens width is set by the spacing of the channels rather than by their individual widths. The minimum physical spacing is between Channels 7 and 8, which have the properties listed in Table 3.1-6. The distance between the centers of these channels is approximately equal to

$$\frac{0.7}{0.5} \times \frac{1}{2} (0.833 + 0.830) = 1.164 \text{ mm}.$$

Thus 1 mm wide lenses can be used at a separation of about 0.16 mm or 0.0063 in. Note also that the detector width exceeds the exit slit width in Channels 7 through 10.

Table 3.1-6
Nominal First-Order Spectrometer Values*
for
Channels 7 and 8

Channel	v	r	w'
7	666.20 cm^{-1}	34.458 ⁰	0.833 mm
8	666.90	34.371	0.830

* For $a = 800 \text{ cm}^{-1}$

For a grating constant of 750 cm^{-1} , the distance between the centers of channels 7 and 8 is still greater than 1 mm (1.061 mm). However, for a grating constant of 600 cm^{-1} , this distance is less than 1 mm (0.795 mm), which indicates the need for a greater focal length and therefore a larger instrument.

3.1.1.6 Detector Width

The width of a detector element is given by

$$w_d = F' f \Delta r_{22.5}$$

where $\Delta r_{22.5} = \frac{m \Delta v}{a v_{22.5}^2 \cos r_{22.5}}$

and $F' = 0.7.$

The resultant detector widths are listed in Table 3.1-7 for the fixed focal length f of 762 mm.

Table 3.1-7
Detector Element Widths

a^{-1}	$r_{22.5}$	$\Delta i_{22.5}$	w_d
600 cm^{-1}	31.887 ⁰	9.9033×10^{-4}	0.528 mm
750	41.323	1.3996×10^{-3}	0.747
800	44.775	1.5794×10^{-3}	0.842

3.1.1.7 Discussion

If we delete the fixed parameters m , Δv , v_{10} , and $v_{22.5}$ from the throughput equation, we find that it is proportional to the following factors

$$T \propto \frac{s_g f}{a^2 \cos i \cos r_{22.5}}$$

This shows that we can obtain a greater throughput by means of a larger focal length f , a larger grating s_g , or more grooves per unit length a in the grating. The last of these also reduces $\cos i$ and $\cos r_{22.5}$ and thereby further increases the throughput.

We may also note that without the fixed parameters, the detector width is proportional to

$$w_d \propto \frac{F' f}{a \cos r_{22.5}}$$

so that the throughput proportionality can also be stated as follows

$$T \propto \frac{s_g w_d}{F' a \cos i}$$

At the same time, it is well to establish just how the throughput influences the sensitivity of the instrument. In the case of the shortwave (In Sb) channels, the maximum allowable noise current (minimum signal current) increases in direct proportion to T . The background noise current, on the other hand, is proportional to T^2 , so that a larger throughput allows a greater noise input from other sources and thereby relieves the design requirements on the preamplifier.

In the longwave (HgCdTe) channels, however, the system D_v^* is proportional to

$$D_v^* \text{ (system)} \propto \frac{w_d}{T} \propto \frac{F' a \cos i}{s_g}$$

As a result, the longwave channels benefit from a greater throughput only if it is obtained by an increase in a or s_g , i.e., only by changes in the grating itself. A longer focal length or its equivalent of a larger detector width does not help the longwave channels. This is a consequence of the fact that they are limited by internally generated noise that is proportional to w_d but independent of T . In fact, in the HgCdTe channels, there is an advantage in smaller detector elements. A smaller element has a larger responsivity at a given bias dissipation or, conversely, a smaller bias dissipation at a given responsivity.

From the standpoint of the complete instrument, the best way to increase throughput is therefore to increase a^{-1} , s_g , or both, a change that improves the sensitivity of all channels. In fact, the grating parameters appear as the combination $s_g/a \cos i$, which is just the total number of grooves along the length of the grating.

If the reduction in field lens f-number (F') below one were used to increase the slit length rather than to reduce the detector width, the throughput T would be increased by the factor $1/F'$. At the same time, the proportionality for D_v^* (system) would be unchanged from the above expression. Thus it would seem that the longwave (HgCdTe) channel sensitivity is insensitive to the manner in which the reduced field lens f-number is used (smaller detector or larger slit length). At the same time, the shortwave (In Sb) channels would benefit from a greater throughput, although a smaller w_d would reduce the amplifier noise as a result of the decrease in detector capacitance. In fact, however, the longwave channels

benefit greatly from a reduction in the detector width as a result of interaction with the radiant cooler. For a given responsivity (e.g., the level necessary to reduce the influence of preamplifier noise to a negligible level), a smaller detector requires less bias current, in proportion (at least theoretically) to w_d^{-2} . The joule heat on the second stage is therefore also reduced (in proportion to w_d^{-4} at a fixed detector resistance). The reduction in joule heat input, in turn, allows a reduction in operating temperature. A lower temperature not only increases the detector D^* , but also decreases the detector resistance and increases the detector responsivity, which allows a further decrease in detector bias.

Finally, the smaller detector area reduces the capacitance of the InSb elements (as mentioned above), which allows an increase in chopper frequency with no change in the noise level of the InSb preamplifiers. And the increase in chopping frequency benefits the HgCdTe channels by reducing the low frequency (1/f) noise contribution in these detectors.

3.1.2 Optical Performance

The scale factor of the optical system was limited on the one end by the desire to maintain a minimum field lens width of one m.m. (which implies a long focal length mirror and the maximum feasible grating dispersion) and on the opposite end by a desire to keep the mirror focal length to a maximum of 3/4 meter. The result was to select a special plane grating with about 80 grooves per m.m. and a blaze angle of $\sim 40^\circ$ for a blaze wavelength of $16.4 \mu\text{m}$; the O.R.A. optical analysis was performed using a 75 grooves per m.m. grating blazed at 38.7° at $16\mu\text{m}$. Other characteristics of the Ebert-Fastie spectrometer are listed in Table 3.1-8.

Table 3.1-8
Spectrometer Characteristics (O.R.A. Design)

A.	Grating	75 grooves/MM, 38.7° blaze angle at 16μ
B.	Focal Length	762 MM
C.	Mirror	Hyperboloid with higher correction to improve spectral purity
D.	F-Number	5.0
E.	Blur spot diameter	$\sim 0.2 \text{ MM}$
F.	Projected area of grating	6" x 6"

Ray traces were made for channels 2, 10 and 13 since channel 2 is near the center of the useful spectrum and channels 10 and 13 are the extremes. Blur spot diameters at the spectrometer exit slits were about 0.2 m.m. for 90% of the rays; since this is about 1/5 of the width of the exit slits the spectral contours should be very good. The location of the centers of the exit slits are given in Table 3.1-9; the length of the spectrum for the O.R.A. design is 143.337 m.m. It should be noted that the dispersion changes across the spectrum, for example channels 7 and 8 which are separated by 0.7 cm^{-1} in wavenumber are physically separated by 1.069 m.m. between centers at the exit slit position; thus 0.5 cm^{-1} would correspond to 0.764 m.m. width. Channels 22 and 23, which are 2.0 cm^{-1} apart in 4th order or 0.5 cm^{-1} equivalent in 1st order, are physically separated by 1.075 m.m. between centers.

Optical modeling data for the Ebert spectrometer is given in Tables 3.1-10A and B. The collimating - focusing mirror is a hyperboloid with high order corrections to reduce the optical aberrations; no effort was expended to reduce the mirror complexity since the objectives were to prove performance feasibility and to minimize the detector area.

Figures 3.1-2A and B show the layout of the over-under spectrometer configuration in two orthogonal planes (Fig. 3.1-2B is for just one channel). Figures 3.1-3 and 3.1-4 show the optical aberrations at the exit slit for $16\mu\text{m}$ (625 cm^{-1}); the three sets of data from top to bottom represent the top, middle and bottom of the entrance slit along its length (i.e. the object was a point source at the entrance slit). It can be seen from Fig. 3.1-4 that most of the rays are contained in a circle with a diameter of 0.2 m.m. which indicates that the spectral contours should be very good.

Table 3.1-9
Location of Exit Slits, ΔX , for O.R.A. Design

Channel	$\sqrt{\nu}$ cm^{-1}	λ (Microns) Wavelength	Grating Order M	ΔX (MM)
1	607.00	16.47446	1	-34.88324
2	623.23	16.04544	1	- 3.28641
3	627.75	15.92991	1	5.04819
4	635.80	15.72822	1	19.43795
5	646.65	15.46431	1	37.99131
6	652.75	15.31980	1	48.00723
7	666.20	15.01051	1	69.14398
8	666.90	14.99475	1	70.21261
9	668.10	14.96782	1	72.03730
10	669.10	14.94544	1	73.55092
11	1203.00	8.31255	2	-46.20847
12	1231.80	8.11820	2	-17.21957
13	1772.00	5.64334	3	-69.78623
14	1844.50	5.42152	3	-42.83739
15	1889.50	5.29240	3	8.75462
16	1809.50	5.52639	3	-42.83739
17	1839.40	5.43655	3	-22.69211
18	1850.90	5.40278	3	-15.23087
19	1930.10	5.18107	3	32.39529
20	2383.75	4.19507	4	-58.10683
21	2386.10	4.19093	4	-56.83553
22	2388.20	4.18725	4	-55.70338
23	2390.20	4.18375	4	-54.62825
24	2392.35	4.17999	4	-53.47609
25	2394.50	4.17624	4	-52.32764
26	2424.00	4.12541	4	-36.92417
27	2505.00	3.99201	4	2.30324
28	2616.50	3.82189	4	50.23015

10. 6. 56

IMAGE

$$1 + (1 - (1 + i)^{-n}) / r(1 + i)^{-n} \quad Y$$

ORIGINAL PAGE IS
OF POOR QUALITY

A(1)	- .00000000	-2.480713	.0000000	1	-.231454E -9	.321076E -12	.000000E	1
A(2)	0.01000000	0.000000	.0000000	1	.0000000	1	.000000E	1
A(3)	- .00000000	-2.480713	.0000000	1	-.231454E -9	.321076E -12	.000000E	1

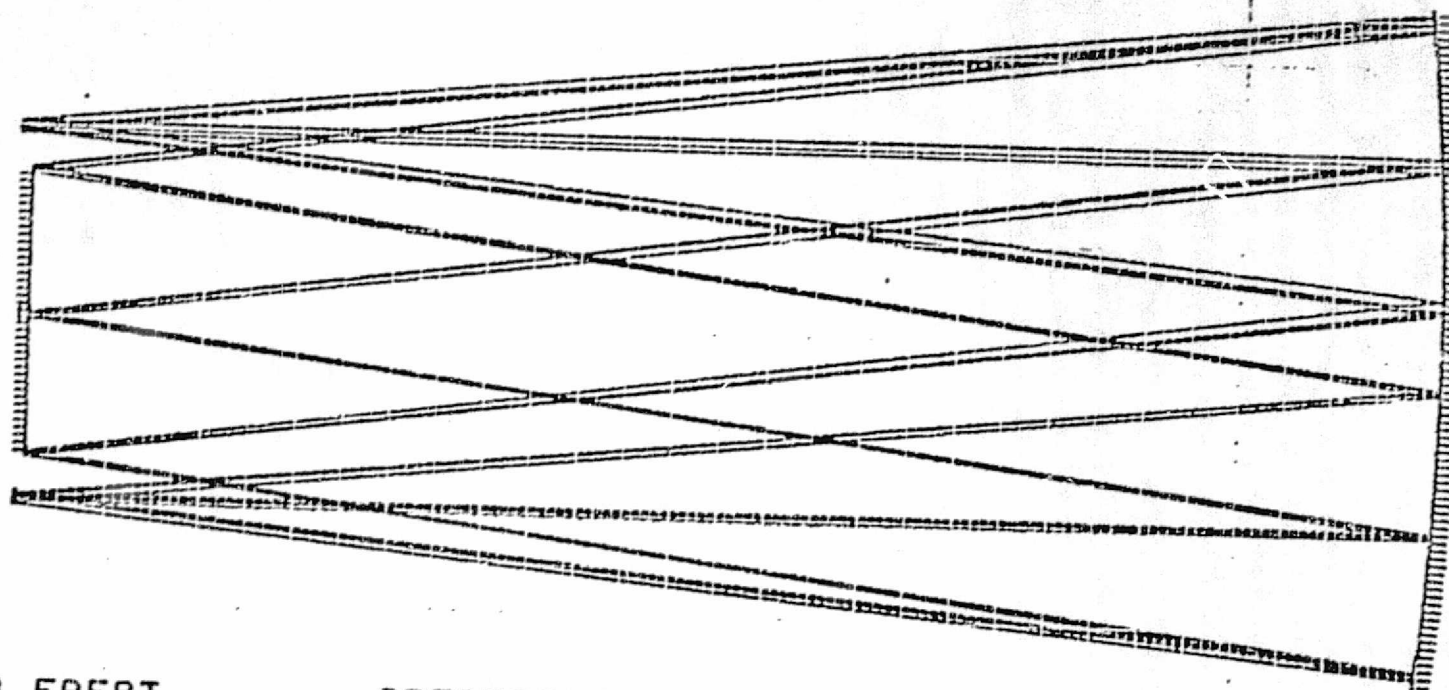
PERCENT	X	Y	Z	ALPH	BETA	GAMMA
P(1)	0.00000	-10.00000	0.00000	0.00000	0.00000	0.00000
P(2)	0.00000	0.00000	0.00000	77.24236	0.00000	0.00000
P(3)	0.00000	0.00000	0.00000	-77.24236	0.00000	0.00000
P(4)	0.00000	-10.00000	0.00000	0.00000	-12.24973	0.00000

```

EF1          = 21.270.7398
EF2          = 26682.6895
FF1          = -21.082.4605
F/F0        = 709.5530
REFLECTION  = 1.0000
FLITTL F/F0 = 5.0001
OBJ DIST    = -187.5006
IMAGE LTST  = -.0002
TOTAL TRACH = .0004
OAI         = 187.5005
SEP1-FIELD  =
  AICLL     = .0002
ENTR PLPIL  =
  DIAMETER  = 37.5000
  DISTANCE  = .00000
EXIT PLPIL  =
  DIAMETER  = 37.7767
  DISTANCE  = -190.3317

```

ORIGINAL PAGE IS
OF POOR QUALITY

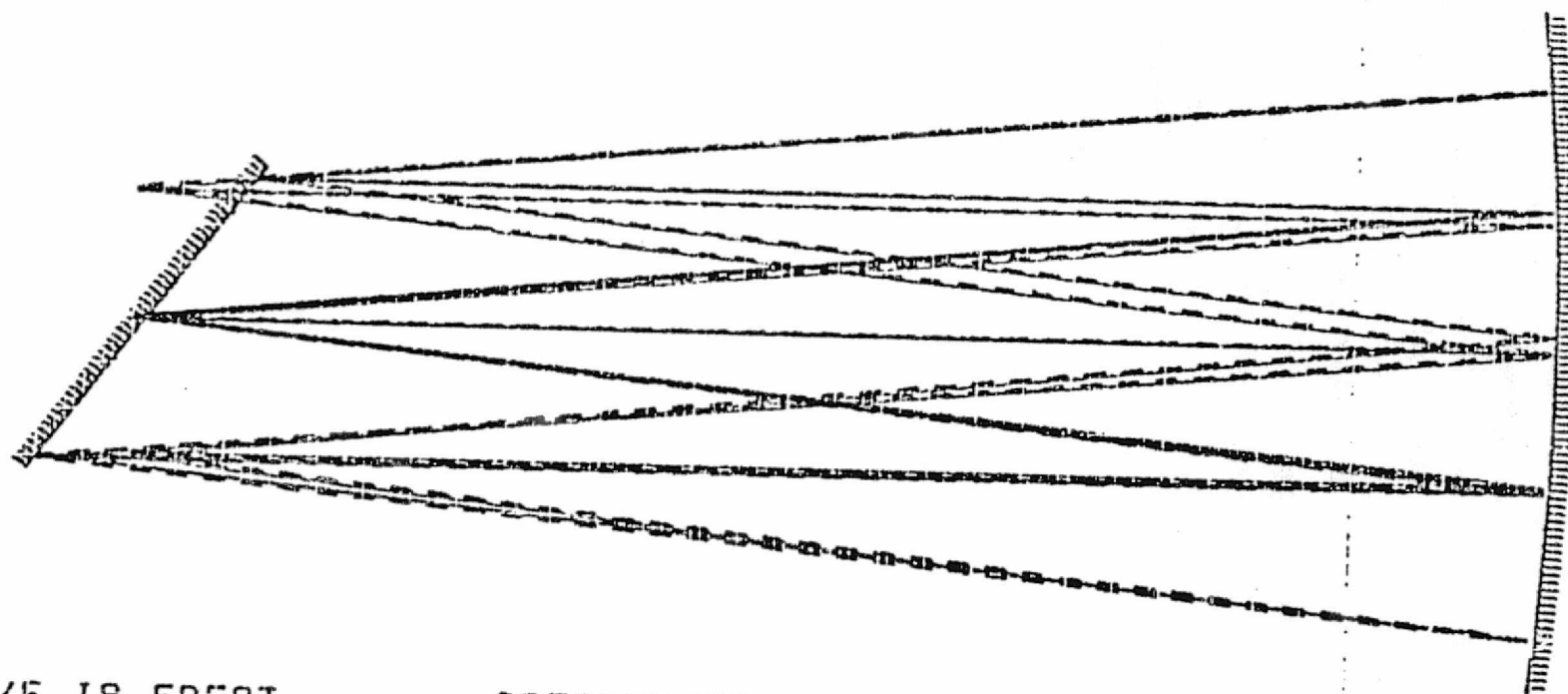


F/5 IR EBERT

SPECTROMETER

SCALE 0.25 CAA 9/2/77

FIG. 3.1-2A



F/5 IR EBERT

SPECTROMETER

SCALE 0.25 GRA 9/2/77

FIG. 3.1-2B

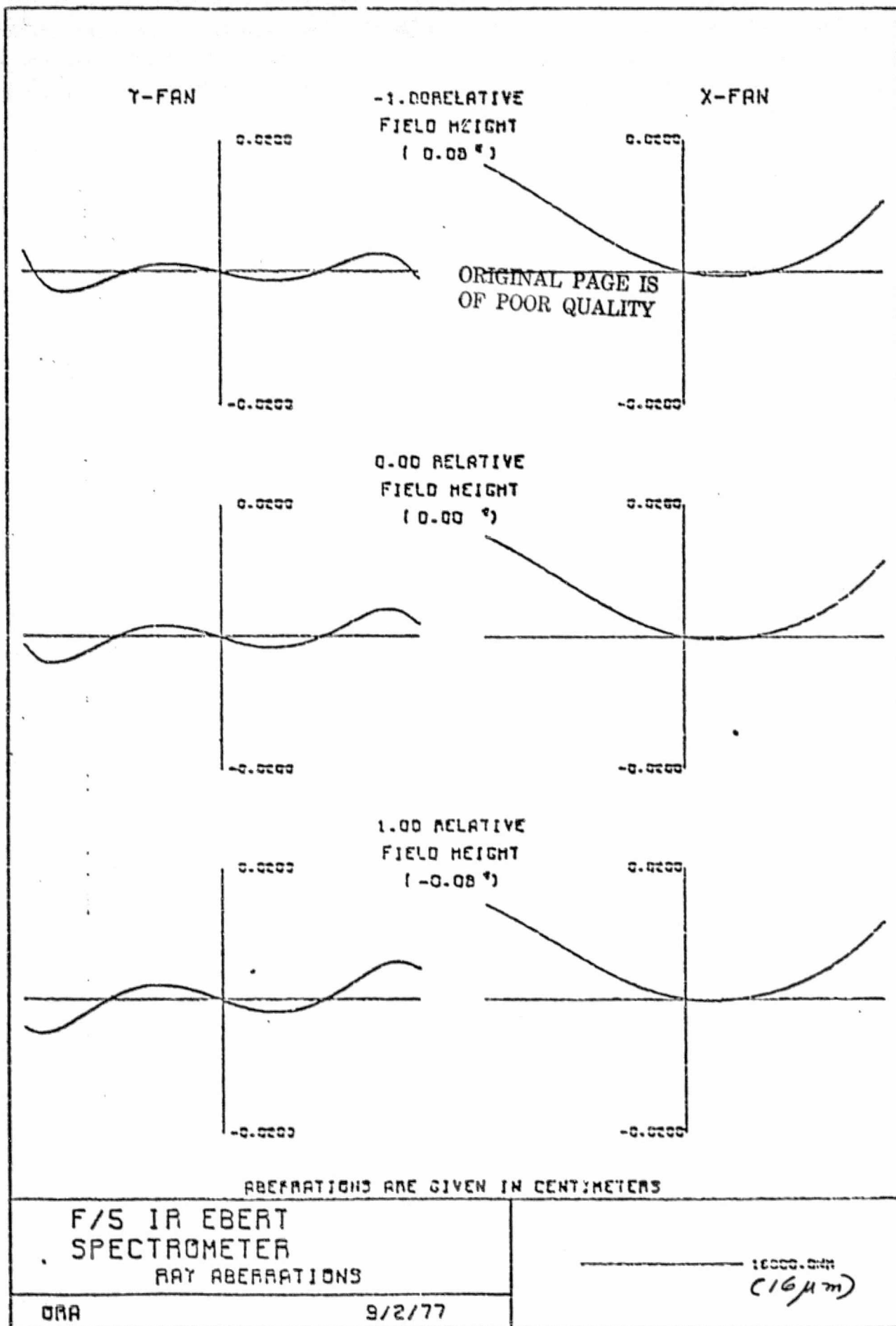


FIG. 3.1-3 SPECTROMETER OPTICAL ABERRATIONS

FIELD POSITION

-1.00
(0.089)

0.00
(0.009)

1.00
(-0.089)

ORIGINAL PAGE IS
OF POOR QUALITY

GAA 9/2/77

DEFOCUSING
F/5 IR EBERT

0.00000
SPECTROMETER

SCALE: 1 INCH = 0.02000 CM

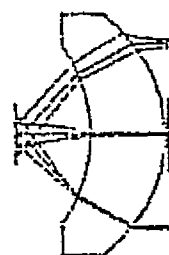
FIG. 3.1-4 SPOT DIAGRAMS AT EXIT SLIT

Ignoring the optical aberrations of the fore-optics, the image of the entrance slit is aberrated by the Ebert mirror and the grating. Over-corrected field curvature is introduced by double reflection from the mirror. This causes the best image of the entrance slit to be focused on a curved focal surface whose radius is equal to the radius of mirror divided by four ($R_M/4$). If a flat focal plane is used to match this image slit, the plane of best blur focus would be tilted 12.24° to the optic axis and tangent to the focal sphere at the middle of the slit image. Another effect observed was the twisting of the exit slit 5.37° about the chief ray at the center of the exit slit. At present, the author has no plausible explanation for the twisting of the exit slit. One possible explanation is that on reviewing the literature on spectrometers, several articles¹ point out that straight line entrance slits are imaged as parabolic images due to oblique incidence from grating normals.

Field lenses were designed to accept the energy passing through each of the exit slits and focus it onto individual detectors for each channel. Originally cadmium telluride was used for the long wavelength channels (1 to 10) but lenses made of this material gave poor performance at the low f-numbers. Consequently germanium was used in all channels because of its superior performance. The absorption of germanium at the long wavelengths is quite small when cooled to 84 kelvins in the thickness required (~2 m.m.). The grating is designed to be the limiting aperture or stop in the optical system, with the field lenses forming an image of the grating on the detector. Figure 3.1-5 shows the shape of the f/0.7, 3.5 m.m. focal length field lenses for channels 2, 10 and 13 and how the rays are focused onto the detectors. Tables 3.1-11, 3.1-12 and 3.1-13 give the optical modeling data for the f/0.7, 3.5 m.m. field lenses using germanium material.

Figures 3.1-6, 3.1-7 and 3.1-8 show the images of the grating at the detector for channels 2, 10 and 13; all images (for one channel) overlay each other but are shown displaced for clarity of presentation. The different images correspond to different points in the field of view which is the same as different points at the spectrometer entrance slit (the telescope lens which images the entrance slit on the earth was not designed in detail for the study effort); the different points at the entrance slit are identified by the illustration in Figure 3.1-9. Radial energy distributions for percent of energy versus spot diameter are given in Figures 3.1-10, 3.1-11 and 3.1-12 for channels 2, 10 and 13 respectively. These figures show that most of the energy can be collected by a 0.85 m.m. x 0.85 m.m. size detector using field

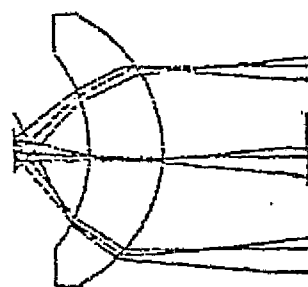
1. J. F. James and R. S. Sternberg, The Design of Optical Spectrometer (London, 1957) p. 64



GE

CHANNEL 2

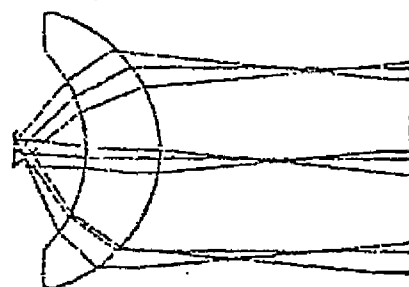
SCALE 5.0
QAR 9/29/77



GE

CHANNEL 10

SCALE 5.0
QAR 9/29/77



GE

CHANNEL 13

SCALE 5.0
QAR 9/29/77

FIG. 3.1-5 FIELD LENS DRAWINGS

9/27/77

CHANNEL 2

ELEMENT	R1	R2	T	CA1	CA2	GLASS
<hr/>						
			APERTURE STOP	5.0000		
1	4.1022	4.2696	1.0000			
			2.0000	5.3020	3.1364	GE
			2.2201			
			-1.030			
IMAGE	MAGNIFICATION =					
	TYPE			.5374		

NOTE - POSITIVE RADIUS INDICATES THE CENTER OF CURVATURE IS TO THE RIGHT
 NEGATIVE RADIUS INDICATES THE CENTER OF CURVATURE IS TO THE LEFT

- DIMENSIONS ARE GIVEN IN MILLIMETERS

LE1	=	3.5000
BE1	=	2.2201
FE1	=	-3.7296
FZFO	=	.7000
GM	=	5.0000
SEMI-FLIP		
APPL	=	4.5900
ENTR PUPIL		
DIAMETER	=	5.0000
DISTANCE	=	0.0000
EXIT PUPIL		
DIAMETER	=	4.6919
DISTANCE	=	-1.0643

ORIGINAL PAGE IS
 OF POOR QUALITY

MODEL DATA

OPTICAL RESEARCH ASSOCIATES

9/27/77

511 531 385

9/27/77

CHANNEL 10

ELEMENT	P1	R2	T	CA1	CA2	GLASS

			APERTURE STOP	5.0000		
1	3.8976	3.8116	3.0000			
			2.0000	5.3142	3.5465	GL
			2.1529			
			-1.1704			
IMAGE	DEFOCUSING =					
	TMF			.5374		

NOTE - POSITIVE RADII INDICATES THE CENTER OF CURVATURE IS TO THE RIGHT
 NEGATIVE RADII INDICATES THE CENTER OF CURVATURE IS TO THE LEFT

- DIMENSIONS ARE GIVEN IN MILLIMETERS

EFL	=	3.5000
BFL	=	2.1529
FFL	=	-3.8775
F/NO	=	.7000
OAL	=	3.0000
SEMI-FIELD		
ANGLE	=	4.3700
ENTR PUPIL		
DIAMETER	=	5.0000
DISTANCE	=	0.0000
EXIT PUPIL		
DIAMETER	=	4.5132
DISTANCE	=	-1.0064

TABLE 3.1-12 FIELD LENS DESIGN FOR CHANNEL 10

1/27/77

CHANNEL 13

ELEMENT	R1	R2	T	CA1	CA2	GLASS

			APERTURE STOP	5.0000		
1	3.8962	3.7990	1.0000			
			2.0000	5.3142	3.5065	GE
			2.1512			
			-1.699			
IMAGE	DEFUSSING =					
	IMP					
					.5374	

NOTE - POSITIVE RADII INDICATES THE CENTER OF CURVATURE IS TO THE RIGHT
 NEGATIVE RADII INDICATES THE CENTER OF CURVATURE IS TO THE LEFT

- DIMENSIONS ARE GIVEN IN MILLIMETERS

EFL	=	3.5000
BFL	=	2.1512
PFL	=	-3.8833
F/NO	=	.7000
OAL	=	3.0000
SEMI-FIELD		
ANGLE	=	4.3900
ENTER PUPIL		
DIAMETER	=	5.0000
DISTANCE	=	0.0000
EXIT PUPIL		
DIAMETER	=	4.5065
DISTANCE	=	-1.0033

ORIGINAL PAGE IS
 OF POOR QUALITY

TABLE 3.1-13 FIELD LENS DESIGN FOR CHANNEL 13

FIELD POSITION

-1.00
(0.00°)

0.00
(0.00°)

1.00
(0.00°)

DEFOCUSING*

-0.05000

-0.02500

-0.00000

0.02500

0.05000

CHANNEL 2

ORIGINAL PAGE IS
OF POOR QUALITY

ORA 9/30/77

SCALE: 1 INCH = 0.10000 CM

FIG. 3.1-6 GRATING IMAGES AT DETECTOR FOR DIFFERENT FIELD POINTS (CH. 2)

FIELD POSITION

-1.00
(0.03°)

0.00
(0.00°)

1.00
(0.03°)

DEFOCUSING -0.05000 -0.02500 -0.00000 0.02500 0.05000

CHANNEL 10

SCALE: 1 INCH = 0.10000 CM

FIG. 3.1-7 GRATING IMAGES AT DETECTOR FOR DIFFERENT FIELD POINTS (CH. 10)

ORIGINAL PAGE IS
OF POOR QUALITY

ORA 9/30/77

FIELD POSITION

-1.00
(0.037)

0.00
(0.007)

1.00
(-0.037)

DEFOCUSING

-0.05000

-0.02500

-0.00000

0.02500

0.05000

CHANNEL 13

SCALE: 1 INCH = 0.10000 CM

ORIGINAL PAGE IS
OF POOR QUALITY

ORA 9/30/77

FIG. 3.1-8 GRATING IMAGES AT DETECTOR FOR DIFFERENT FIELD POINTS (CH. 13)

FIELD POSITION

1.00
-0.037

0.00
10.007

-1.00
10.037

DEFOCUSING

CHANNEL 13

-0.05000

-0.02500

-0.00000

0.02500

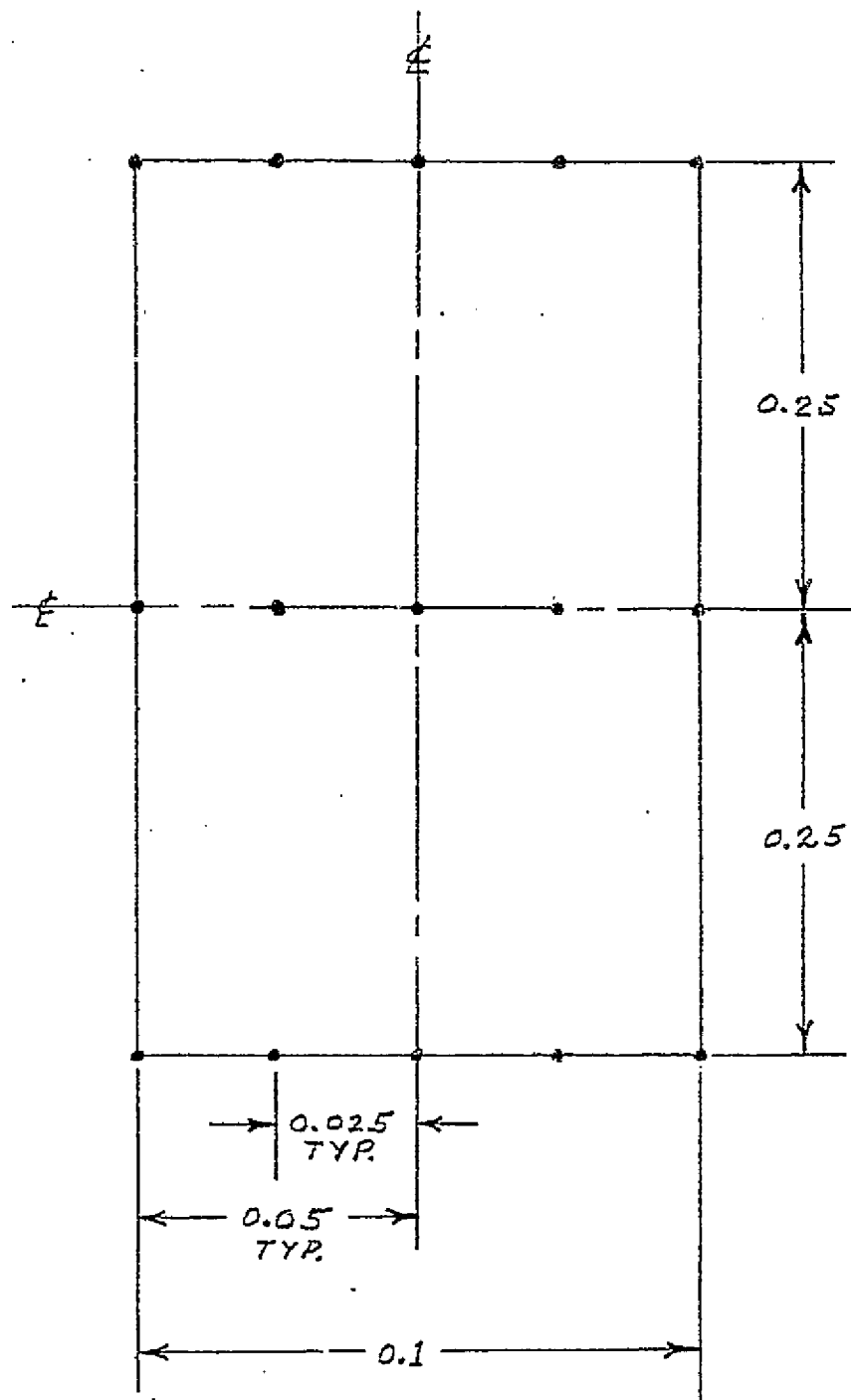
0.05000

SCALE: 1 INCH = 0.10000 CM

FIG. 3.1-8 GRATING IMAGES AT DETECTOR FOR DIFFERENT FIELD POINTS (CH. 13)

ORIGINAL PAGE IS
OF POOR QUALITY

GHA 9/30/77



Dimensions in Centimeters

Fig. 3.1-9 Identification of Field Points (dots) at Entrance Slit

CE/011 2

WAVELLENGTH 16041.4 nm 16045.4 nm 16049.4 nm
WFLIGHT 50 50 50

FOCUS	-0.0000	-0.0000	-0.0000	0.0000	0.0000	0.0000	0.0000
1.00 YR							
0.1 DEG							
10	.124850	.124850	.124850	.124850	.124850	.124850	.124850
20	.124850	.124850	.124850	.124850	.124850	.124850	.124850
30	.124850	.124850	.124850	.124850	.124850	.124850	.124850
40	.124850	.124850	.124850	.124850	.124850	.124850	.124850
50	.124850	.124850	.124850	.124850	.124850	.124850	.124850
60	.124850	.124850	.124850	.124850	.124850	.124850	.124850
70	.124850	.124850	.124850	.124850	.124850	.124850	.124850
80	.124850	.124850	.124850	.124850	.124850	.124850	.124850
90	.124850	.124850	.124850	.124850	.124850	.124850	.124850
100	.124850	.124850	.124850	.124850	.124850	.124850	.124850
1.00 YR							
0.0 DEG							
10	.124850	.124850	.124850	.124850	.124850	.124850	.124850
20	.124850	.124850	.124850	.124850	.124850	.124850	.124850
30	.124850	.124850	.124850	.124850	.124850	.124850	.124850
40	.124850	.124850	.124850	.124850	.124850	.124850	.124850
50	.124850	.124850	.124850	.124850	.124850	.124850	.124850
60	.124850	.124850	.124850	.124850	.124850	.124850	.124850
70	.124850	.124850	.124850	.124850	.124850	.124850	.124850
80	.124850	.124850	.124850	.124850	.124850	.124850	.124850
90	.124850	.124850	.124850	.124850	.124850	.124850	.124850
100	.124850	.124850	.124850	.124850	.124850	.124850	.124850
1.00 YR							
0.1 DEG							
10	.124850	.124850	.124850	.124850	.124850	.124850	.124850
20	.124850	.124850	.124850	.124850	.124850	.124850	.124850
30	.124850	.124850	.124850	.124850	.124850	.124850	.124850
40	.124850	.124850	.124850	.124850	.124850	.124850	.124850
50	.124850	.124850	.124850	.124850	.124850	.124850	.124850
60	.124850	.124850	.124850	.124850	.124850	.124850	.124850
70	.124850	.124850	.124850	.124850	.124850	.124850	.124850
80	.124850	.124850	.124850	.124850	.124850	.124850	.124850
90	.124850	.124850	.124850	.124850	.124850	.124850	.124850
100	.124850	.124850	.124850	.124850	.124850	.124850	.124850

ORIGINAL PAGE IS
OF POOR QUALITY

FIG. 3.1-11

9/20/77

RADIAL DISTANCE
SCT FIBERS (in centimeters)

POSITION

CIRCUIT 10

WAVELENGTH 1494.4 M 14945.4 M 14939.3 M
WEIGHT 50 50 50

FOCUS	-.07500	-.05000	-.02500	0.00000	.02500	.05000	.07500
REL. PCT							
.00 YN							
.01 DEG							
10	.020628	.019475	.019237	.019405	.017470	.030350	.014275
20	.017091	.021332	.019552	.020439	.020610	.020505	.021100
30	.040292	.037564	.033741	.037440	.033406	.027477	.020150
40	.041547	.040509	.042921	.044472	.041400	.027109	.030357
50	.057305	.053065	.059271	.050041	.042702	.041013	.039646
60	.055176	.062080	.055722	.056160	.052501	.043075	.040371
70	.061107	.074490	.068340	.065177	.063015	.053469	.053430
80	.066570	.084173	.079719	.072121	.060102	.051051	.061335
90	.070270	.100511	.094507	.081640	.064650	.051120	.070003
100	.072970	.107222	.100409	.086700	.064101	.053217	.070033
.00 YN							
.00 DEG							
10	.024112	.021717	.024111	.021110	.016631	.011001	.011000
20	.022001	.030115	.022511	.031500	.020400	.012003	.017000
30	.041123	.040295	.039001	.030740	.030020	.021175	.022070
40	.050400	.047536	.047100	.045100	.035700	.025472	.028200
50	.057377	.054360	.052575	.036170	.041203	.033010	.033400
60	.065356	.061170	.059250	.050423	.045325	.045002	.037100
70	.073574	.066130	.063570	.050000	.041270	.040150	.043500
80	.075201	.074537	.069411	.040171	.035130	.030101	.050017
90	.075119	.080032	.077024	.070403	.063200	.061107	.050000
100	.075330	.080110	.075331	.060000	.060000	.050000	.072500
.00 YN							
.01 DEG							
10	.020057	.010015	.022150	.010203	.021000	.017023	.014300
20	.017031	.021007	.013500	.021070	.010000	.021000	.021000
30	.020057	.037011	.031000	.030100	.010000	.030000	.030000
40	.020057	.047011	.042000	.040000	.010000	.040000	.040000
50	.020057	.060011	.052000	.050000	.010000	.050000	.050000
60	.020057	.070011	.060000	.060000	.010000	.060000	.060000
70	.020057	.080011	.070000	.070000	.010000	.070000	.070000
80	.020057	.090011	.080000	.080000	.010000	.080000	.080000
90	.020057	.100011	.090000	.090000	.010000	.090000	.090000
100	.020057	.110011	.100000	.100000	.010000	.100000	.100000

ORIGINAL PAGE IS
OF POOR QUALITY

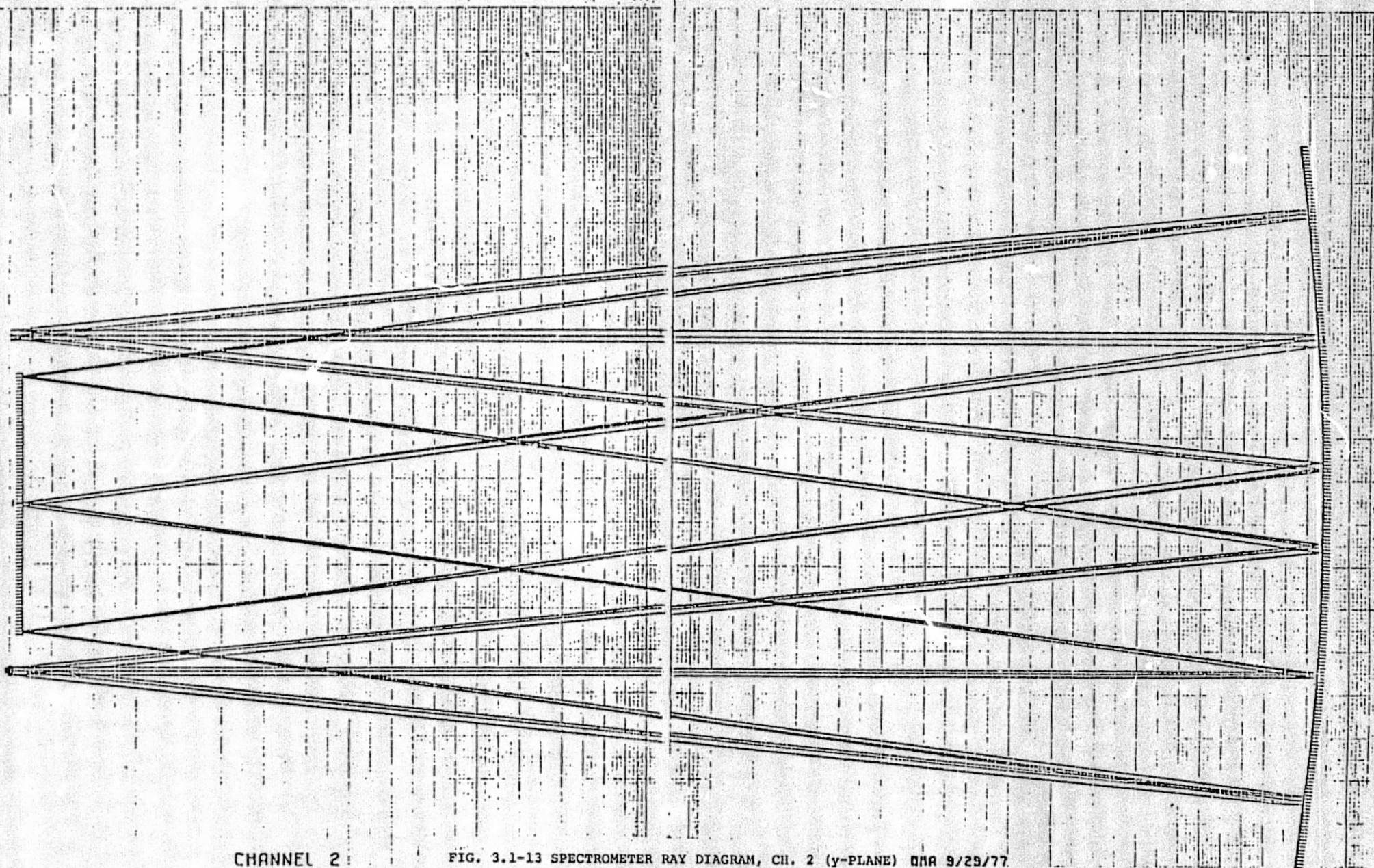
4477

5. 7. 1964 (in centimeters)

ORIGINAL PAGE IS
OF POOR QUALITY

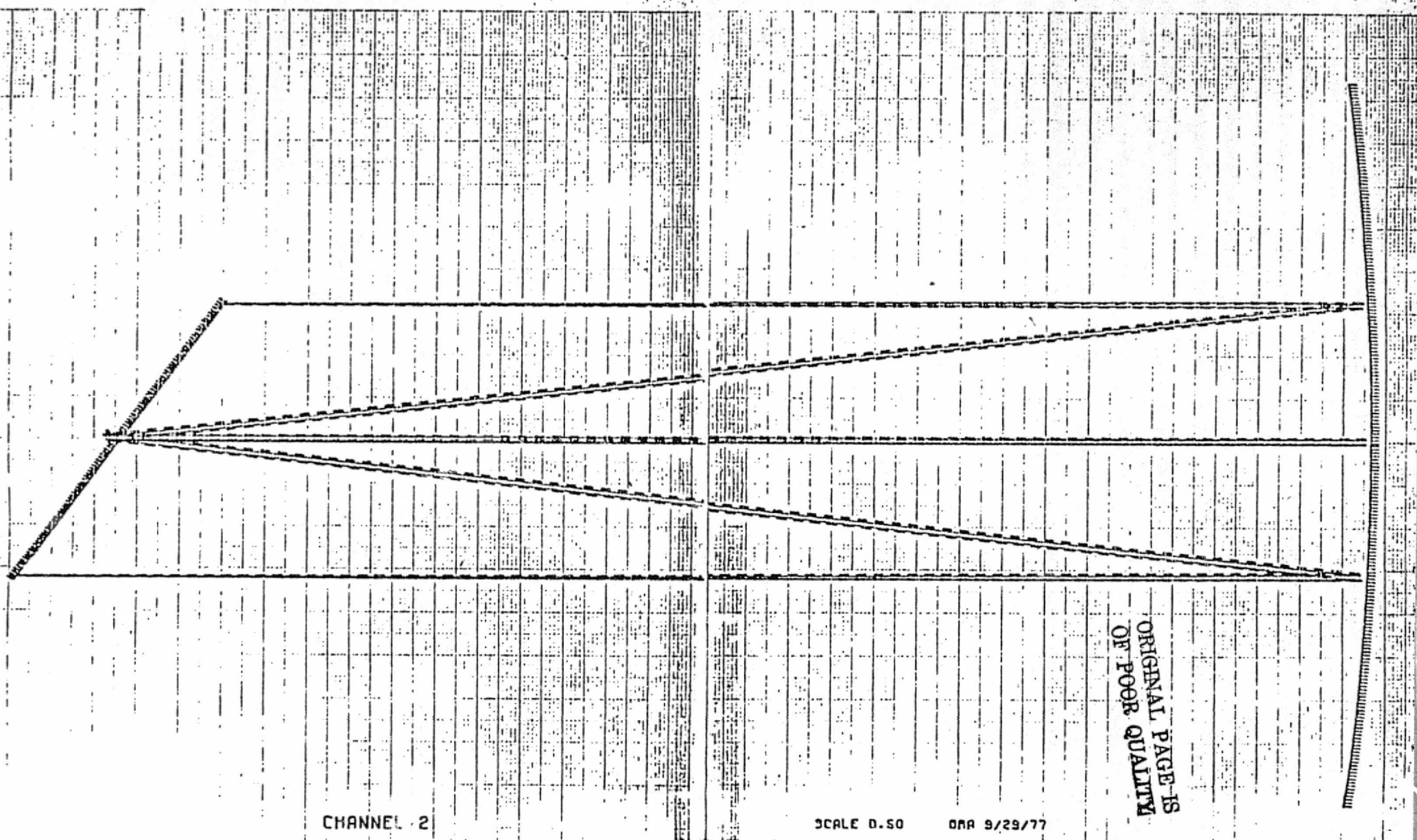
lenses with 3.5 m.m. focal length.

Figures 3.1-13 through 3.1-16 show the spectrometer configuration with field lenses for channels 2, 10 and 13. A flat, rectangular folding mirror (not shown) would be inserted about 3 inches ahead of the spectrometer exit focal plane to direct the optical beam into the radiant cooler.



CHANNEL 2

FIG. 3.1-13 SPECTROMETER RAY DIAGRAM, CH. 2 (y-PLANE) DMR 9/29/77



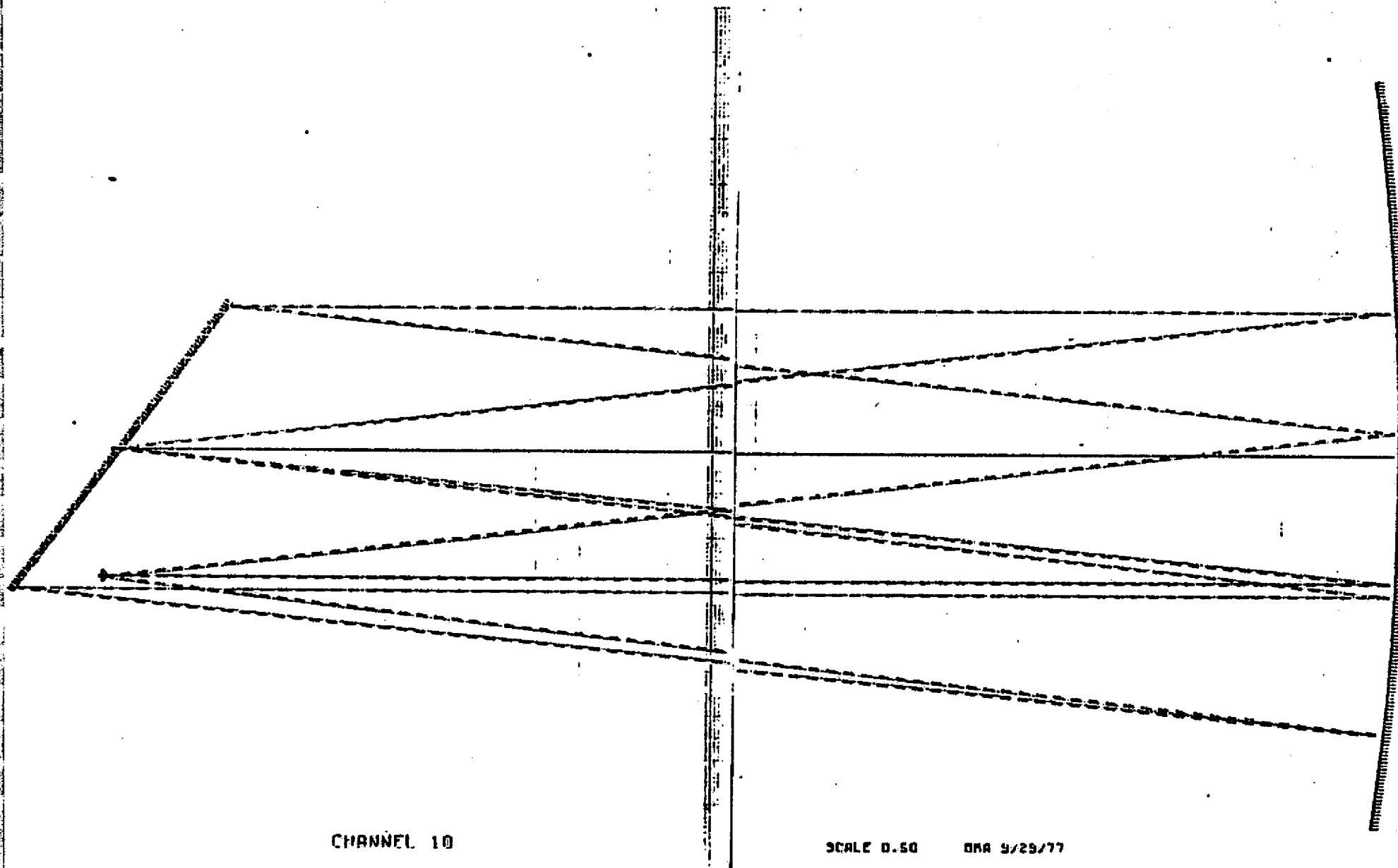
CHANNEL 2

SCALE 0.50

QMA 9/29/77

ORIGINAL PAGE IS
OF POOR QUALITY

FIG. 3.1-14 SPECTROMETER RAY DIAGRAM, CH. 2 (X-PLANE)

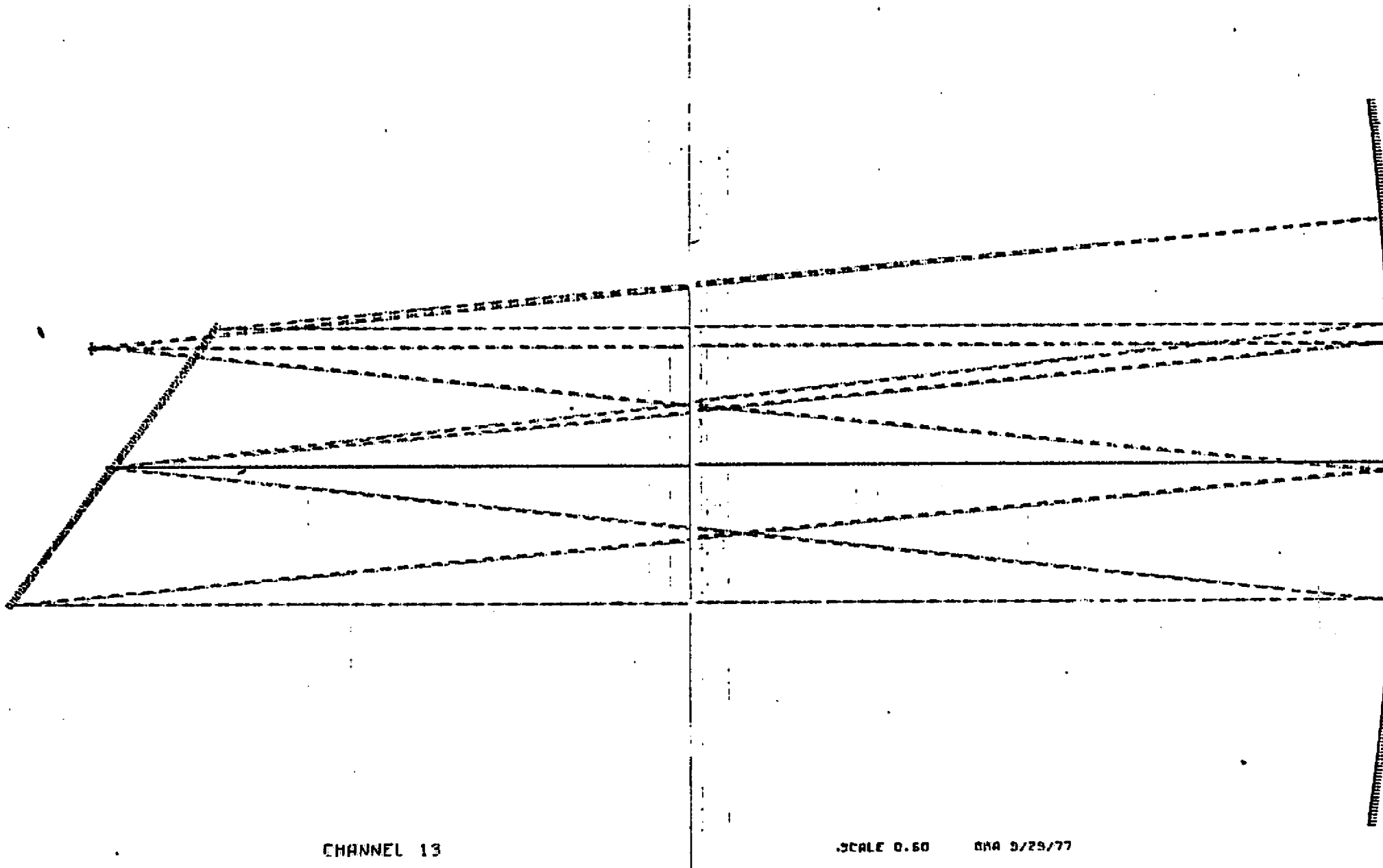


CHANNEL 10

SCALE 0.50

DMR 9/29/77

FIG. 3.1-15 SPECTROMETER DAY DIAGRAM, CH. 10 (X-PLANE)



CHANNEL 13

SCALE 0.50

DATA 9/29/77

FIG. 3.1-16 SPECTROMETER RAY DIAGRAM, CH. 13 (X-PLANE)

3.2

Radiant Cooler

The radiant cooler is designed to maintain the field lens/detector/spectral filter array at an operating temperature of 84K. It is a scaled-up version of the cooler in use on the Advanced Very High Resolution Radiometer (AVHRR, Mods 1 and 2) for the Tiros-N spacecraft (Contracts NAS5-21900, 5-22497 and 5-23400). In particular, all the linear dimensions are 2x those of the AVHRR design, as shown in Fig. 3.2-1. At the same time, the thermal conductance of the mechanical supports is 4x that of the AVHRR/Mod. 1. This is because the thickness of the cooler stages is not increased, so that the mass goes up as the area of the cooler. However, the total thermal conductance has increased by more than 4x as a consequence of the even greater increase in the number of electrical leads into the cooler (e.g., 63 leads to the patch or colder stage compared with 10 on the AVHRR/Mod. 1).

The nominal in-orbit characteristics of the cooler are summarized in Tables 3.2-1 and 3.2-2. We see that the detectors and their associated optical elements operate at 84K with a thermal margin of 35.3mW or 4.5K.

The performance of the radiant cooler is highly insensitive to the orbit normal to sun angle β_s up to the point at which the earth shield is exposed to direct sunlight. For example, the sun angle range of the AVHRR instrument is $0^\circ < \beta_s < 68^\circ$. The exact value of the upper limit depends on the placement of the instrument and the configuration of the spacecraft. Within this range, the maximum cooler temperatures will occur at the angle at which the spacecraft enters and leaves the earth's shadow (27.83° at an altitude of 833 km). For the design described here, the housing (spectrometer) temperature at this angle increases by 2.5K, the first stage by 0.36K, and the second stage by 0.11K.

3.2.1

Cover Temperatures

Both the vertical and horizontal earth shields are insulated from external inputs by shield covers. All the optically polished shields are thermally and mechanically connected. However, the two vertical covers are not connected to the horizontal cover. The cover temperatures are determined by the thermal balance equation given in Fig. 3.2-2. The nominal Tiros orbit corresponds to a sun angle β_s of 37.5° (3:30 PM/8:30 AM) and an altitude of 833 km (nadir to earth-tangent line angle β_e of 62.17°). The resultant cover temperatures are:

$$T_c \text{ (horizontal)} = 238.6K$$

$$T_c \text{ (vertical)} = 190.1K$$

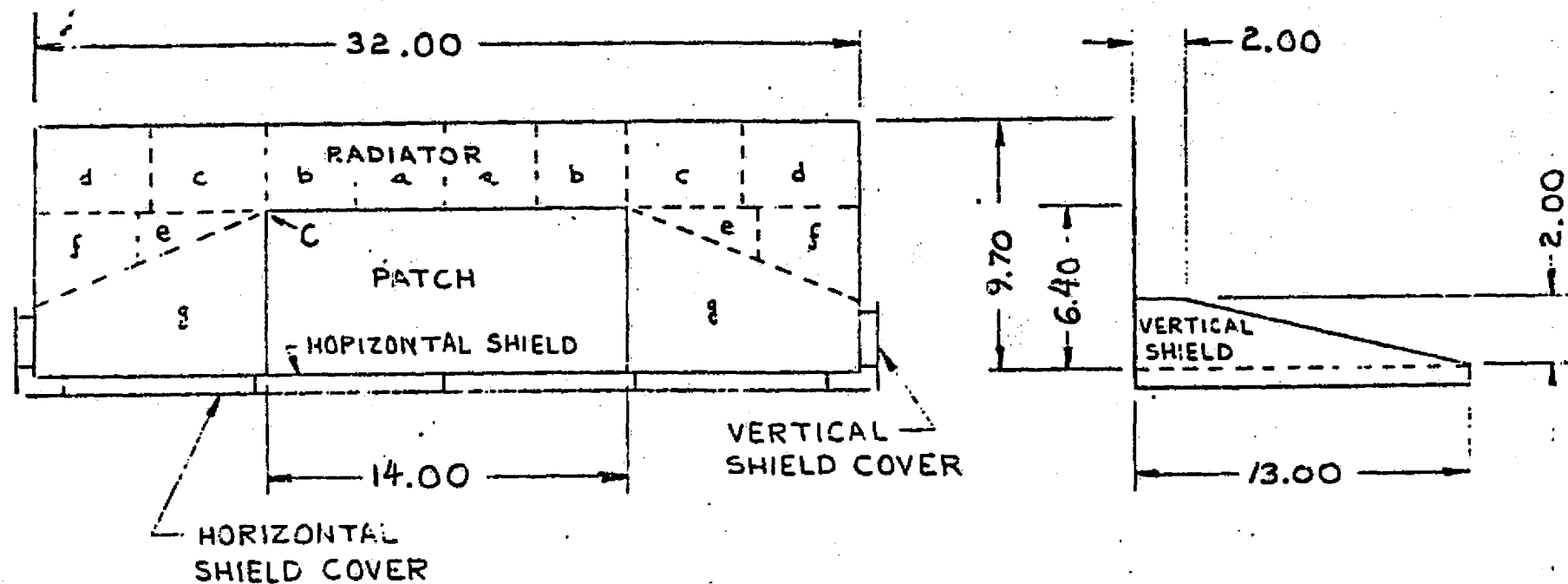


Fig. 3.2-1 Basic Design of Radiant Cooler (Dimensions in Inches)

Table 3.2-1

Nominal Characteristics of the Radiator (1st Stage) (a)

Temperature	153.7K	
Power radiated	4.373W	
Radiating area		220.8 in ²
Conductive input	0.844W	19.3%
Insulation input	0.398	9.1
Earth input	0.793	18.1
Covers input	1.947	44.5
Optical port input	0.341	7.8
Joule heat input	0.050	1.2
$d\phi/dT$ (b)		0.147WK ⁻¹

(a) Cooler housing (spectrometer) at -25°C; spacecraft in normal orbit (833 km altitude, 37.5° orbit normal to sun angle).

(b) Rate of change of input power with temperature at 153.7K.

Table 3.2-2

Nominal Characteristics of the Patch (2nd Stage) (a)

Temperature (b)	84.0K	
Power radiated	158.3 mW	
Radiating area		89.6 in ²
Conductive input (c)	50.7 mW	32.0%
Insulation input	27.2	17.2
Joule heat input	16.1	10.2
Optical port input	4.5	2.8
Shield input	24.5	15.5
Control power (d)	35.3	22.3
dφ/dT		7.35mW/K @ 80K

(a) Cooler housing (spectrometer) at -25°C; spacecraft in nominal orbit (833 km altitude, 37.5° orbit normal to sun angle).

(b) Control point; without control power, temperature decreases to 79.5K (in orbit).

(c) Including effect of support shields.

(d) In-orbit value.

Fig. 3.2-2 Cooler Earth Shield Cover Thermal Balance Equation

$$\epsilon_c \sigma T_c^4 = F_{ce} (\epsilon_c W_e + \alpha_c W_r) + \alpha_c S_o \langle \sin i \rangle,$$

- where
- ϵ_c = emissivity = 0.72 (silvered Teflon)
 - α_c = solar absorptivity = 0.08
 - F_{ce} = view factor from cover to earth; $\sin^2 \beta_e$ for a horizontal cover and $\frac{1}{\pi} (\beta_e - \sin \beta_e \cos \beta_e)$ for a vertical cover, where β_e is the mean angle from nadir to the earth-tangent line.
 - $\langle \sin i \rangle$ = orbital average of the solar incidence angle, taken to be zero when the cover is shaded from direct sunlight; $\frac{1}{\pi} \sin \beta_s (1 - \sin \Delta u_e)$ for a horizontal surface and $\frac{1}{2\pi} \sin \beta_s (1 + \cos \Delta u_e)$ for a vertical surface.
 - Δu_e = $\arccos (\cos \beta_e / \sin \beta_s)$; zero when $\sin \beta_s \leq \cos \beta_e$, i.e., when the spacecraft is in direct sunlight throughout its orbit.
 - W_e = infrared exitance of earth = $2.1 \times 10^{-2} \text{ Wcm}^{-2}$
 - W_r = reflected solar exitance of earth = $1.68 \times 10^{-2} \sin \beta_s \text{ Wcm}^{-2}$
 - S_o = solar constant = 0.14 Wcm^{-2}

3.2.2 Radiator Thermal Analysis

The radiator and earth shield have a temperature T_r that is the solution to the thermal balance equation given in Fig. 3.2-3. The thermal conductance K between the cooler housing and the first stage of cooling consists of $6.90 \times 10^{-3} \text{ WK}^{-1}$ from the synthane support tubes and $2.05 \times 10^{-3} \text{ WK}^{-1}$ from the electrical leads listed in Table 3.2-3. All the leads are 3.0×10^{-3} inch diameter copper except those for the outgas heaters, which are 5.0×10^{-3} inch diameter copper. All the leads have a free length of 4.50 inches between the housing and radiator.

Table 3.2-3

Electrical Leads Between the Cooler Housing and Radiator

<u>Function</u>	<u>Quantity</u>
HgCdTe leads	$2 \times 12 = 24$
InSb pre-amp fronts	$5 \times 16 = 80$
InSb common	1
Temperature sensors	$2 \times 2 = 4$
Outgas heaters	$2 \times 2 = 4$
Patch control heater	2
	<hr/> 115

In order to operate the second stage (patch) at a controlled temperature of 84K, we must have a first stage (radiator) temperature that approaches 150K. At the same time, however, we must avoid going below 150K in order to ensure that the low-emissivity earth shield surfaces will not be contaminated by condensation of water vapor from the spacecraft atmosphere. In order to reach the desired temperature range, we have replaced the multilayer insulation blanket (between the housing and the radiator) used on the AVHRR radiant coolers with a close-spaced geometry of gold-plated metallic shields, as described by Annable (Appl. Opt. 15, 1860, 1976).

The solution to the equation described in Figure 3 is

$$T_r = 153.7\text{K}$$

under the conditions of the nominal orbit.

Fig. 3.2-3 Cooler First Stage Thermal Balance Equation

$$\epsilon_r \sigma A_r T_r^4 = \phi_{er} + \phi_{cr} + \phi_i + \phi_k + \phi_o + \phi_p$$

• where ϕ_{ab} = radiant power from a that is absorbed in b

e = earth (infrared and reflected sunlight)

r = black radiator, c = shield covers

ϕ_a = input from instrument through a

i = multilayer insulation; k = supports and wires;
o = optical port; p = InSb preamplifier fronts.

$$\phi_{er} = F_{re} (\epsilon_r W_e + \alpha_r W_r) A_r$$

$$\phi_{cr} = \frac{\sigma A_c}{S_c} (T_c^4 - T_r^4) + K_c (T_c - T_r) \text{ for each cover}$$

F_{ab} = view factor from a to b; A_a = area of a

ϵ_a = emissivity of a; α_a = solar absorptivity of a

W_e = earth infrared exitance = $2.1 \times 10^{-2} \text{ Wcm}^{-2}$

W_r = earth reflected sunlight exitance

= $1.68 \times 10^{-2} \sin \beta_s \text{ Wcm}^{-2}$; β_s = orbit normal to
sun angle = 37.5° (nominal)

A_c (horizontal) = 416 in^2 ; A_c (2 vertical) = 30.0 in^2

A_r = 220.8 in^2 ;

F_{re} = 0.01837 (833 km), computer
calculation

ϵ_r = α_r = 0.97 (honeycomb cavity array covered with
black paint)

S_c = $\frac{2}{\epsilon_c} - 1$; ϵ_c = emissivity of gold plating on
facing surfaces of shield and cover = 0.035.

K_c = thermal conductance of supports between shield
and cover

= $10.64 \times 10^{-3} \text{ WK}^{-1}$ (horizontal),

= $8.28 \times 10^{-3} \text{ WK}^{-1}$ (2 vertical)

Fig. 3.2-3 (Continued)

Cooler First Stage Thermal Balance Equation

T_C = cover temperature = 238.6K (horizontal), 190.1K (vertical) in nominal orbit.

$$\phi_i = \frac{\sigma A_i}{S_i} (T_h^4 - T_r^4); A_i = 440 \text{ in}^2$$

S_i = insulation factor of gold-plated shields between housing and radiator = $(n + 1) \times$

$$\left(\frac{2}{\epsilon_i} - 1 \right); \epsilon_i = \text{emissivity of gold}$$

plating on surfaces = 0.045; n = number of intermediate shields = 2.

T_h = housing temperature = 248K (-25°C)

$\phi_k = K_r (T_h - T_r); K_r$ = thermal conductance between h and $r = 8.95 \times 10^{-3} \text{ WK}^{-1}$

$\phi_o = 0.341 \text{ W}$ (Section V)

$\phi_p = 0.050 \text{ W}$

3.2.3 Patch Thermal Analysis

The thermal balance equation for the patch is the solution to the equation described in Figure 3.2-4. The joule heat consists of 1.0 mW for each HgCdTe detector in Channels 2 through 12, 4.0 mW for the detector in Channel 1, and 1.1 mW for the temperature sensor. The optical port loading is for a nominal baseplate temperature of -25°C . The thermal conductance K between the radiator and patch consists of $4.750 \times 10^{-4} \text{ WK}^{-1}$ from the mechanical supports plus $1.470 \times 10^{-4} \text{ WK}^{-1}$ from the electrical leads (63,0.0030 inch diameter nickel wires wound around the supports for 6.00 inches of free length).

The dual heat mode multiplier, M , was calculated by the technique described in the Technical Description of AVHRR/Mod 1 (Rev. B, Nov. 15, 1974, memorandum at the end of Section 6.0). A shield emissivity, ϵ_s , of 0.035 was used in the calculation and the analysis was carried out for the shield at the radiator temperature (i.e., the thermal gradient was evaluated at $x = l$). In addition, a support length of 2.00 inches was assumed.

At the nominal radiator temperature of 153.7, the patch has a temperature of

$$T_p = 79.5\text{K}$$

Operation at a control point of 84.0 then provides a nominal thermal margin of 4.5 or 35.3 mW.

The equation in Figure 4 does not include the input present during chamber testing as a result of reflection of the radiator power from the cold space target. Based on thermal tests and their analyses (Section 6.7 of the AVHRR Mod 1 Technical Description), we estimate this input to be given by

$$3.0 \times 10^{-2} \left(\frac{T_r}{164} \right)^4 \text{ W}$$

for the 89.6 in^2 black radiating area. Under nominal conditions, this input is $23.1 \times 10^{-3} \text{ W}$ and increases the uncontrolled patch temperature to 82.5K, an increase of 3.0K.

$$\sigma \epsilon_p A_p T_p^4 = \phi_s + \phi_k + \phi_i + \phi_j + \phi_o$$

- where
- p = patch
 - s = earth shield (upper side)
 - k = thermal conductance including the influence of radiative inputs from the support shields
 - i = gold-to-gold radiative insulation
 - j = joule heat of detectors and temperature sensor
 - o = optical port
 - $\phi_s = \sigma \epsilon_p \epsilon_s A_p F_{ps} T_r^4$
 - $\phi_k = M K_p (T_r - T_p)$; M = dual mode multiplier
 - $\phi_i = \frac{\sigma A_i}{S_i} (T_r^4 - T_p^4)$; $S_i = \left(\frac{2}{\epsilon_i} - 1 \right) (n + 1)$;
n = number of intermediate shields = 1.
 - $\phi_j = 16.1 \times 10^{-3} \text{ W}$
 - $\phi_o = 2.57 \times 10^{-3} + 2.71 \times 10^{-12} (T_r + 9\text{K})^4 \text{ W}$
(Section V)
 - $\epsilon_p = 0.97$ (black paint on honeycomb cavity array)
 - $\epsilon_s = 0.035$ (vacuum deposited aluminum)
 - $\epsilon_i = 0.035$ (gold plate)
 - $A_p = 89.6 \text{ in}^2$; $A_i = 164 \text{ in}^2$
 - $F_{ps} = 0.3948$ (computer calculation, including second reflections)
 - $K_p = 6.220 \times 10^{-4} \text{ WK}^{-1}$; M = 1.17

Figure 3.2-4 Cooler Second Stage Thermal Balance Equation

3.2.4 Optical Port Loading

The geometry of the optical port into the radiant cooler is shown in Fig. 3.2-5. The field lens array (spectrum) at the edge of the patch views the grating through windows on the radiator and cooler housing. To provide contamination protection for the radiator window, it is heated a nominal 9K above the radiator temperature and protected by a cold trap at the radiator temperature (See AVHRR Technical Description, Rev. B., Nov. 25, 1974, DIR No. 15 at the end of Section 6.0). To minimize the radiative load on the patch, the spaces between the field lens are covered with a low-emissivity (gold-plated) surface. In addition, the facing areas of the radiator window that are not utilized by the optical beams from the grating to the field lenses are similarly covered with a low-emissivity surface (e.g., by gold-plated spacers in a segmented window or by a vacuum deposited aluminum film on the window material itself).

The optical loading on the radiator is given by

$$\phi_{or} = \epsilon_1 \sigma T_h^4 A_1 [F_{12}^1 (1 - p_2) + (1 - F_{12}^1)],$$

where ϵ_1 = emissivity of window-spectrometer combination = 0.9

T_h = temperature of cooler housing (spectrometer) = 248K

A_1 = area of housing window = 18.87 cm²

F_{12}^1 = view factor from housing window to radiator window = 0.1

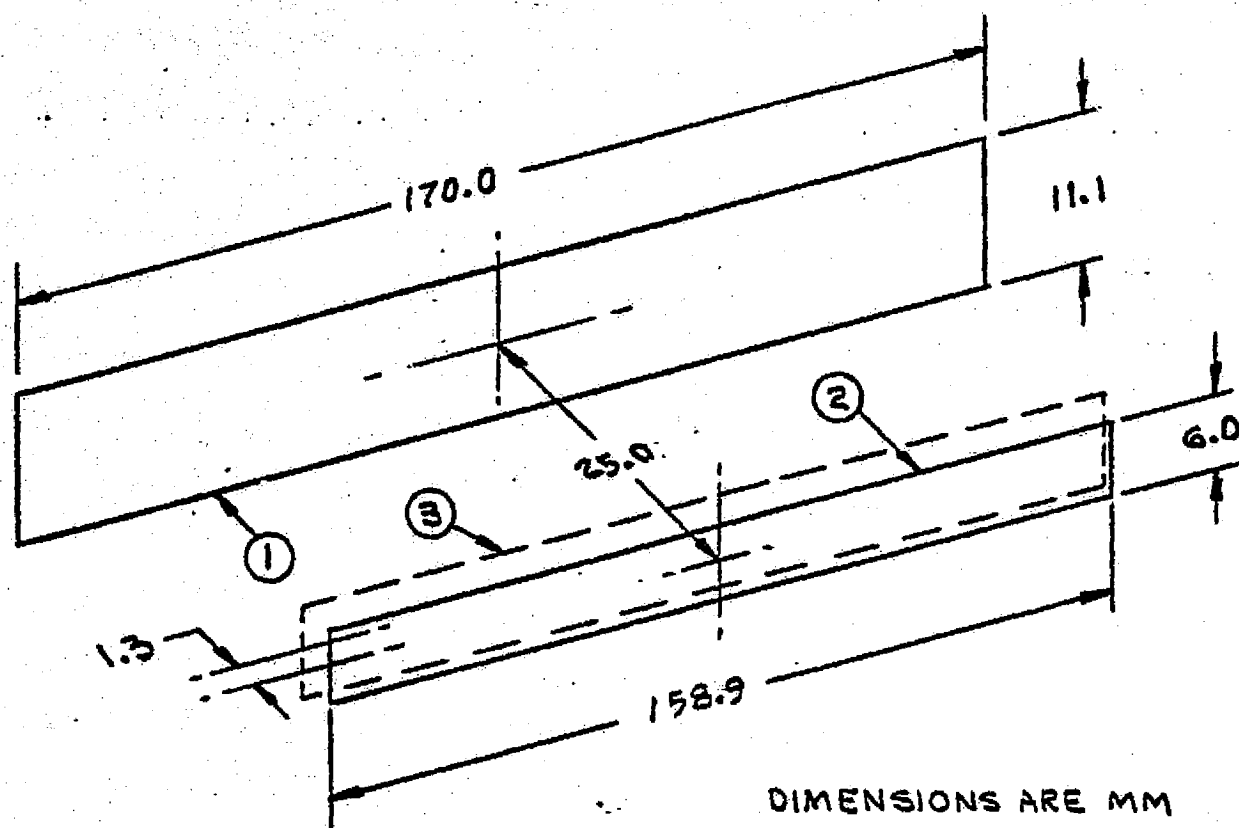
p_2 = fraction of housing temperature radiation passed by radiator window = 0.63 (ZnSe with effective cutoff wavelength of 20 μ m)

We then have

$$\phi_{or} = 0.341W.$$

The optical port loading on the patch consists of inputs from the spectrometer and the radiator. We will restrict the radiator input to that from the inner window itself; radiation at the radiator temperature (i.e., the cold trap) is efficiently absorbed in the window. The input from the instrument to the patch is given by

$$\phi_{13} = \epsilon_1 \sigma T_h^4 p_2 \tau_2 F_{31} \gamma_3 A_3,$$



- ① HOUSING WINDOW (CdTe)
- ② RADIATOR WINDOW (ZnSe)
- ③ PATCH OPENING

FIG. 3.2-5 DIMENSIONS AND OPENING MATERIALS IN OPTICAL PORT

where τ_2 = transmittance of the radiator window for greybody radiation at $T_h = 0.9$

F_{31} = view factor from field lens array to housing window = 0.2035 (computer calculation)

γ_3 = effective absorptivity of the patch opening (field lens array) = $0.65 \times 0.186 = 0.121$

A_3 = area of patch opening = 9.534 cm^2

The width of the patch opening corresponds to the entire spectrum or 158.9 mm. At the same time, this width contains 28 exit slits whose combined openings add up to 29.5 mm, so that $29.5/158.9 = 0.186$ of the patch opening contains germanium. And germanium has broadband effective absorptivity (absorptivity plus transmissivity) of 0.65. As a result, the effective absorptivity γ_3 of the patch opening is 0.65×0.186 . (The radiative interchange between the low-emissivity areas on the patch opening and radiator window are included in the radiative insulation input ϕ_i in the patch thermal balance equation). This gives an input from the housing window of

$$\phi_{13} = 2.57 \times 10^{-3} \text{ W.}$$

The input to the patch from the inner window attached to the radiator is given by

$$\phi_{23} = \sigma T_w^4 \epsilon_2 F_{32} \gamma_3 A_3$$

The window temperature, T_w , is a nominal 9K above the radiator. For an inner window of ZnSe and for greybody radiation at the window temperature, the window emissivity, ϵ_2 , is approximately 0.45 (Y.S. Touloukian and D.P. DeWitt, Thermal Properties of Matter, 1F1/Plenum, 1972) and the effective patch absorptivity is still 0.114. The thermal load on the patch from the radiator window is then

$$\phi_{23} = 2.71 \times 10^{-12} (T_r + 9\text{K})^4 \text{ W}$$

for a view factor F_{32} of 0.92.

3.3 Detector Selection and System Sensitivity

3.3.1 AMTS Requirements

3.3.1.1 System Parameters

System performance is affected by several parameters which are fixed by scientific requirements or by satellite operational characteristics. These include spectral width, dwell time on an elemental field of view, size of the field of view, swath width to be covered, etc.

The instantaneous field of view (IFOV) was specified by J.P.L. as being 45 km. along the spacecraft ground track and < 9 km. perpendicular to the ground track at the subsatellite point. The nominal TIROS spacecraft altitude is 833 km. so that the instrument IFOV along the ground track must be 0.054 radian ($\approx 3.096^\circ$). This is determined by the length (height) of the spectrometer entrance slit (which is imaged on the ground) and the focal length of the telescope lens.

The elemental dwell time is related to the satellite velocity and the instrument effective field of view, which is $45 \text{ km.} \times 45 \text{ km.}$ Since the time for one orbital rotation of the TIROS spacecraft is 102 minutes, the subsatellite ground velocity, V_g , is

$$V_g = \frac{2 \pi R_e}{102 \times 60 \text{ seconds}} = 6.548 \text{ km/second}$$

where R_e = earth's radius = 6,378 km.

For contiguous scan lines, the time for one scan line plus retrace, t_{line} , is

$$t_{\text{line}} = \frac{45 \text{ km}}{6.548 \text{ km/sec}} = 6.872 \text{ seconds.}$$

The retrace time for the HIRS instrument is 0.9 second so we will allow 0.872 seconds for AMTS retrace leaving 6.0 seconds for active scan time. Since the effective FOV is approximately 3° in the scan direction there would be 20 scan elements in a $\pm 30^\circ$ scan. The effective dwell time per element, t_d , is therefore

$$t_d = \frac{6.0 \text{ seconds}}{20 \text{ elements}} = 0.30 \text{ second per element.}$$

The output electrical 3 d.b. bandwidth, Δf_o , is

$$\Delta f_o = \frac{1}{2 t_d} = 1.67 \text{ hz.}$$

The spectral bandwidths are given in Table 1 (section 1.0). Scene radiances are given in the following section.

3.3.1.2 Scene Radiance

The dynamic range of the AMTS instrument is determined by the minimum and maximum scene radiances expected to be encountered in each channel. These are listed in Table 3.3-1. Also given is the scene radiance for a 220 Kelvin source which is used to specify the signal-to-noise requirement. The noise equivalent radiance, NER, for a signal-to-noise ratio of unity is also given in slightly different units.

3.3.1.3 Signal-to-Noise Requirements

The detectors must be selected to meet the system signal-to-noise requirement which was stated by J.P.L. as follows:

"All detectors (must) achieve a minimum signal-to-noise ratio of 100:1 when the field of view is filled with a 220K blackbody for a dwell time consistent with a 45 x 45 km. effective field of view".

3.3.2 Detector Selection

In order to meet the desired performance, detectors with the best sensitivity must be used in all channels and they must be cooled to cryogenic temperatures. In the short wavenumber channels (1-12) mercury-cadmium-telluride (HgCdTe) detectors are the only feasible choice. In order to achieve high sensitivity in the wavenumber bands of interest they must be cooled to the region of 80-90 Kelvin. In the long wavenumber bands (13-28) both lead selenide and indium antimonide detectors are sensitive in the wavenumber bands of interest, however indium antimonide has shown superior performance in the reduced background mode of operation. The InSb detector characteristics will be discussed in Section 3.3.2.1 and the HgCdTe characteristics in Section 3.3.2.2. A preliminary choice (during the study) for the chopping frequency was selected at 250 Hz in order to favor the InSb channels, however, more detailed analysis showed the S/N problem to be more severe in the HgCdTe channels so a higher frequency (500 to 1000 Hz) must be used.

TABLE 3.3-1

EXPECTED TEMPERATURE EXTREMES AND RADIANCES (B)

CH.	ν (cm^{-1})	KELVINS		RADIANCE ($\text{WATTS}/\text{CM}^2 \text{ STR } \text{cm}^{-1}$)			($\frac{\text{Milliwatts}}{\text{m}^2 \text{ str cm}^{-1}}$)
		T_{max}	T_{min}	B_{max}	B_{min}	$B_{220\text{K}}$	N.E.R.
1	607.00	288	216	1.349E-5	4.755E-6	5.125E-6	0.513
2	623.23	276	214	1.164E-5	4.433E-6	4.979E-6	0.498
3	627.75	246	213	7.690E-6	4.305E-6	4.937E-6	0.494
4	635.80	230	212	5.844E-6	4.147E-6	4.862E-6	0.486
5	646.65	228	210	5.537E-6	3.881E-6	4.760E-6	0.476
6	652.75	229	207	5.575E-6	3.584E-6	4.702E-6	0.470
7	666.20	233	209	5.851E-6	3.626E-6	4.572E-6	0.457
8	666.90	233	209	5.844E-6	3.619E-6	4.565E-6	0.456
9	668.10	254	220	8.257E-6	4.554E-6	4.554E-6	0.455
10	669.10	242	213	6.806E-6	3.929E-6	4.544E-6	0.454
11	1203.00	320	216	9.323E-6	6.866E-7	7.943E-7	0.079
12	1231.80	320	216	8.788E-6	6.084E-7	7.063E-7	0.071
13	1772.00	250	216	2.468E-7	4.956E-8	6.142E-8	0.0061
14	1844.50	250	216	1.834E-7	3.448E-8	4.312E-8	0.0043
15	1889.50	250	216	1.521E-7	2.747E-8	3.453E-8	0.0034
16	1809.50	250	216	2.118E-7	4.111E-8	5.118E-8	0.0051
17	1839.40	270	216	4.102E-7	3.538E-8	4.421E-8	0.0044
18	1850.90	280	216	5.591E-7	3.339E-8	4.178E-8	0.0042
19	1930.10	320	216	1.458E-6	2.234E-8	2.822E-8	0.0028
20	2383.75	237	214	8.372E-9	1.767E-9	2.736E-9	0.00027
21	2386.10	257	214	2.555E-8	1.745E-9	2.702E-9	0.00027
22	2388.20	274	215	5.805E-8	1.859E-9	2.673E-9	0.00027
23	2390.20	292	215	1.248E-7	1.839E-9	2.645E-9	0.00026
24	2392.35	306	217	2.124E-7	2.106E-9	2.615E-9	0.00026
25	2394.50	306	217	2.108E-7	2.082E-9	2.585E-9	0.00026
26	2424.00	320	214	3.135E-7	1.418E-9	2.211E-9	0.00022
27	2505.00	320	214	2.403E-7	9.077E-10	1.437E-9	0.00014
28	2616.50	320	214	1.659E-7	4.888E-10	7.897E-10	0.00008

ORIGINAL PAGE IS
OF POOR QUALITY

3.3.2.1 Indium Antimonide Channels (13-28)

To begin with, we will consider the signal and noise currents in Channels 20 through 28, which cover a wavenumber band over which the quantum efficiency of InSb is essentially constant. The noise equivalent current generated in the InSb detector cannot exceed the value given by

$$i_n (\text{max}) = 10^{-2} \eta e (A \Omega) \tau \Delta \nu L_\nu (220K) \alpha^{-1}$$

where η = detector quantum efficiency = 0.85 (Channels 20-28)

e = charge on an electron = $1.602 \times 10^{-19} \text{C}$

$(A \Omega)$ = optical throughput = $2.14 \times 10^{-3} \text{ cm}^2 \text{ ster}$
(Section 3.1.1.1)

τ = optical transmittance = 0.20

$\Delta \nu$ = spectral bandwidth = 2.0 cm^{-1}
(channels 20-25), 2.5 cm^{-1} (channels 26-28)

$L_\nu (220K)$ = spectral photon radiance from a 220K blackbody
at a wavenumber ν (photons $\text{sec}^{-1} \text{ cm}^{-2} \text{ ster}^{-1} / \text{cm}^{-1}$)

α^{-1} = inverse degradation factor = 0.45 (Section 3.3.3.1).

The spectral photon radiance is given by the Planck function,

$$L_\nu (T) = 2 c \nu^2 d\nu / [\exp (ch\nu / kT) - 1]$$

where c = velocity of light = $2.9979 \times 10^{10} \text{ cm sec}^{-1}$
 ch/k = second radiation constant = 1.4388 cm K .

Both the spectral photon radiance and the maximum noise equivalent current are listed in Table 3.3-2 for Channels 20 through 28. In addition, we have listed the noise equivalent radiance (NER) in $\text{mWm}^{-2} \text{ ster}^{-1} / \text{cm}^{-1}$, in order to permit easy comparison with the HIRS specification.

The background current from a blackbody at the temperature T_s of the spectrometer is given by an equation similar to i_n that of the noise equivalent current, namely

$$i_{bg} = \eta e (A\Omega) \tau_c \Delta \nu_c L_\nu (T_s)$$

Table 3.3-2
Spectral Radiance

and

Maximum Noise Equivalent Current
(Channels 25 - 28)

Channel	ν	L_{ν} (220K)	NER	i_n (max)
20	2383.75	5.780×10^{10}	2.737×10^{-4}	3.032×10^{-14}
21	2386.10	5.703	2.703	2.992
22	2388.20	5.635	2.673	2.956
23	2390.20	5.571	2.645	2.922
24	2392.35	5.503	2.615	2.886
25	2394.50	5.436	2.586	2.851
26	2424.00	4.593	2.212	3.012
27	2505.00	2.888	1.437	1.893
28	2616.50	1.520	7.899×10^{-5}	9.96×10^{-15}

ν in cm^{-1}

L_{ν} (220K) in $\text{photons sec}^{-1} \text{ cm}^{-2} \text{ ster}^{-1} / \text{cm}^{-1}$

NER in $\text{mW m}^{-2} \text{ ster}^{-1} / \text{cm}^{-1}$

i_n in amperes

where c = optical elements within the cryogenic cooler

$\tau_c = 0.47$ (first stage window of 0.9; field lens of 0.95,
and spectral filter of 0.55)

$\Delta\nu_c = 25 \text{ cm}^{-1}$ (channel 20-25),

15 cm^{-1} (channel 26-28)

$T_s = 248\text{K}$ (-25°C).

The spectral bandwidths $\Delta\nu$ are those of the cooled spectral filters; they are based on the tolerances of the HIRS filters, as shown in Table 3.3-3. A single filter is used to cover all six of the closely spaced $4.2 \mu\text{m}$ channels (20 - 28) and individual filters to cover each of the well separated window channels (26 - 28). The 248K is a practical (realizable) lower limit for a housing cooled by a horizontal silver teflon radiator (Section 3.5). If lower noise is needed in the $4.2 \mu\text{m}$ band, we can reduce the value of $\Delta\nu$ by increasing the number of filters used, to where we have individual filters for each channel and a minimum bandwidth of 15 cm^{-1} .

The background current results in an rms noise current given by

$$i_n(\text{bg}) = (2e i_{\text{bg}} \Delta f)^{1/2}$$

where Δf = effective noise bandwidth = 1.67Hz.

This value of bandwidth is for the specified scan coverage of $\pm 30^\circ$ from nadir. An increase to the HIRS/2 value of $\pm 49.5^\circ$ would increase it to approximately 2.76 Hz.

The resultant background noise currents are listed in Table 3.3-4 for Channel 20 through 28, together with the maximum allowable current from all other sources. In Channel 28, the background noise current exceeds the maximum allowable value for the total noise current (Table 3.3-2). And in Channel 27 the noise current left for other noise sources is unrealistically low. As a result, we must expect some change in the requirements for these two channels, either in the spectral bandwidths or in the minimum signal/noise ratios.* For example, if the other noise has the maximum allowable value for channel 25, the signal/noise would be reduced to about 80 in channel 27 and 50 in channel 28 (compared with the required value of 100 for a 220K blackbody source).

* Lower signal/noise ratios are acceptable to J.P.L. in Channels 27 and 28.

Table 3.3-3
Spectral Bands
of the
Cooled Filters

Channels 20 - 28

Band to cover 20-28	12.8 cm^{-1}
Tolerance on center ν	8.8
Tolerance on band	<u>3.0</u>
	24.6

Nominal value used 25 cm^{-1}

Channels 26 - 28

Band to cover one channel	2.5 cm^{-1}
Tolerance on center ν	9.4
Tolerance on band	<u>3.0</u>
	14.9

Nominal value used 15 cm^{-1}

Table 3.3-4
Noise Currents
(Channels 20 - 28)

Channel	i_n (bg)	$i_n(0)$ max.
20	2.481×10^{-14} A	1.743×10^{-14} A
21	2.465	1.696
22	2.454	1.648
23	2.442	1.605
24	2.429	1.559
25	2.415	1.515
26	2.244	2.009
27	1.835	0.465
28	1.386	-

i_n (bg) = rms background noise current

$i_n(0)$ = maximum allowable rms noise current
from all other sources

$\Delta f = 1.67$ Hz

If we consider the performance in Channel 25 to be the limiting factor (i.e., assume the requirements in Channels 27 and 28 have been reduced), then according to Section 3.4.1.2 we can set the chopping frequency at a maximum of about 670 Hz. Also we can improve the performance in Channels 20 through 25 by replacing the single 25 cm^{-1} cold filter used for all six channels by a set of six individual 15 cm^{-1} filters for each channel. This reduces i_{bg} in Channel 25 to $1.871 \times 10^{-14} \text{ A}$ and $i_{\text{bg}}(0)_{\text{max}}$ to $2.151 \times 10^{-14} \text{ A}$. Again using the noise currents given in Section 3.4.1.2 we could then increase the chopping frequency to a maximum of 1000 Hz. Or, as an alternate, we could increase the scan coverage from $\pm 30^\circ$ to $\pm 49.5^\circ$ and keep the chopping frequency at 670 Hz or less.

The quantum efficiency of InSb decreases at wavelengths beyond $5.0 \mu\text{m}$; moreover, at these wavelengths it also decreases with a decrease in detector temperature. As a worst case, we have estimated the quantum efficiency in Channels 13 to 19 from the 77K spectral response given by Santa Barbara Research Center (SBRC Brochure 1975, p. 2). The results are listed in Table 3.3-5 for an assumed quantum efficiency of 0.85 at $4.3 \mu\text{m}$.

The only other change from the previous shortwave calculations is the reduction in the signal spectral bandwidth to 1.5 cm^{-1} . The cooled (background) spectral filters are assumed to have a bandwidth of 25 cm^{-1} ; a single filter can be used to cover Channels 17, 14, and 18. The resultant spectral photon radiances for blackbodies at 220K and 248K are also listed in Table 3.3-5. In Table 3.3-6, we show the maximum allowable noise equivalent current (corresponding to a signal/noise of 100 for the 220K source), the background noise current, and the maximum allowable noise current from all other sources. These other sources are the Johnson noise of the detector and the noises of the preamplifier, (Section 3.4.1.2). We see that the allowable levels are much higher than those in Channels 20 to 26; the increase in source radiance with wavelength has more than offset the decrease in quantum efficiency. In fact, if the other sources contribute a level of $1 \times 10^{-14} \text{ A}$, we could meet the sensitivity requirement with a quantum efficiency as low as 0.0270 in Channel 13 and 0.0337 in Channel 16.

Table 3.3-5
 Detector Quantum Efficiency
 and
 Source Photon Radiance
 (Channels 13-19)

Channel	ν	η	L_{ν} (220K)	L_{ν} (248K)
13	1772.00	0.13	1.745×10^{12}	6.458×10^{12}
16	1809.50	0.15	1.424	5.417
17	1839.40	0.34	1.210	4.706
14	1844.50		1.177	4.595
18	1850.90		1.137	4.458
15	1889.50	0.57	9.202×10^{11}	3.714
19	1930.10	0.70	7.363	3.062

ν in cm^{-1}

L_{ν} (T) in photons $\text{cm}^{-2} \text{ster}^{-1}/\text{cm}^{-1}$

Table 3.3-6
Noise Currents
(Channels 13-19)

Channel	i_n (max)	i_n (bg)	i_n (0) max
13	$1.05 \times 10^{-13} \text{ A}$	$4.25 \times 10^{-14} \text{ A}$	$9.60 \times 10^{-14} \text{ A}$
16	0.99	4.19	8.97
17	1.90	5.87	18.1
14	1.85	5.80	17.6
18	1.78	5.71	16.9
15	2.43	6.75	23.3
19	2.39	6.80	22.9

$$\Delta f = 1.67 \text{ Hz}$$

3.3.2.2

HgCdTe Channels

Figure 3.3-1 shows the variation in theoretical detectivity, D^*_λ , with temperature at both $15\mu\text{m}$ (667 cm^{-1}) and $16.5\mu\text{m}$ (606 cm^{-1}). These curves assume that the chopping frequency is high enough that no $1/f$ noise is present and that the responsivity is high enough (and that bias current is adequate) so that preamplifier noise is negligible. At these wavelengths the HgCdTe detectors are thermal G-R noise limited so that cooling or spectrally restricting the background irradiance on the detector does not improve the D^*_λ .

Figure 3.3-2 shows the theoretical variation of responsivity with temperature for the same two wavelengths. This data, as well as the D^*_λ data, was obtained from Honeywell Radiation Center, Lexington, Mass. The variation of responsivity with temperature is much greater than the variation of D^*_λ ; by going from 90K to 84K the responsivity permits use of a smaller bias current to operate the detector which permits a lower bias heat input to the radiant cooler. It should also be noted that the high responsivity is obtained by dividing the sensitive area into three strips which are electrically connected in series. Also, it was later found possible to reduce the size of the detector from $1.0\text{ m.m.} \times 1.0\text{ m.m.}$ to about $0.84\text{ m.m.} \times 0.84\text{ m.m.}$, depending on the f-number of the field lenses; this also tends to increase the responsivity and reduce the detector bias heat load to the cooler. At 84 kelvins, an estimated minimum responsivity of 650 volts per watt can be achieved for the $623\text{--}669\text{ cm}^{-1}$ channels (2 to 10) using 1 m.w. of bias power per detector whereas at 607 cm^{-1} (channel 1) a bias power of 4 m.w. has been allotted in the cooler design because of the greater importance in achieving the highest possible signal-to-noise ratio and because of less experience by detector manufacturers at the shorter wavenumbers.

At 667 cm^{-1} ($15\mu\text{m}$) one detector manufacturer (HRC) will guarantee delivery of a $1\text{ m.m.} \times 1\text{ m.m.}$ detector with a D^*_λ of $1.0 \times 10^{10}\text{ cm Hz}^{1/2}\text{ watt}^{-1}$ at an operating temperature of 90 kelvins, chopping frequency of 250 Hz and bias power of 4.0 m.w.; at 1,000 Hz they will guarantee a D^*_λ of $1.2 \times 10^{10}\text{ cm Hz}^{1/2}\text{ watt}^{-1}$. Cooling to 84K instead of 90K gives a theoretical improvement of 1.25. Since 1,000 Hz is a rather high chopping frequency for the InSb detectors, (due to a capacitance noise effect in the preamplifier) we expect a better choice would be near 500 Hz. For our signal-to-noise calculations we therefore estimate the D^*_λ at 667 cm^{-1} to be $1.36 \times 10^{10}\text{ cm Hz}^{1/2}\text{ watt}^{-1}$ or better for operation at 84 kelvins and for a chopping frequency near 500 Hz. At 607 cm^{-1} we estimate a D^*_λ of $1.19 \times 10^{10}\text{ cm Hz}^{1/2}\text{ watt}^{-1}$ to be achievable based on the theoretical D^*_λ data (HRC is very reluctant to guarantee such performance, however, due to lack of experience at these wavenumbers and operating temperature). The D^*_λ values for the other channels were obtained by linear scaling between these two extremes and are listed on page 75.

Fig. 3.3-1 THEORETICAL D_{λ}^* VERSUS T FOR $HgCdTe$

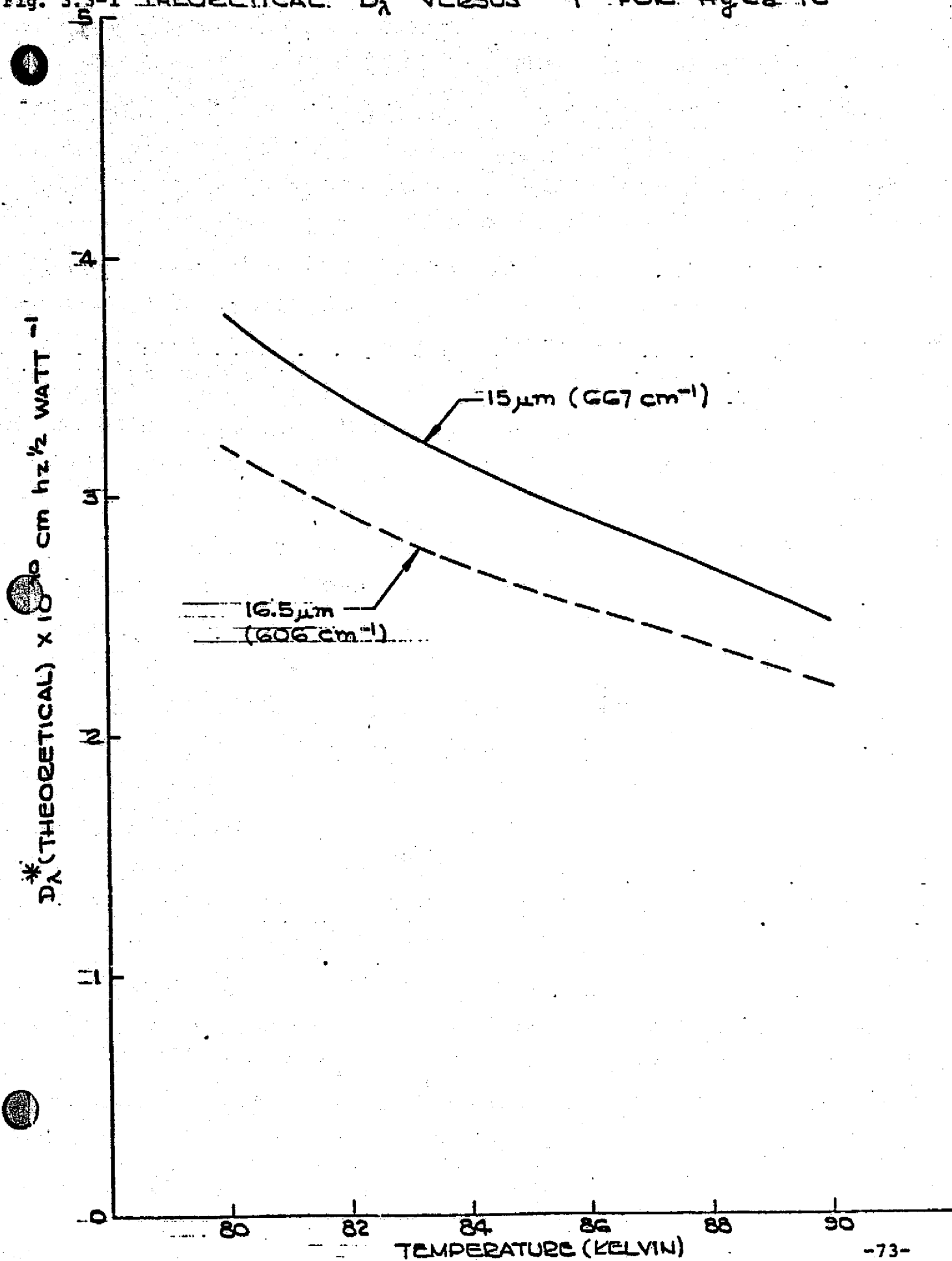
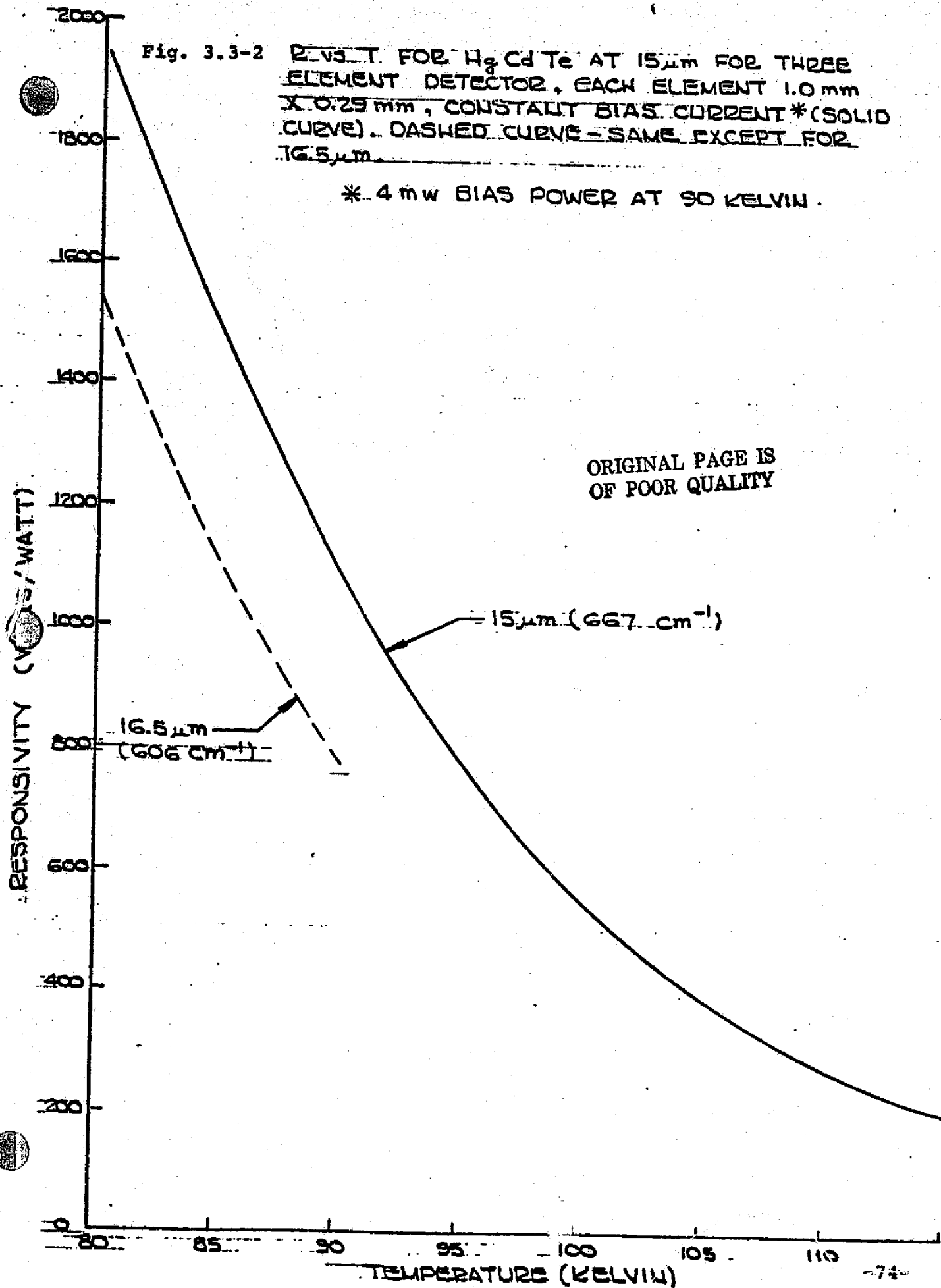


Fig. 3.3-2 R vs T FOR $HgCdTe$ AT $15\mu m$ FOR THREE ELEMENT DETECTOR, EACH ELEMENT $1.0 mm \times 0.29 mm$, CONSTANT BIAS CURRENT* (SOLID CURVE). DASHED CURVE - SAME EXCEPT FOR $16.5\mu m$.

* $4 mW$ BIAS POWER AT 90 KELVIN.

RESPONSIVITY ($V/WATT$)

ORIGINAL PAGE IS
OF POOR QUALITY



<u>Channel</u>	<u>Wavenumber</u>	<u>D_v[*] (minimum expected)</u>
1	607 cm ⁻¹	1.19 x 10 ¹⁰ cm Hz ^{1/2} watt ⁻¹
2	623 cm ⁻¹	1.24 x 10 ¹⁰ cm Hz ^{1/2} watt ⁻¹
3	628 cm ⁻¹	1.25 x 10 ¹⁰ cm Hz ^{1/2} watt ⁻¹
4	636 cm ⁻¹	1.28 x 10 ¹⁰ cm Hz ^{1/2} watt ⁻¹
5	647 cm ⁻¹	1.31 x 10 ¹⁰ cm Hz ^{1/2} watt ⁻¹
6	653 cm ⁻¹	1.32 x 10 ¹⁰ cm Hz ^{1/2} watt ⁻¹
7-10	666-669 cm ⁻¹	1.36 x 10 ¹⁰ cm Hz ^{1/2} watt ⁻¹

For channels 11 and 12, (near 8μm or 1200 cm⁻¹) the detectivity of HgCdTe is background limited. Thus cooling the background, restricting the spectral band and/or limiting the field of view at the detector all tend to improve the D_λ^{*}. Experience on AVHRR and other programs has shown that detectors with D_λ^{*} near the BLIP limit can be purchased at a reasonable cost. A detector with D_λ^{*} (295 kelvin background, 2 π FOV, 1K Hz) at 8μm of 2 x 10¹⁰ λ cm Hz^{1/2} watt⁻¹ can be readily obtained. The field of view at the detector can be obtained from the AMTS throughput value, AΩ, which is equal to 2.14 x 10⁻³ cm² str. For a square detector edge width of 0.084 cm we find Ω = 0.32 str. Using Ω = π sin² θ to get the equivalent circular FOV yields sin θ = 0.31 and D_λ^{*} (295 K bkgnd, 18° FOV, 1K Hz) = 2 x 10¹⁰

$$\begin{aligned} & \sin \theta \\ & = 6.4 \times 10^{10} \text{ cm Hz}^{1/2} \text{ watt}^{-1}. \end{aligned}$$

Since the spectrometer will be cooled to 248K to reduce the background irradiance on the InSb detector, we will get some improvement also in the 8μm HgCdTe detectors. This will be offset at least in part by the lower chopping frequency and a small bias power (~ 1 m.w.); we will use a detectivity for signal-to-noise calculations of

$$D_{\lambda}^* (8\mu\text{m}, 18^{\circ} \text{ FOV Hz}, 248\text{K bkgnd}) = 5 \times 10^{10} \text{ cm Hz}^{1/2} \text{ watt}^{-1}.$$

If necessary, the detectivity could be further enhanced by use of a cooled narrow spectral band filter in front of the detector.

3.3.3 System Sensitivity

3.3.3.1 Degradation Factors

Radiometric instruments frequently use choppers to modulate the incoming signal. This is done to avoid low-frequency noise in the detector and amplifier and to allow the use of stable, a-c amplification. The signal is then demodulated and filtered to provide the output (Ref. 1). In a synchronous or coherent demodulator, the target signal is beat with an inphase reference signal of the same frequency. In this section, we will first discuss degradation factors which apply to signal processing. Next we will treat degradation effects as they apply to detector and amplifier noise in the HgCdTe channels; noise effects in the InSb channels are treated in section 3.3.2.1.

For a sinusoidal input signal, the output signal-to-noise ratio from a synchronous demodulator is independent of the demodulation waveform. For example, A. van der Ziel (Ref. 2), shows that square-wave (commutator or switching) coherent demodulation is equivalent to sine-wave (mixing) coherent demodulation with the fundamental of the square wave. And in general, the synchronous demodulation of a sinusoid by any waveform is equivalent to sinusoidal demodulation using the fundamental of the demodulation waveform. For a non-sinusoidal target signal, the optimum demodulator has the same waveform as the target signal. Thus synchronous demodulation may be viewed as a problem in cross-correlation.

The advantages of modulation and demodulation, however, are not obtained without compensation. The process introduces a reduction in the signal to noise ratio, which may be expressed as a degradation factor. Inverse degradation factors, or the values by which the signal to noise ratio is reduced, are listed in Table 3.3-7 for modulated radiant signals in the form of sine, triangle, and square waves (Refs. 3, 4 and 5). Reference 3 also contains formulas for trapezoidal waveforms, of which the triangle and square are limiting cases.

REFERENCES

1. R. A. Smith, F. E. Jones, and R. P. Chasmar, The Detection and Measurement of Infrared Radiation, Oxford at the Clarendon Press, 1957, Sections 6.6-6.8, Chapter XII.
2. A. Van der Ziel, Noise, Prentice-Hall, 1954, Chapter 13.
3. Report on the Design Review for the High Resolution Infrared Radiation Sounder, ITT Aerospace/Optical Division for Goddard Space Flight Center, Contract NAS5-21651, March 1972; Sections 2.3.3 and 2.3.4.
4. R. V. Annable, The Synchronous Demodulation of a Square Wave, ITT Aerospace/Optical Div. internal memorandum, Oct. 29, 1970.
5. R. Hanel, Chapter 13 in Advances in Geophysics, ed, by A. J. Drummond, Academic Press, 1970.

Table 3.3-7

Inverse Degradation Factors
for
Modulation and Demodulation

<u>Waveform</u>	<u>Square-wave demodulation</u>		<u>Optimum demodulation</u>
	<u>Fundamental</u>	<u>All harmonics</u>	<u>All harmonics</u>
Sine	$\frac{1}{2\sqrt{2}} = 0.3536$	--	--
Triangle	$\frac{4}{\pi^2\sqrt{2}} = 0.2866$	$\frac{1}{4} = 0.2500$	$\frac{1}{2\sqrt{3}} = 0.2887$
Square	$\frac{2}{\pi\sqrt{2}} = 0.4502$	$\frac{1}{2} = 0.5000$	$\frac{1}{2} = 0.5000$

When only the fundamental of the signal waveform is used, synchronous demodulation may be interpreted as a process by which the fundamental is converted from peak-to-peak into rms. The conversion factor is then just the reciprocal degradation factor given in Table 3.3-7. The same interpretation can be used when a optimum demodulation waveform, identical to that of the complete signal waveform from the chopper, is used to demodulate all the harmonics (in this case, the conversion factor applies to the complete signal with all harmonics). Such a simple interpretation does not appear to be possible, in general, when all signal harmonics are used in a square wave demodulation.

The lowest degradation factor is achieved by a square wave demodulation of all the harmonics in a square wave signal. Two practical limitations, however, prevent us from achieving this ideal, although it can be closely approached. First, the electrical input bandwidth is finite and cannot pass all the harmonics. And second, square wave modulation cannot be obtained with a non-zero, finite chopper and aperture. Thus we are, in practice, dealing with a trapezoid wave whose shape is determined by the ratio (m) of chopper to aperture dimensions. As an example, assume that m is 10 and that the first 4 harmonics (1st, 3rd, 5th and 7th) are used in a square wave demodulation. Using the equations given in Ref. 3, we find that the resultant inverse degradation factor is 0.4806 or 96.1% of the ideal value of 0.5.

In the case of a trapezoidal signal, there is an optimum number of harmonics that is a function of the ratio m . For example, when $2.347 > m > 4.015$, only harmonics 1 through 5 should be used (Ref. 3). For m equals 10, the optimum number of harmonics is through the 11th, which yields an inverse degradation factor of 0.4819 or 96.4% of the ideal.

Finally, we should point out that the above results are for a uniform scene that fills the aperture at which the chopping takes place. However, the output signal will, in general, depend on the power distribution within the aperture as well as on the power magnitude. If this adversely influences the operation of the sounder, we can use the waveform independent technique for synchronous demodulation described by Geist (Ref. 6). This requires that both the infrared detector and the signal processing electronics that precede the synchronous demodulator introduce no frequency dependent phase shift or attenuation, i.e., pass all signal harmonics or a sufficiently high number of them without distortion. Moreover, the inverse degradation factor is reduced to 0.25.

Reference

6. J. Geist, Waveform-Independent Lock-In Detection, Rev. Sci. Instr. 43, 1704 (1972).

Next we will derive a noise degradation factor for the HgCdTe detector channels. We define this degradation factor, α_n , as follows:

$$\alpha_n = \sqrt{\frac{N_p^2 + N_d^2}{N_d^2}} = \sqrt{\frac{N_p^2}{N_d^2} + 1}$$

where N_p = noise voltage of the preamplifier referred to its input

N_d = noise voltage from the HgCdTe detector.

Now N_d is given by

$$N_d = R \cdot NEP_d = R \frac{\sqrt{A_d \Delta f}}{D^*}$$

where R = responsivity of the detector (volts per watt)

A_d = detector area (0.084 cm X 0.084 cm)

Δf = output 3 d.b. electrical bandwidth

D^* = detector detectivity.

There is some variation of R and D^* between channels, however, since α_n is small we will only consider the difference between channel 1 and the rest (2-12). Combining the above equation gives

$$\alpha_n = \sqrt{\frac{N_p^2 D^{*2}}{R^2 A_d \Delta f} + 1}$$

From section 3.4.1.1 we have

$$N_p = 2 \times 10^{-9} \text{ volt}$$

and from section 3.3.2.2

$$D^* \text{ (chs. 2-10)} \doteq 1.3 \times 10^{10} \text{ cm Hz}^{1/2} \text{ watt}^{-1}$$

$$R \text{ (chs. 2-10)} \doteq 650 \text{ volts watt}^{-1}$$

$$A_d = 0.084 \text{ cm} \times 0.084 \text{ cm}$$

$$\Delta f = 1.67 \text{ Hz}^{1/2}$$

which gives

$$N_d = 5.42 \times 10^{-9} \text{ volt and}$$

$$\alpha_n = 1.066 \text{ (chs. 2-10)}$$

In channel 1 ($\nu = 607 \text{ cm}^{-1}$) we have

$$D^* (\text{ch. 1}) = 1.19 \times 10^{10} \text{ cm Hz}^{1/2} \text{ watt}^{-1}$$

$$R (\text{ch. 1}) \doteq 500 \text{ volts watt}^{-1}$$

$$\text{giving } \alpha_n = 1.092.$$

Combining with the signal degradation factor, α_s , for a square wave demodulation and using the fundamental component of a square wave ($\alpha_s = 1/0.4502 = 2.221$)

$$\alpha_s \alpha_n = \begin{cases} 2.42 & \text{in channel 1} \\ 2.37 & \text{in channels 2-12.} \end{cases}$$

These degradation factors will be used in the following sections to calculate the expected AMTS signal-to-noise ratios.

3.3.3.2 Signal/Noise in Channels 13-28

In section 3.3.2.1 we determined the signal currents from the InSb detector for a $S/N = 1$ with a 220 kelvins scene filling the instrument field of view. From Table 3.3-6 and from Section 3.3.2.1 the signal currents in channels 13 to 18 are given by

$$S = 100 \times i_n (\text{max}).$$

The noise current from the detector, which is predominantly background generated noise, was also calculated in section 3.3.2.1. To get the total noise we must combine the background noise current, $i_n (\text{bg})$, with the noise from the pre-amplifier, $i_n (\text{p})$, which is given in section 3.4.1.2.3. The signal/noise ratio is given by

$$\frac{S}{N} = 100 \times \frac{i_n (\text{max})}{[i_n (\text{bg})^2 + i_n (\text{p})^2]^{1/2}}$$

The resultant signal/noise ratios are given in Table 3.3-8 for a 500 hz chopping frequency for two different swath widths. With a 500 hz chopping frequency and 25 cm^{-1} filter in channels 20 to 25, we are limited to the $\pm 30^\circ$ swath width; other possibilities were discussed in section 3.3.2.1.

3.3.3.3 Signal-to-Noise Ratio in Channels 1 - 12.

The radiant power incident on the detector that produces a signal from the detector equal to the noise is termed the noise equivalent power or NEP. It is given by

$$\text{NEP} = \frac{(A_d)^{1/2} (\Delta f)^{1/2} a_N}{D^*_{\nu}}$$

ν = wavenumber (cm^{-1}) of channel

A_d = detector sensitive area

Δf = electronic information or output bandwidth

D^*_{ν} = detector specific detectivity at the wavenumber of the specified channel and at the radiant signal chopping frequency

a_N = noise degradation factor.

The radiant power, S , incident on the detector from a 220K blackbody scene of spectral radiance $L(220K, \nu)$ ($\text{watts/cm}^2 \text{ ster cm}^{-1}$) in the specified channel is given by

$$S = A_o \Omega_o a_s^{-1} \int L(220K, \nu) \tau(\nu) d\nu$$

where

A_o = area of entrance pupil

Ω_o = solid angle of view of instrument

$\tau(\nu)$ = instrument transmittance at ν

a_s = signal degradation factor.

Because of the narrow bands (high spectral resolution), we can replace the integral with the product

$$\tau_{\nu} L_{\nu}(220K) \Delta\nu$$

where τ_v and L_v are the values at the center wavenumber and Δv is an effective band given by

$$\Delta v = \frac{1}{\tau_v} \int \tau(v) dv$$

The signal-to-noise ratio is given by

$$\frac{S}{N} = \frac{A_o \Omega_o \tau_v \Delta v L_v (220K) D_v^*}{\alpha_n \alpha_s A_d^2 \Delta f^2}$$

We can relate the electronic output bandwidth to the integration time t_o of a channel. For example, the electronic output filter may be an ideal, low-pass filter, also known as a running-mean filter or a zero-order hold filter (See B.F.C. Cooper, Post-Detector Filtering in Radiometry, Proc. Inst. of Radio & Electron. Engrs. Australia, 31, No. 2, pp. 41-48, Feb. 1970). Its normalized frequency response is $\sin \pi t_o f / \pi t_o f$, where f is the electrical frequency. For white noise, the equivalent output bandwidth is given by

$$\Delta f = \int_0^\infty (\sin \pi t_o f / \pi t_o f)^2 df = \frac{1}{2t_o}$$

In the case of the Advanced Meteorological Temperature Sounder, t_o may be identified with the dwell time consistent with a 45 km x 45 km effective field of view. From Section 3.3.1.1 we have $\Delta f = 1.67$ Hz.

Returning to the S/N equation, we see that, except for a scale factor, all of the parameters are either specified in the functional requirements or set by the requirements in other areas. Of course, the other areas may in turn be influenced, in turn, by the requirement for a minimum S/N ratio of 100:1 in all channels. In particular, $L_v (220K)$, Δv and $t_o (\Delta f)$ are specified directly or indirectly in the functional requirements. The convergence angle u at the detector, which is determined by the Abbe sine law $A_d \pi \sin^2 u = A_o \Omega_o$, comes from the optical design. From the standpoint of S/N, it is the objective of the optical design to maximize this angle (minimize the f-number) subject to the constraints imposed by other instrument requirements. The transmittance τ_v can also be obtained from the optical design. Again from the S/N standpoint, it is the objective of the detector selection task to obtain the maximum D_v^* , consistent with the requirement for a realizable cooling system. The signal degradation factor depends on the signal processing system (modulation, demodulation, and filtering) and the performance of the preamplifiers; it is therefore an input from the electronic design (Section 3.4).

This leaves us with the detector area, which represents the scale factor or size of the instrument's optical assembly. That is, when all the other factors have been set, the system performance requirements impose a minimum size requirement. A lower size limit may also be imposed by spatial or spectral diffraction effects. At the same time, there will be upper limits imposed by size and mass restrictions on the smaller size end by the smallest size field lens width that is feasible from a manufacturing/use standpoint. Contacts with two optical fabricators indicated that lenses could be made as small as $\frac{1}{4}$ m.m. wide, however, optical performance may not be good due to twisting caused by internal stresses (also because of cooling to 84 kelvin). A more feasible width was considered to be ≈ 1.0 m.m. minimum and the final optical design achieved this size.

From section 3.1.1 we have

$$A_o \Omega_o = 2.14 \times 10^{-3} \text{ cm}^2 \text{ str for all channels.}$$

$$A_d^{\frac{1}{4}} = 0.0842 \text{ cm}$$

From the AMTS specification we have

$$\Delta v = \begin{cases} 0.5 \text{ cm}^{-1} & \text{in channels 1 - 10} \\ 1.0 \text{ cm}^{-1} & \text{in channels 11 and 12.} \end{cases}$$

The optical transmission is estimated as follows

$$\tau_v = R_m^2 \tau_{fl} \tau_{tl} \tau_w^2 \epsilon_{gv}$$

where R_m = mirror reflectance (including grating)

τ_{fl} = transmittance of field lens

τ_{tl} = transmittance of telescope lens

τ_w = transmittance of cooler window

ϵ_{gv} = grating efficiency at v .

We will ignore variations in mirror reflectance and lens transmittance with wavenumber since these are comparatively small but grating efficiency data was obtained from Bausch and Lomb for our spectrograph mode (not the normally published Littrow configuration data). Since the field lenses can be coated for optimum narrow band performance we estimate higher transmission than for the telescope lens and cooler windows which must have wide band coatings.

Using

$$\tau_m = 0.98$$

$$\tau_{f1} = 0.95$$

$$\tau_{t1} = \tau_w = 0.90$$

yields $\tau_v = 0.589 \approx \tau_{gv}$ (see Table 3.3.3-1)

Using the data for D_v^* from section 3.3.2.2, scene radiance for a 220K source and degradation factors from section 3.3.3.1 the signal-to-noise ratios for channels 1 - 12 were calculated and are given in Table 3.3.3-1. Channels 11 to 12 have adequate margin or safety over the required S/N ratio of 100:1. Channels 6 to 10 also have relatively safe margins since D_v^* values used in the calculations are near the spectral region (667 cm^{-1} or $15 \mu\text{m}$) where HgCdTe suppliers have had some past experience and the values used were based on one vendor's guaranteed performance. Signal-to-noise in channel 1 barely meets the desired performance using the estimated minimum D_v^* (see section 3.3.2.2). The grating efficiency of 69% at 607 cm^{-1} (channel 1) seems low since the grating parameters (80 grooves/m.m. and blaze wavelength of $16.4 \mu\text{m}$ in Littrow configuration) were chosen to optimize efficiency in this region. Every effort must be made to improve the sensitivity at 607 cm^{-1} , the most critical being the achievable D_v^* which can be obtained from detector manufacturers.

TABLE 3.3.3-1 SIGNAL-TO-NOISE RATIO FOR CHANNELS 1 - 12

Channel	ν (cm ⁻¹)	ϵ_{gv}	L_{ν} (220K)**	$D^* \frac{\text{cm Hz}^{\frac{1}{2}}}{\text{watt}}$	$\alpha_s \cdot \alpha_n$	S/N
1	607.00	0.69	5.12×10^{-6}	1.19×10^{10}	2.42	101
2	623.23	0.71	4.98×10^{-6}	1.24×10^{10}	2.37	107
3	627.75	0.71	4.94×10^{-6}	1.25×10^{10}	2.37	107
4	635.80	0.71	4.86×10^{-6}	1.28×10^{10}	2.37	108
5	646.65	0.72	4.76×10^{-6}	1.31×10^{10}	2.37	110
6	652.75	0.73	4.70×10^{-6}	1.32×10^{10}	2.37	111
7	666.20	0.74	4.57×10^{-6}	1.36×10^{10}	2.37	113
8	666.90	0.74	4.56×10^{-6}	1.36×10^{10}	2.37	112
9	668.10	0.74	4.55×10^{-6}	1.36×10^{10}	2.37	112
10	669.10	0.74	4.54×10^{-6}	1.36×10^{10}	2.37	112
11	1203.00	0.75	7.94×10^{-7}	5.0×10^{10}	2.37	144
12	1231.80	0.78	7.06×10^{-7}	5.0×10^{10}	2.37	133

** in units of watts/cm² str cm⁻¹

3.4 Electronics Design

3.4.1.0 ELECTRICAL BLOCK DIAGRAM

The block diagram for the total sounder system is shown in Figure 3.4-1. Each of the 28 channels has an individual video amplifier chain which consists of a preamplifier, main amplifier, filter, and a synchronous demodulator followed by an integrator and holding circuit. The outputs from the 28 channels are fed into an analog multiplexer where they are sequentially routed to an analog to digital converter for conversion into a 14 bit digital word before being sent to the spacecraft data system.

Channels 1 through 12 use low input impedance preamplifiers which are fed by HgCdTe detectors while channels 13 through 28 make use of InSb detectors which feed preamplifiers with cooled FET input stages to obtain low noise operation.

A chopper in the optical path chops the incoming energy at a 250*Hz rate. A pickup from the chopper is used to generate the reference signal that is used by the synchronous demodulators. All 28 channels are sampled simultaneously so that the data from each spectral channel is taken from the same IFOV.

The requirements for the A/D Converter are set by the dynamic range of the scene and the signal to noise ratio desired. The most severe requirements occur in channels 25, 26, 27 and 28. If the allowable noise level at a S/N ratio of 100:1 is assigned a value of one bit, the resulting levels of digitization required for these channels are listed below.

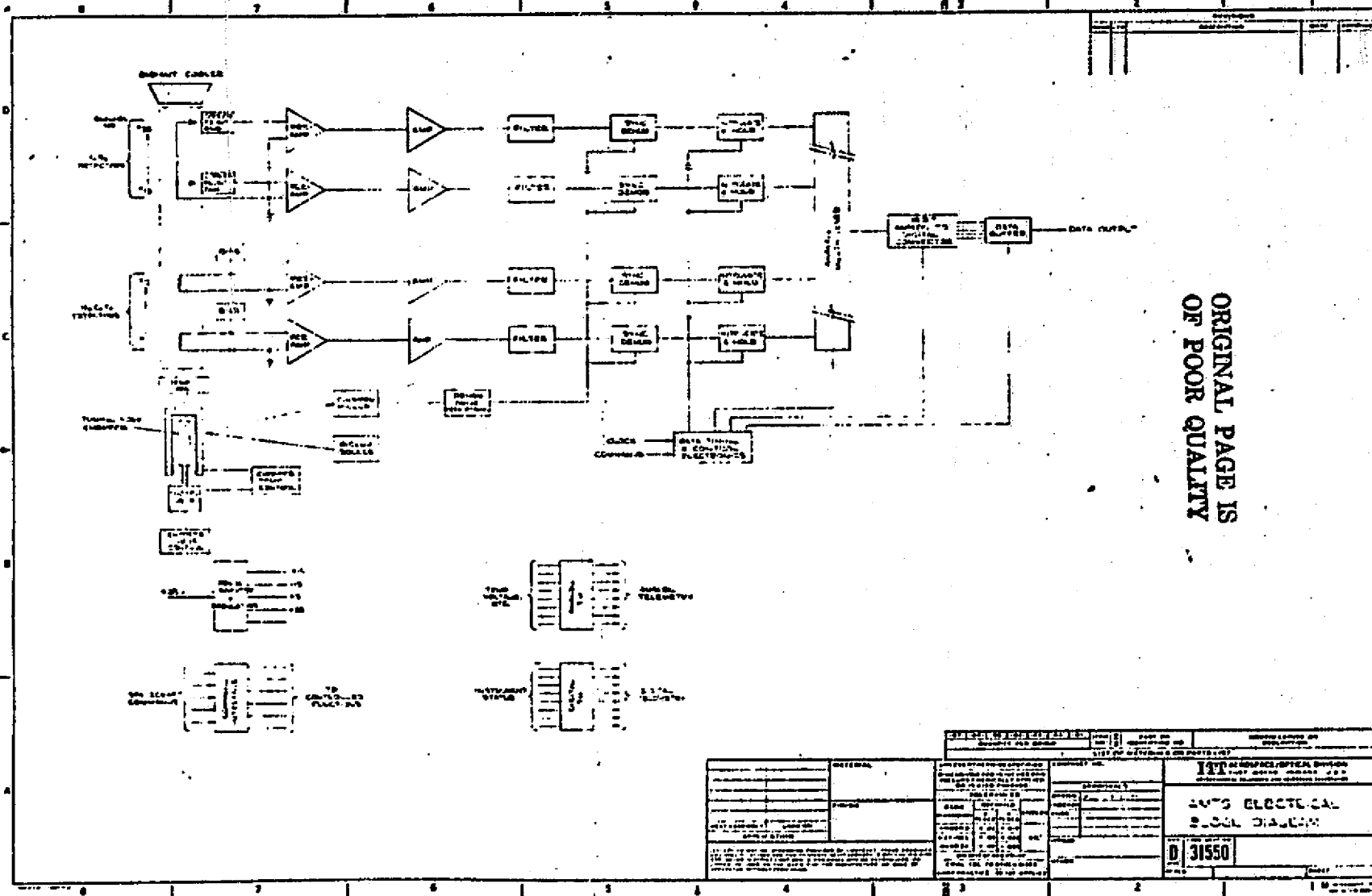
<u>Channel</u>	<u>Bits</u>
25	11,033
26	18,118
27	15,868
28	37,912

Since it is unlikely that a S/N ratio of 100:1 will be obtained in Channel 28 and also because of the fact that channel 26 may not be used over its full dynamic range, a 14 bit A/D converter will be used which will provide 16,384 quantizing intervals.

3.4.1.1 Mercury-Cadmium - Telluride Channels

The preamplifiers for the Mercury-Cadmium-Telluride (HgCdTe) channels, 1 through 12, are designed for use with a low impedance source and therefore do not require FET's to provide a high input impedance. The low input impedance reduces the susceptibility to noise pickup and the effects of stray capacity upon the operation. Since a low noise preamp for these channels can be obtained without cooling any of the preamp components and the low impedance detector reduces the need for short lead lengths,

* Preliminary study value; revised to 500 - 1000 Hz.



ORIGINAL PAGE IS
OF POOR QUALITY

Fig. 3.4-1 AMTS Electrical Block Diagram

there is no need to place any of the components on the first stage of the radiant cooler. This helps to reduce the number of leads going into the cooler.

Figure 3.4-2 shows the schematic diagram of the preamp to be used for the HgCdTe channels. Figure 3.4-3 illustrates the typical noise performance which can be expected from this amplifier.

The bias current supply for the detectors is also shown with the schematic of the preamplifier. A constant current supply is used to obtain a high impedance to minimize loading the signal from the detector. This is advantageous because of the significant internal resistance of the HgCdTe detectors.

The major factors entering into the noise of this preamp are detector resistance Johnson noise, input transistor noise and the noise caused by the bias current supply. Previous tests with the bias current supply indicate that it generates approximately 1×10^{-12} amps/ $\sqrt{\text{Hz}}$ of noise per milliampere of bias current. Channel 1 is operated with 4 milliwatts of bias power while channels 2 through 12 are operated with 1 milliwatt of bias power. This results in bias currents of 3.9 ma and 1.9 ma respectively. For a 3.9 ma detector bias and a 270 ohm detector, this results in

$$e_B = (3.9 \times 10^{-12}) \cdot (270)$$

$$e_B = 1.05 \times 10^{-9} \text{ V}/\sqrt{\text{Hz}}$$

The 1.9 ma bias results in a noise of

$$e_B = (1.9 \times 10^{-12}) \cdot (270)$$

$$e_B = 0.52 \times 10^{-9} \text{ V}/\sqrt{\text{Hz}}$$

The detector Johnson noise (84°K) is

$$e_D = \sqrt{4KTBR}$$

$$e_D = [(4) \cdot (1.38 \times 10^{-23}) \cdot (84) \cdot (270)]^{1/2}$$

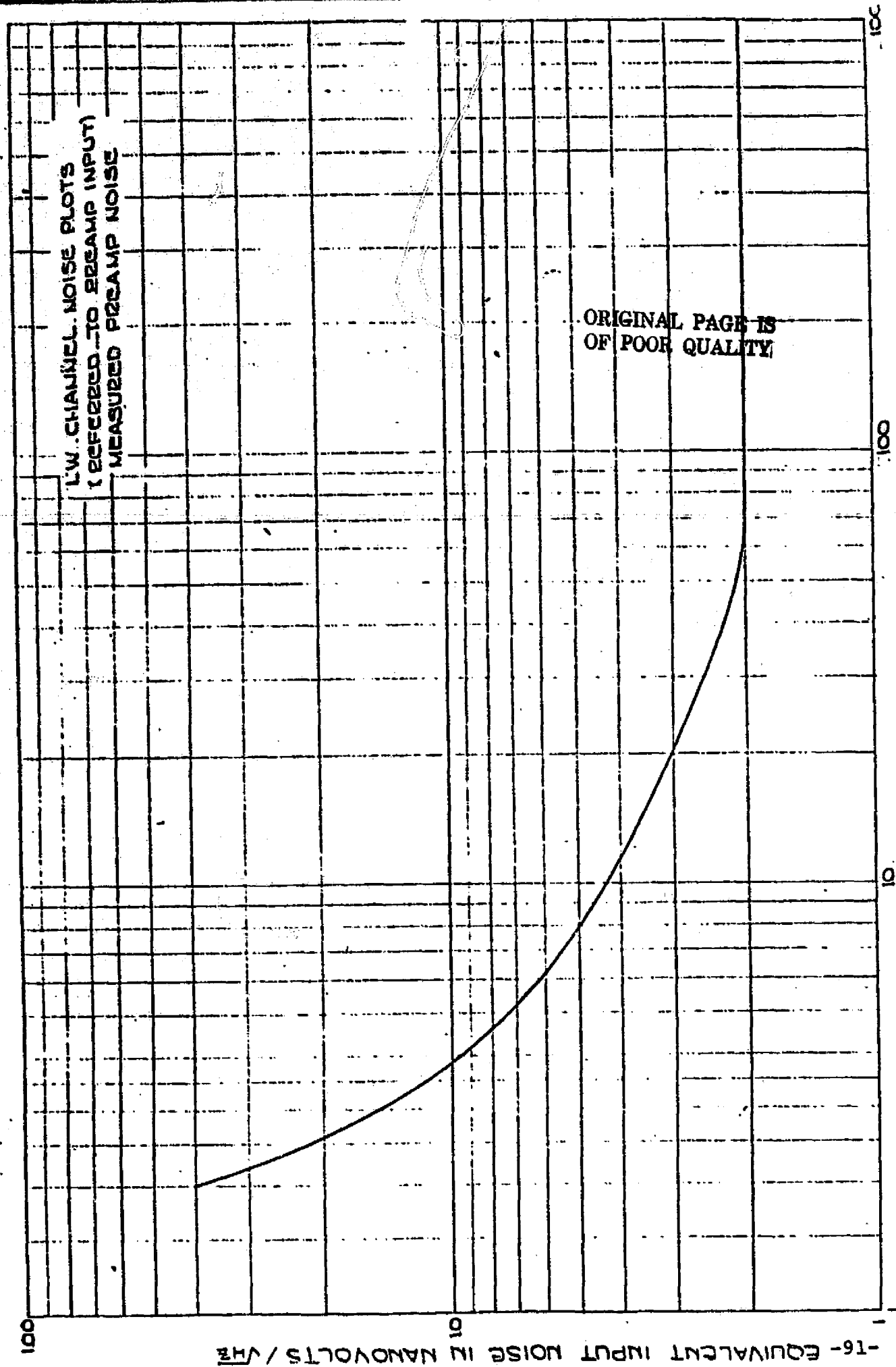
$$e_D = 1.12 \times 10^{-9} \text{ V}/\sqrt{\text{Hz}}$$

The transistor noise is made up of the emitter-base voltage noise and the base current noise.

The emitter-base noise can be described by

$$e_n = KT \frac{2}{q I_C}$$

$$e_n = 0.293 \times 10^{-9} \text{ V}/\sqrt{\text{Hz}} \text{ for } I_C = 2.5 \text{ ma.}$$



ORIGINAL PAGE IS
OF POOR QUALITY

Fig. 3.4-3 Plot of HgCdTe Preamp Noise

The base current noise is

$$i_n = \frac{2q I_c}{h_{fe}}$$

$$i_n = 1.266 \times 10^{-12} \text{ amps}/\sqrt{\text{Hz}}$$

$$e_n = (R_i) \cdot (i_n)$$

$$\text{Thus } e_n = (270) 1.266 \times 10^{-12}$$

$$e_n = 0.34 \times 10^{-9} \text{ V}/\sqrt{\text{Hz}}$$

The total transistor noise is then

$$e_T = [(0.34 \times 10^{-9})^2 + (.293 \times 10^{-9})^2]^{1/2}$$

$$e_T = .449 \times 10^{-9} \text{ V}/\sqrt{\text{Hz}}$$

Operating both halves of the transistor in parallel results in a noise reduction by the $\sqrt{2}$.

$$\text{Thus } e_{nt} = 0.317 \times 10^{-9} \text{ V}/\sqrt{\text{Hz}}$$

Summing the noise sources results in the following total noise.

For Channel 1

$$e_N = [(1.05 \times 10^{-9})^2 + (1.12 \times 10^{-9})^2 + (.317 \times 10^{-9})^2]^{1/2}$$

$$e_N = 1.57 \times 10^{-9} \text{ V}/\sqrt{\text{Hz}}$$

$$\text{or } e_N = 2.03 \times 10^{-9} \text{ V in a bandwidth of 1.67 Hz.}$$

For Channels 2 - 12,

$$e_n = [(0.52 \times 10^{-9})^2 + (1.12 \times 10^{-9})^2 + (.317 \times 10^{-9})^2]^{1/2}$$

$$e_n = 1.27 \times 10^{-9} \text{ V}/\sqrt{\text{Hz}}$$

$$\text{or } e_n = 1.65 \times 10^{-9} \text{ V in a bandwidth of 1.67 Hz.}$$

This calculated value compares favorably to the actual noise measured from a similar type of amplifier, the results of which are shown in Figure 3.4-3.

The gain of the input transistor is approximately

$$A = \frac{R_L}{r_e} \quad \text{where} \quad r_e = \frac{KT}{q I_E}$$

$$r_e = 10.4 \text{ ohms}$$

$$A = \frac{2000}{10.4} = 192 .$$

Thus the open loop gain of the first stage is $(192) \cdot (100) = 19,200$.

The closed loop gain of the first stage is $\frac{R_f}{R_{DET}}$

$$A = \frac{50000}{270} = 185 .$$

3.4.1.2 Indium Antimonide Channels

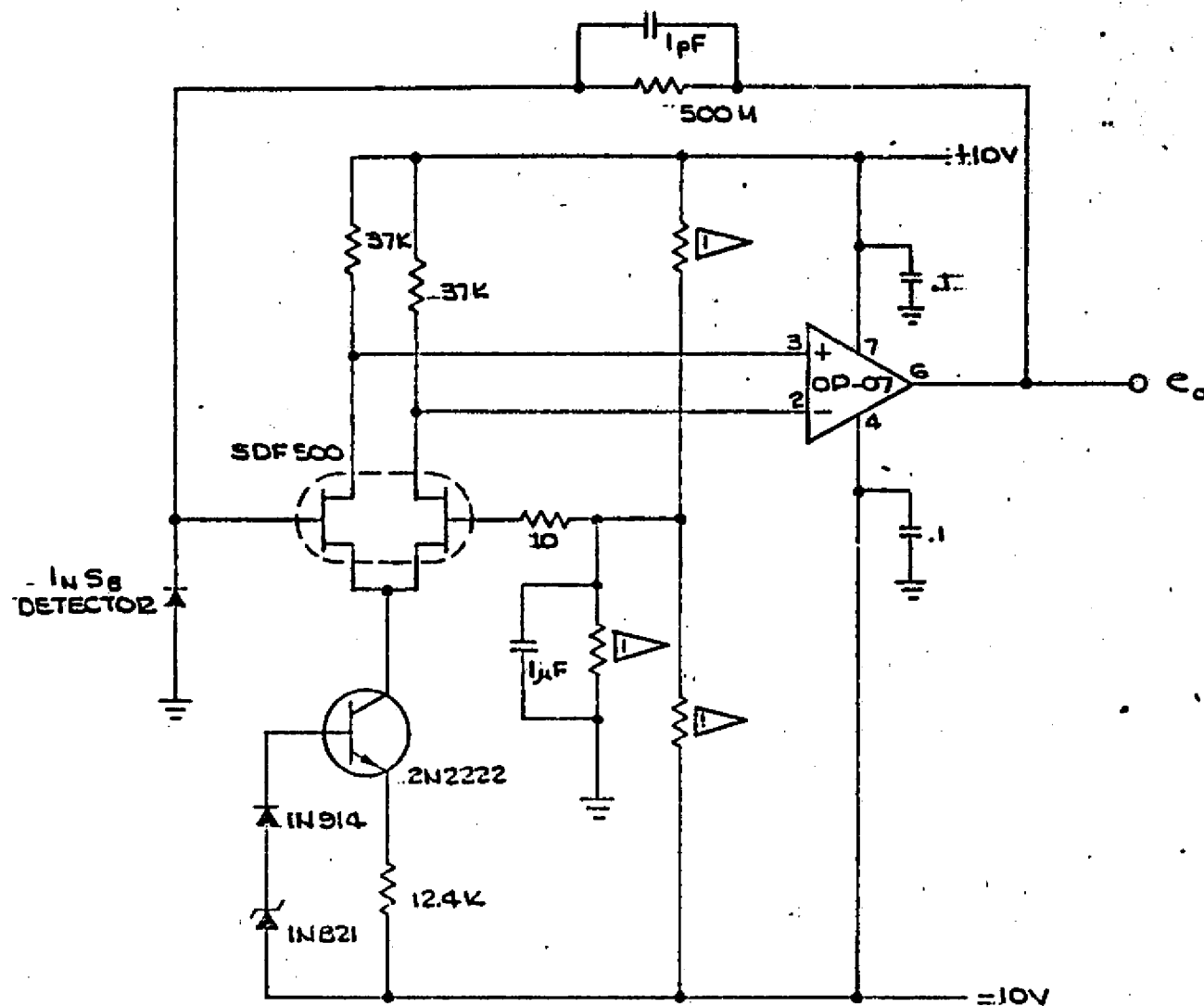
The preamplifier for the Indium Antimonide (InSb) Channels 13 through 28 will consist of a differential pair FET input followed by a low noise operational amplifier as shown in Figure 3.4-4.

The input FET as well as the feedback resistor, R_f , are cooled to a temperature of $\sim 150K$ by mounting them on the first stage of the radiant cooler in order to reduce the system noise. Mounting these components on the first stage also has the advantage of allowing shorter length connections to the high impedance components which reduces stray capacity and also reduces the susceptibility to noise pickup.

Individual preamplifiers will be used for each channel and a common ground will be used for all of the InSb detectors to minimize the number of leads required going to the second stage of the cooler.

A common source differential FET input is used because this configuration provides a very high input resistance and reduces the effect of the drift, offset and noise of the operational amplifier by the gain of the FET input stage.

The noise analysis of the preamplifier is based on the noise equivalent circuit shown in Figure 3.4-5; the gain bandwidth equivalent circuit is given in Figure 3.4-6.



▷ TAILOR FOR
DET BIAS

Fig. 3.4-4 InSb Preamplifier

ORIGINAL PAGE IS
OF POOR QUALITY

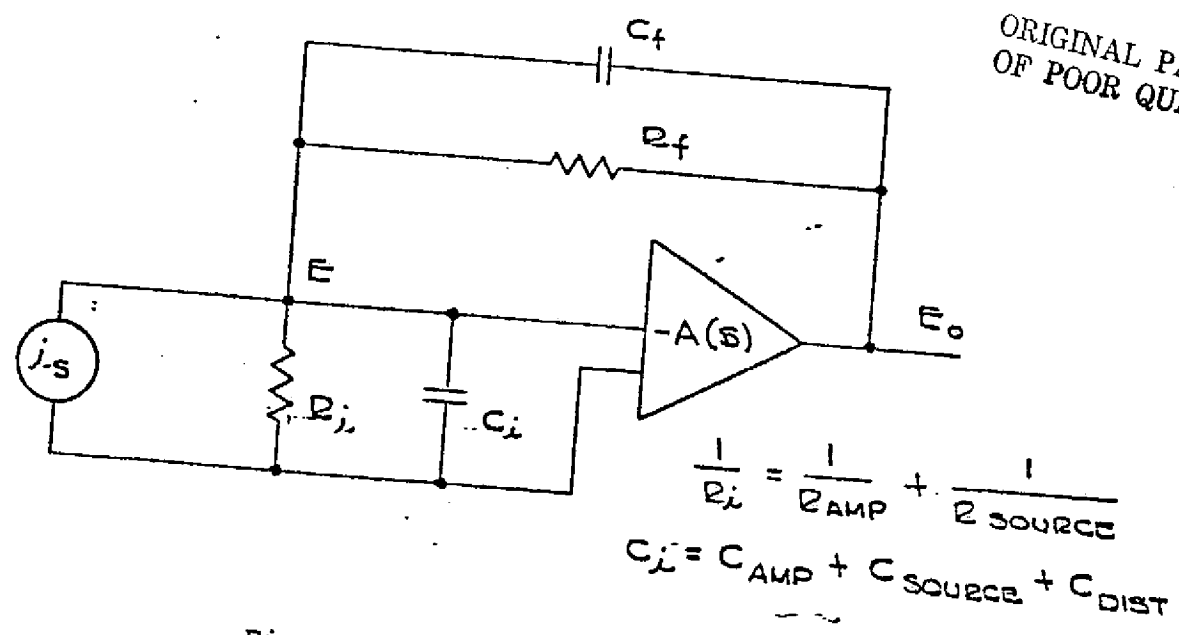


Fig. 3.4-6 Gainbandwidth Equivalent Circuit

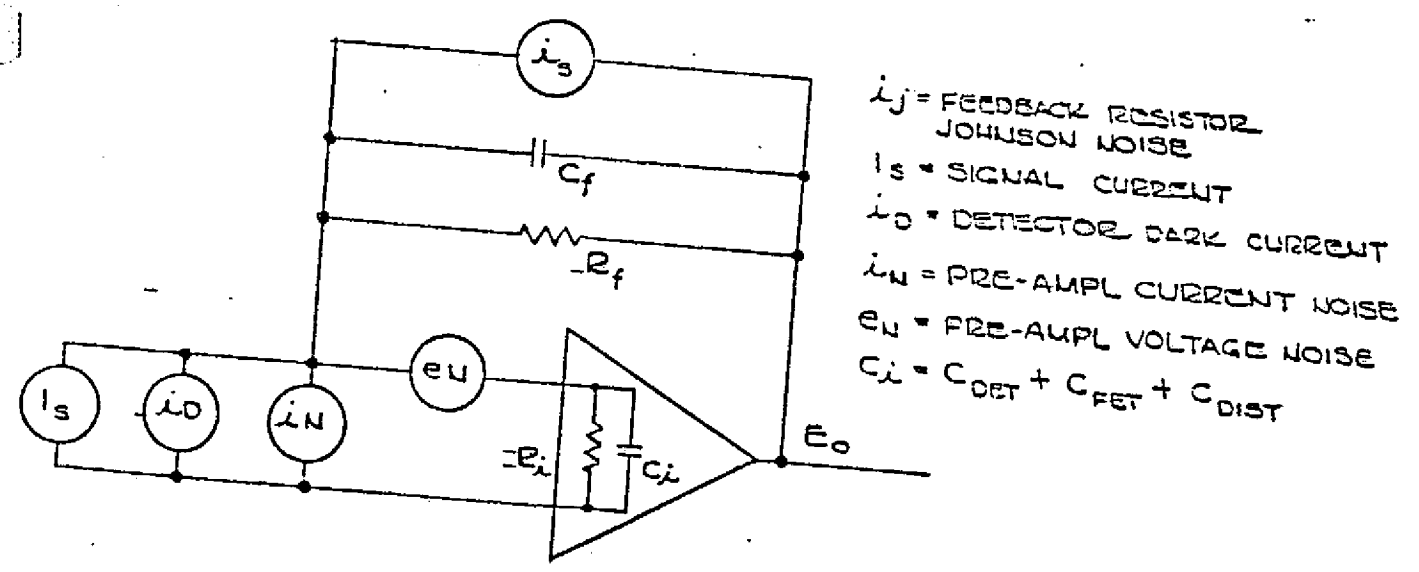


Fig. 3.4-5 Noise Equivalent Circuit

The Johnson noise of the feedback resistor is calculated at a temperature of 150°K since the resistor will be mounted on the 1st stage of the radiant cooler.

$$i_R = \left[\frac{4KTB}{R_F} \right]^{1/2}$$

$$K = 1.38 \times 10^{-23}$$

$$B = 1 \text{ Hz}$$

The following table summarizes the noise currents for various values of feedback resistors.

R_F	$i_n \text{ Amps}/\sqrt{\text{Hz}}$	
	@ 150°K	@ 300K
100 Meg	9.10×10^{-15}	1.29×10^{-14}
200 Meg	6.43×10^{-15}	9.10×10^{-15}
400 Meg	4.55×10^{-15}	6.43×10^{-15}
500 Meg	4.07×10^{-15}	5.75×15^{-15}
600 Meg	3.71×10^{-15}	5.25×15^{-15}
800 Meg	3.22×10^{-15}	4.55×10^{-15}
1000 Meg	2.88×10^{-15}	4.07×15^{-15}
2000 Meg	2.03×10^{-15}	2.88×10^{-15}
3000 Meg	1.66×10^{-15}	2.35×10^{-15}

3.4.1.2.1 Reduction of FET Noise by Reduced Temperature

The basic noise voltage of a FET caused by the channel resistance can be represented by the following equation:

$$e_n = \left[4KTR_N B \left(1 + \frac{f_1}{f^n} \right) \right]^{1/2}$$

$$K = 1.38 \times 10^{-23}$$

$$R_N \approx \frac{0.67}{g_{fs}}$$

but g_{fs} increased by $\approx .5$ percent/°C as the temperature is reduced.

For an SDF 500 FET with $V_{DS} = 20$ V and $I_D = 200$ μ A, $g_{fs} = 500$ μ mho
min at 300K

Therefore at 150K

$$g_{fs} = (500) [1 + (.005) \cdot (150)]$$

$$g_{fs} = 875 \times 10^{-6}$$

@ 300K

$$e_n = \sqrt{4K (300) \frac{.67}{500 \times 10^{-6}}} = 4.71 \times 10^{-9} \text{ V}/\sqrt{\text{Hz}}$$

@ 150K

$$e_n = \sqrt{4K (150) \frac{.67}{875 \times 10^{-6}}} = 2.52 \times 10^{-9} \text{ V}/\sqrt{\text{Hz}}$$

$$\frac{2.52}{4.71} = .535$$

The portion of e_n due to the channel resistance is reduced to 0.535 of original by going to 150K.

Since the preamp input is a differential FET pair the noise is $\sqrt{2}$ times the single FET noise.

@ 300K

$$e_n = \sqrt{2} (4.71 \times 10^{-9}) = 6.66 \times 10^{-9} \text{ V}/\sqrt{\text{Hz}}.$$

This corresponds reasonably well to the measured preamp noise of an actual amplifier beyond the 1/f region, therefore it is reasonable to assume that the temperature reduction factor is valid.

The actual measured noise on a previously constructed preamp is 15 $\text{nv}/\sqrt{\text{Hz}}$ at 300K. Cooling to 150K will result in an $e_n = 8.0 \times 10^{-9} \text{ V}/\sqrt{\text{Hz}}$.

3.4.1.2.2 FET Gate Leakage Current

An SDF500 Solitron FET operating at $V_{DS} = 20V$ and $I_D = 200\mu a$ has an $I_g = 50 \text{ pa}$ at $25^\circ C$.

The current noise is given by

$$i_n = \sqrt{2 q I_G B}$$

$$q = 1.602 \times 10^{-19}$$

Thus $i_n = 4.00 \times 10^{-15} \text{ amps}/\sqrt{\text{Hz}}$ at 300K.

Lowering the temperature reduces I_g by a factor of 2 for each $10^\circ C$.

Therefore @ $150^\circ K$, $I_G = \frac{50 \times 10^{-12}}{2^{15}} = 1.53 \times 10^{-15}$

and $i_n = 2.21 \times 10^{-17} \text{ amps}/\sqrt{\text{Hz}}$ at 150K.

Each InSb is 0.84 mm square giving an active area of

$$.034 \text{ in.} \times .034 \text{ in.} = 1156 \text{ mil}^2$$

Added to this is a 5 x 5 mil contact area.

Since the detector has a capacity of approximately 0.2 pf/mil², this results in a total calculated capacity of

$$1181 \times 0.2 = 236 \text{ pf.}$$

For noise calculation purposes, an additional 75 pf will be added to this value for stray and undefined capacitances.

If the system chopper operates at 250 Hz, the noise due to the input capacity is as follows:

$$i_n = \frac{e_n}{z_i} = \frac{e_n}{\frac{R_i}{1 + j\omega R_i C_i}}$$

$$i_n = \frac{e_n (1 + j \omega R_i C_i)}{R_i}$$

$$i_n = \frac{8.0 \times 10^{-9} [(1)^2 + (2\pi \times 250 \times 5 \times 10^8 \times 312 \times 10^{-12})^2]^{\frac{1}{2}}}{5 \times 10^8}$$

$$i_n = 3.92 \times 10^{-15} \text{ amps}/\sqrt{\text{Hz}}.$$

3.4.1.2.2 Amplifier Stability

The feedback capacitor required for amplifier stability determines the closed loop breakpoint frequency and also the amount of noise current from the feedback resistor at frequencies above the breakpoint.

The size of the feedback capacitor can be determined as follows:

$$C_f = \frac{2d^2 + 2d \sqrt{(d^2 + R_f C_i \omega_H)}}{R_f \omega_H}$$

Where C_f = feedback capacitor

d = damping ratio

R_f = feedback resistor

ω_H = GBW of amplifier

C_i = input capacity.

For this case, assume $d = 1$

$R_f = 500 \text{ Meg}$

GBW = 500 KHz

$C_i = 312 \text{ pf.}$

$$C_f = \frac{2 (1)^2 + 2 (1) \sqrt{1^2 + 5 \times 10^8 \times 3.12 \times 10^{-10} \times 3.14 \times 10^6}}{5 \times 10^8 \times 3.14 \times 10^6}$$

$$C_f = .89 \times 10^{-12}$$

$$C_f \approx 1.0 \text{ pf.}$$

The breakpoint of the amplifier frequency response is given by:

$$\omega_{3db} = \frac{1}{R_f C_f}$$

$$\omega_{3db} = \frac{1}{5 \times 10^8 \times 1 \times 10^{-12}}$$

$$\omega_{3db} = 2000 \text{ rad/sec}$$

$$\text{or } f_{3db} = 318 \text{ Hz.}$$

Thus the amplifier will still have a flat response at the chosen chopping frequency of 250 Hz.

The InSb detectors will be operated at 84 kelvins and because of the narrow spectral bands that they see, will have a dynamic resistance of 500 meg or greater. This will result in a Johnson noise of

$$i_{nd} = \sqrt{\frac{4KTB}{R_d}}$$

$$i_{nd} = \sqrt{\frac{4 \times 1.38 \times 10^{-23} \times 84}{5 \times 10^8}}$$

$$i_{nd} = 3.05 \times 10^{-15} \text{ amps}/\sqrt{\text{Hz}}.$$

3.4.1.2.3 Noise Summary

The individual contributions of each noise source for the indium antimonide channel preamplifiers is listed below:

Feedback Johnson	$i_n = 4.07 \times 10^{-15} \text{ amp}/\sqrt{\text{Hz}}$
Detector Johnson	$i_n = 3.05 \times 10^{-15} \text{ amp}/\sqrt{\text{Hz}}$
$e_n/\text{Input Z}$	$i_n = 3.92 \times 10^{-15} \text{ amp}/\sqrt{\text{Hz}}$
FET Leakage	$i_n = 2.21 \times 10^{-17} \text{ amp}/\sqrt{\text{Hz}}$

The total noise will be:

$$i_n = \left[(4.07 \times 10^{-15})^2 + (3.05 \times 10^{-15})^2 + (3.92 \times 10^{-15})^2 + (2.21 \times 10^{-17})^2 \right]^{1/2}$$

$$i_n = 6.42 \times 10^{-15} \text{ amp}/\sqrt{\text{Hz}}.$$

Since the system bandwidth is 1.67 Hz, the total noise is equal to

$$\sqrt{1.67} \cdot (6.42 \times 10^{-15}).$$

$$i_n \text{ Total} = 0.83 \times 10^{-14} \text{ amps.}$$

Other chopping frequencies result in the following noise currents.

Freq.	$e_n/\text{Input Z}$	$i_n \text{ (amps}/\sqrt{\text{Hz}})$	$i_n \text{ (1.67 Hz BW)}$
500	$7.84 \times 10^{-15} \text{ amp}/\sqrt{\text{Hz}}$	9.35×10^{-15}	$1.21 \times 10^{-14} \text{ amp}$
750	$11.76 \times 10^{-15} \text{ amp}/\sqrt{\text{Hz}}$	12.81×10^{-15}	$1.66 \times 10^{-14} \text{ amp}$
1000	$15.57 \times 10^{-15} \text{ amp}/\sqrt{\text{Hz}}$	16.38×10^{-15}	$2.12 \times 10^{-14} \text{ amp}$

3.5 Instrument Cooling

Both the radiant cooler design (Sec. 3.2) and the short-wave channel sensitivity (Sec. 3.3.2.1) depend on cooling the spectrometer to a nominal -25°C (248K). We will now outline how this cooling can be accomplished. The spectrometer is contained within a volume approximately as shown in Figure 3.5-1. The horizontal surface that faces the earth is a silver teflon radiator. In an isolated condition, i.e., when perfectly isolated from the rest of the instrument, this radiator has a temperature of 238.6K in the nominal Tiros-N orbit (Ref. 1)*. That is, it would reach an equilibrium temperature of 238.6K when exposed to the sun and earth. If the spectrometer actually runs at 248K, the radiator will emit a net power given by

$$\epsilon_h \sigma A_h \left[(248)^4 - (238.6)^4 \right] = 6.94\text{W},$$

where A_h is the silver teflon area of $14.75 \times 33 \text{ in}^2$ and ϵ_h is its emissivity of 0.72. This power is then equal to the sum of radiative and conductive inputs to the other surfaces of the spectrometer.

For the configuration shown in Figure 3.5-1, both these inputs come from surfaces at the temperature of the electronics and telescope/scanner assemblies, assumed to be 20°C . For facing surfaces that are gold plated, the radiative input is given by

$$\frac{\sigma A_i}{\left(\frac{2}{\epsilon_i} - 1 \right)} \left[(293)^4 - (248)^4 \right] = 3.74\text{W},$$

where A_i = total spectrometer outer area that is gold plated
 $= 1237 \text{ in}^2$

ϵ_i = emissivity of gold plating = 0.045

This leaves us with an allowable conductive input of

$$K_h (293-248) = 6.94 - 3.74 = 3.20\text{W}$$

or $K_h = 0.071 \text{ WK}^{-1}$

where K_h is the thermal conductance between the spectrometer and the rest of the instrument.

* reference on next page.

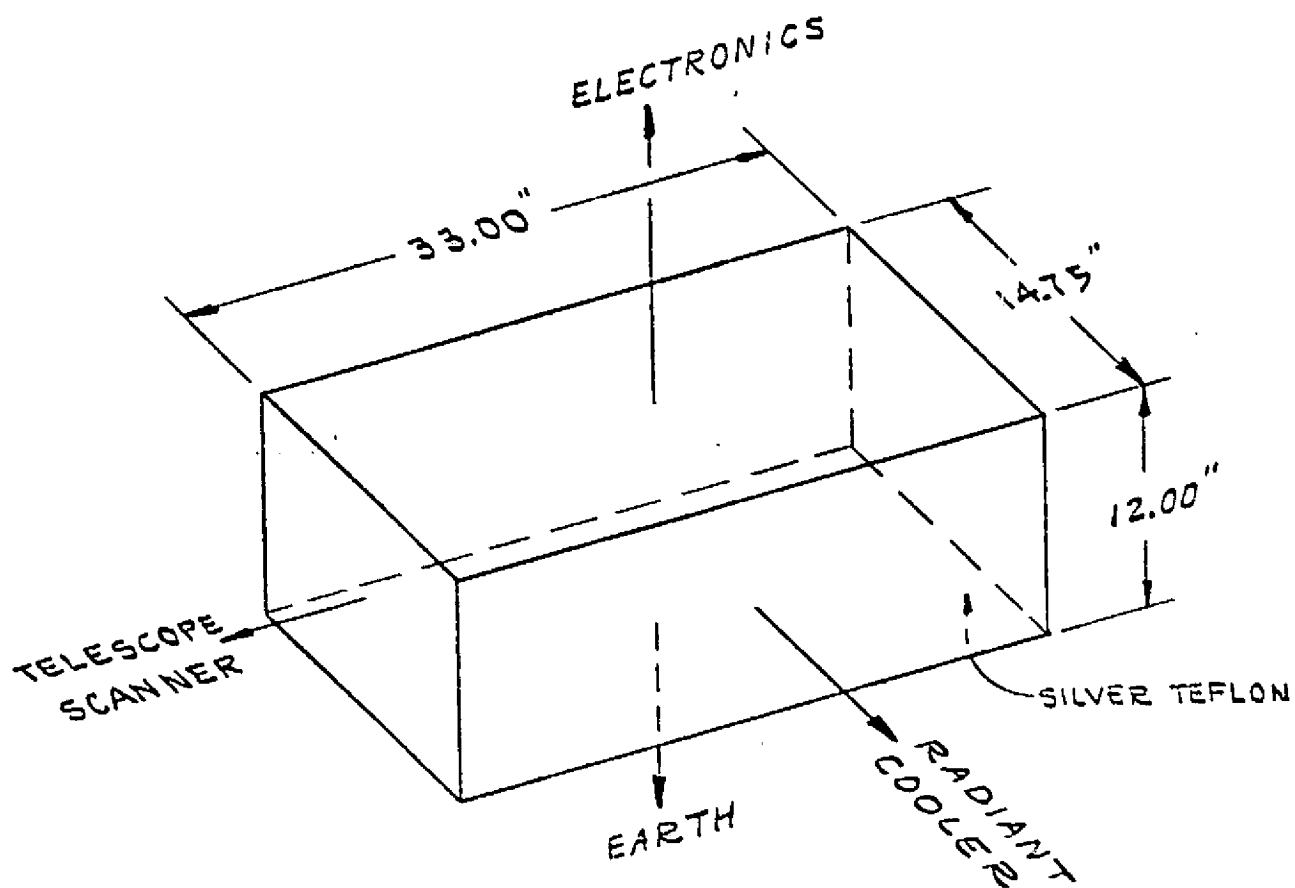


FIG. 3.5-1
AMTS SPECTROMETER PACKAGE (SIMPLIFIED)

If we reserve 10% of the conductance for electrical connections, there is 0.064 WK^{-1} left for mechanical supports and standoffs. The spectrometer will probably have supports connected to both the electronics and telescope/scanner assemblies (See Figure 3.5-1). The other two insulated surfaces will face plates tied to these two assemblies. These surfaces will require only standoffs. Assuming that there are 10 synthane G-10 standoffs of 1/4-inch od, 1/8-inch id, and 1/4-inch free length (surface separation), they will have a thermal conductance given by

$$K_s = 10 \frac{\pi[(1/4)^2 - (1/8)^2] \times 2.54 \times 4.4 \times 10^{-3}}{4 \times 0.25} = 0.016 \text{ WK}^{-1},$$

where $4.4 \times 10^{-3} \text{ (W cm}^{-1} \text{ K}^{-1})$ is the thermal conductance of synthane G-10 in temperature range of interest (Ref. 2). This leaves us 0.048 WK^{-1} for the supports. If there are 10 of these, again of synthane G-10, they can have an od of 0.50 inch, an id of 0.34 inch, and a free length of 0.25 inch.

References (for Section 3.5)

1. Advanced Very High Resolution Radiometer, Mod. 2, Technical Description, Contract NAS5-2340, ITT-A/OD for NASA/GSFC, July 14, 1977, Section 5.1.
2. Results of Experiment to Determine the Thermal Conductivity of Synthane G-10 and Polyimide Composite, memo of Dec. 23, 1974, R. V. Annable, ITT-A/OD.

4.0 New Technology

No new technology was generated during this design definition study for the AMTS instrument.

5.0 Conclusions and Recommendations

The results of this study show that an AMTS instrument can be designed and built which will achieve the 0.5 cm^{-1} resolution in the 607 to 669 cm^{-1} wavenumber bands and 2.0 cm^{-1} resolution in the 2380 to 2395 cm^{-1} wavenumber bands. Contacts with two different optical suppliers indicate that the thin field lenses required by the narrow spectral bands and close spacing between some of the channels can be fabricated. The optical resolution of the f/5, 762 m.m. focal length spectrometer is adequate to provide good spectral resolution as shown by the Optical Research Associates analyses. A radiant cooler was designed to cool the 28 infrared detectors to 84 Kelvin in order to provide signal-to-noise ratios of $> 100:1$ for a 220 Kelvin scene for all channels except two (27 and 28) where lower S/N ratios are acceptable.

Recommendations include additional optical, thermal and structural analyses as well as fabrication and test of critical system components. In particular, fabrication of HgCdTe detectors for the longer wavelength channels (16 and $16.5 \mu\text{m}$) is recommended since detector manufacturers have very limited experience in making detectors which operate at these wavelengths and at the proposed operating temperature of 84 Kelvin.